The Effect of Hole Geometry on the Near Field Character of Crossflow Jets

by

Brenda A. Haven

A dissertation submitted in partial fulfillment
of the requirements for the degree of

Doctor of Philosophy

University of Washington

1996

Approved by _____
(Chairman of Supervisory Committee)

Program Authorized
to Offer Degree _____

Date _____

REPORT DOCUMENTATION PAGE

Public reporting burden for this collection of information is estimated to average 1 hour per response, including the time for reviewing instructions, searching existing data sources, gathering and maintaining the data needed, and completing and reviewing the collection of information. Send comments regarding this burden estimate or any other aspect of this collection of information, including suggestions for reducing this burden, to Washington Headquarters Services, Directorate for Information Operations and Reports, 1215 Jefferson Davis Highway, Suite 1204, Arlington, VA 22202-4302, and to the Office of Management and Budget, Paperwork Reduction Project (0704-0188), Washington, DC 20503.

1. AGENCY USE ONLY (Leave blank)	2. REPORT DATE 1996	3. REPORT TYPE AND DATES COVERED

4. TITLE AND SUBTITLE
The Effect of Hole Geometry on the Near Field Character of Crossflow Jets

5. FUNDING NUMBERS

6. AUTHOR(S)

Brenda A. Haven

7. PERFORMING ORGANIZATION NAME(S) AND ADDRESS(ES)

AFIT Student Attending:

University of Washington

8. PERFORMING ORGANIZATION REPORT NUMBER

96-017D

9. SPONSORING/MONITORING AGENCY NAME(S) AND ADDRESS(ES)
DEPARTMENT OF THE AIR FORCE
AFIT/CI
2950 P STEET, BLDG 125
WRIGHT-PATTERSON AFB OH 45433-7765

10. SPONSORING/MONITORING AGENCY REPORT NUMBER

11. SUPPLEMENTARY NOTES

12a. DISTRIBUTION/AVAILABILITY STATEMENT
Approved for Public Release IAW 190-1
Distribution Unlimited
BRIAN D. GAUTHIER, MSgt, USAF
Chief Administration

12b. DISTRIBUTION CODE

13. ABSTRACT (Maximum 200 words)

19960809 061

14. SUBJECT TERMS

15. NUMBER OF PAGES
126

16. PRICE CODE

17. SECURITY CLASSIFICATION OF REPORT	18. SECURITY CLASSIFICATION OF THIS PAGE	19. SECURITY CLASSIFICATION OF ABSTRACT	20. LIMITATION OF ABSTRACT

NSN 7540-01-280-5500

DTIC QUALITY INSPECTED 1

Standard Form 298 (Rev. 2-89)
Prescribed by ANSI Std. Z39-18
298-102

GENERAL INSTRUCTIONS FOR COMPLETING SF 298

The Report Documentation Page (RDP) is used in announcing and cataloging reports. It is important that this information be consistent with the rest of the report, particularly the cover and title page. Instructions for filling in each block of the form follow. It is important to *stay within the lines* to meet *optical scanning requirements*.

Block 1. Agency Use Only *(Leave blank)*.

Block 2. Report Date. Full publication date including day, month, and year, if available (e.g. 1 Jan 88). Must cite at least the year.

Block 3. Type of Report and Dates Covered. State whether report is interim, final, etc. If applicable, enter inclusive report dates (e.g. 10 Jun 87 - 30 Jun 88).

Block 4. Title and Subtitle. A title is taken from the part of the report that provides the most meaningful and complete information. When a report is prepared in more than one volume, repeat the primary title, add volume number, and include subtitle for the specific volume. On classified documents enter the title classification in parentheses.

Block 5. Funding Numbers. To include contract and grant numbers; may include program element number(s), project number(s), task number(s), and work unit number(s). Use the following labels:

C	-	Contract	PR	- Project
G	-	Grant	TA	- Task
PE	-	Program Element	WU	- Work Unit Accession No.

Block 6. Author(s). Name(s) of person(s) responsible for writing the report, performing the research, or credited with the content of the report. If editor or compiler, this should follow the name(s).

Block 7. Performing Organization Name(s) and Address(es). Self-explanatory.

Block 8. Performing Organization Report Number. Enter the unique alphanumeric report number(s) assigned by the organization performing the report.

Block 9. Sponsoring/Monitoring Agency Name(s) and Address(es). Self-explanatory.

Block 10. Sponsoring/Monitoring Agency Report Number. *(If known)*

Block 11. Supplementary Notes. Enter information not included elsewhere such as: Prepared in cooperation with...; Trans. of...; To be published in.... When a report is revised, include a statement whether the new report supersedes or supplements the older report.

Block 12a. Distribution/Availability Statement. Denotes public availability or limitations. Cite any availability to the public. Enter additional limitations or special markings in all capitals (e.g. NOFORN, REL, ITAR).

DOD - See DoDD 5230.24, "Distribution Statements on Technical Documents."
DOE - See authorities.
NASA - See Handbook NHB 2200.2.
NTIS - Leave blank.

Block 12b. Distribution Code.

DOD - Leave blank.
DOE - Enter DOE distribution categories from the Standard Distribution for Unclassified Scientific and Technical Reports.
NASA - Leave blank.
NTIS - Leave blank.

Block 13. Abstract. Include a brief *(Maximum 200 words)* factual summary of the most significant information contained in the report.

Block 14. Subject Terms. Keywords or phrases identifying major subjects in the report.

Block 15. Number of Pages. Enter the total number of pages.

Block 16. Price Code. Enter appropriate price code *(NTIS only)*.

Blocks 17. - 19. Security Classifications. Self-explanatory. Enter U.S. Security Classification in accordance with U.S. Security Regulations (i.e., UNCLASSIFIED). If form contains classified information, stamp classification on the top and bottom of the page.

Block 20. Limitation of Abstract. This block must be completed to assign a limitation to the abstract. Enter either UL (unlimited) or SAR (same as report). An entry in this block is necessary if the abstract is to be limited. If blank, the abstract is assumed to be unlimited.

DISCLAIMER NOTICE
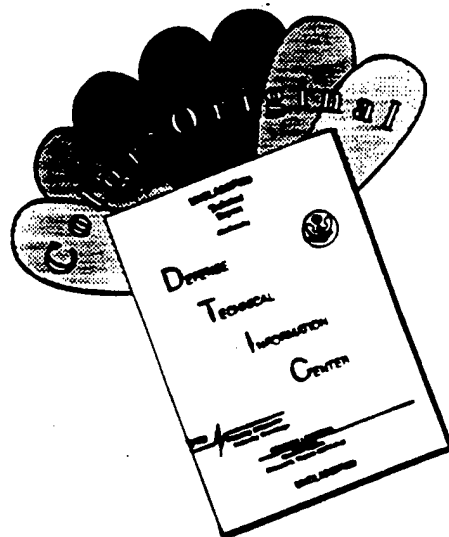
THIS DOCUMENT IS BEST QUALITY AVAILABLE. THE COPY FURNISHED TO DTIC CONTAINED A SIGNIFICANT NUMBER OF COLOR PAGES WHICH DO NOT REPRODUCE LEGIBLY ON BLACK AND WHITE MICROFICHE.

Doctoral Dissertation

University of Washington

Abstract

The Effect of Hole Geometry on the Near Field Character of Crossflow Jets

by Brenda A. Haven

Chairman of Supervisory Committee: Professor Mitsuru Kurosaka
                                            Dept. of Aeronautics and Astronautics

Water tunnel experiments were conducted to understand the effect of hole exit geometry on the lift-off characteristics of crossflow jets. Six basic hole shapes were investigated, all having the same cross-sectional area: round, elliptical, square, and rectangular. Laser Induced Fluorescence (LIF) and Particle Image Velocimetry (PIV) were used to visualize the jet structures near the hole, and acquire velocity and vorticity field information, respectively. The flow visualization pictures, and PIV data images, graphs, and vector plots complement each other to provide a deeper understanding of the basic make-up of the kidney-vortices that are present in a crossflow jet.

The vorticity around the circumference of the jet was tracked using LIF and PIV to understand the relative contributions to the kidney-vortices. The jet side-wall boundary layer is responsible for the primary kidney vortex structures. These vortices result from the roll-up of the side-wall boundary layer as the jet exits the hole. Here, hole geometry alone was found to have a distinct influence on the lift-off behavior by affecting the lateral separation of these side-wall vortices.

The leading edge boundary layer contributes to the side-wall vortices in a complex way. As the jet interacts with the crossflow, the crossflow momentum causes the jet leading edge boundary layer to turn. This turning induces streamwise vorticity that rides over the top of the side-wall vortices. Depending on the hole geometry, this turning can induce a streamwise vortex pair having a rotational sense opposite to the kidney-vortices. The hole trailing edge boundary layer can likewise be turned toward the streamwise direction. In this case, the turning is caused by the strong reverse flow just downstream of the jet.

The results of the LIF and PIV studies show that all hole boundary layer vorticity, regardless of its origin along the hole circumference, contributes to the kidney-vortices sufficiently downstream.

LIF and PIV data were also taken for three industrial cooling hole designs. Comparison of the data shows favorable agreement with the general trends for the six basic hole shapes.

Table of Contents

List of Figures

List of Tables

List of Symbols

AR	Hole Aspect Ratio, D/L
BR	Blowing Ratio, $\rho_j U_j / \rho_\infty U_\infty$
C_p	Pressure Coefficient
D	Hole Lateral Dimension
H	Hole Passage Length
L	Hole Streamwise Dimension
Re_L	Reynolds Number based on Hole Streamwise Dimension and Jet Velocity
s	LaPlace Transform Variable
t	Time
U	Velocity
u	Streamwise Velocity
u'	Non-Dimensional Streamwise Velocity, u/U_∞
v	Lateral Velocity
v'	Non-Dimensional Lateral Velocity, v/U_∞
w	Vertical Velocity
w'	Non-Dimensional Vertical Velocity, w/U_j
x	Streamwise Direction
x'	Non-Dimensional Streamwise Direction, x/L
y	Lateral Direction
y'	Non-Dimensional Lateral Direction, y/D
z	Vertical Direction
z'	Non-Dimensional Vertical Direction, z/D_{hole3}
η	Vortex Strength in y-Direction
ν	Kinematic Viscosity
ρ	Density
ω	Vorticity
ω'	Non-Dimensional Vorticity, $\omega D_{hole3}/U_j$

$\tilde{\omega}$ LaPlace Transform of Vorticity, $\omega(t)$

ξ Vortex Strength in x-Direction

Subscripts

∞ Crossflow Properties

j   Jet Properties

n   Normal Component

0   Initial Condition

x   Property in Streamwise Direction

y   Property in Lateral Direction

z   Property in Vertical Direction

Acknowledgments

I would like to thank especially my advisor, Professor Mitsuru Kurosaka, whose enthusiasm and optimism provided constant motivation over the past three years. Without his encouragement and support, this work would not have been possible.

In addition, I would like to thank the people who supported me in the many aspects of my research. Bob Blair, whose friendship and outstanding technical support were always there when I needed it. Bob Lowe, who always took time to help me in the machine shop and give me direction when I didn't know where to begin. Brian Leverson, for coming to the rescue on numerous occasions when computer problems jeopardized the completion of my research.

I would also like to thank the office staff (Jane Lybecker, Marlo Anderson, Diane Collum, Lillian Lee, and Wanda Frederick) for their support, along with my friends and lab mates (Mike Fox, Phil Poutissou, Tony Simpson, Aline Cotel, and Ben Sayler) who were always available to lend a hand and who made this an enjoyable experience. Special thanks goes to Denise Yamagata, who provided the particle image velocimetry data presented in chapter 7 of this report.

Finally, I wish to thank my husband Mark for his constant encouragement and support.

Chapter 1: Introduction

1.1 Motivation

The requirement to cool the hottest components of the gas turbine engine has been around since the 1960's when the desire for increased specific thrust (power density) resulted in turbine inlet temperatures exceeding turbine blade material limits. Since this time, the temperature in the turbine area as been continually increasing. Material properties have been improved through alloying and innovative manufacturing processes, however, the gap continues to widen between material capability and desired operating temperature. At the present time the only option for operating at the desired turbine inlet temperatures is to cool the components, primarily those in the turbine area where the high temperatures and high stresses due to rotation represent the most hostile environment.

To cool a turbine blade or vane that is directly in the path of the hot, high-pressure gas stream leaving the combustor, high pressure air must be taken from the latter stages of the compressor. There are two serious consequences to extracting cooling air from this location. First, as the compressor pressure ratio increases to improve specific fuel consumption, the temperature of the cooling air also increases, reducing its cooling potential. In modern high performance engines having pressure ratios above 30, the cooling air itself can be as high as 950°K. Second, the air taken off at the compressor exit can be as much as 20% of the compressor discharge. As entropy increases due to heat transfer, and as losses in pressure are suffered in the blade passages, this air cannot be fully recovered for turbine output, which lowers the cycle efficiency. One approach to minimizing the effects of these consequences is to look at ways of increasing the effectiveness of the cooling system. A

turbine system typically employs several cooling methods to efficiently and effectively cool the entire blade/vane surface (see figure 1-1). The majority of modern turbine blade

gas stream

cooing air (a)

gas stream

cooing air (b)

gas stream

cooing air (c)

(a) Convective cooling
(a) Impingement cooling
(a) Film cooling
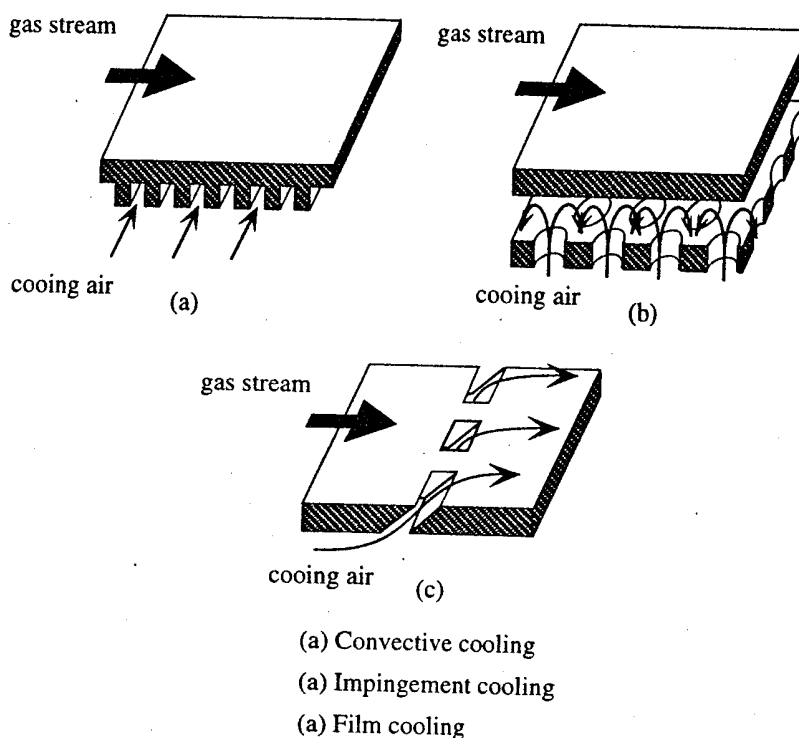
Figure 1-1: Turbine Blade/Vane Cooling Schemes

and vane designs rely on the combined effect of three cooling methods: convective, impingement, and film cooling techniques. Convective cooling of the blade's interior is accomplished by passing the cooling air through a series of serpentine passages inside the blade cavity. At the leading edge of the blades and vanes, where the stagnation of the hot turbine gas results in very high heat loads, impingement cooling is used to increase the heat transfer rate from the blade metal to the cooling air inside the blade. Both convective and impingement cooling techniques are interior to the blade or vane. As the temperature of the cooling air inside the blade rises, its usefulness in cooling the blade/vane decreases. Eventually the cooling air is discharged through the trailing edge or through small holes on the blade surface. By discharging the air through small holes on the blade surface, the

cooling air forms a protective layer providing a buffer between the hot gases and the metal surface. This technique, referred to as film cooling, is the subject of this work.

The effectiveness of film cooling for controlling the external blade temperature is higher than the use of internal schemes such as convective and impingement cooling. In other words, the coolant mass flow required for film cooling is less than that needed internally to produce the same benefit. The use of film cooling however has its disadvantages in the increased aerodynamic loss due to the disruption of the flow over the blade or vane surface. Also, the cooling effectiveness is dependent on the ability of the film layer to cover the surface. If the cooling layer leaves the blade surface, which all but eliminates the buffer between the hot gases and blade surface, local metal temperatures will increase reducing the life of the blade or vane. The lift-off behavior of the coolant depends strongly on the mass flux ratio, or blowing ratio between coolant jet and gas stream, or crossflow ($BR \equiv \rho_j U_j / \rho_\infty U_\infty$, where ρ_j and U_j are the jet density and velocity, respectively, and ρ_∞ and U_∞ are the crossflow density and velocity): the higher the ratio, the more prone the jet is to be blown off the surface. Although the mass flux ratio at which the film effectiveness begins to decline is around 0.5, in actual turbines the ratio often exceeds this critical value due to local variations in gas stream velocity and blade/vane interaction.

Since these shortcomings of film cooling are outweighed by its benefit in cycle efficiency, film cooling is now widely used in practice but its drawbacks warrant further research to improve performance.

1.2 Issues Related to Film Cooling

In as much as the crux of film cooling is for the jet to remain attached to the protected surface even at the high blowing ratios, the problem is fundamentally of the fluid dynamic nature; heat transfer plays only a dependent role.

In film cooling, as with any jet in a crossflow stream, a pair of counter-rotating vortices are formed as the coolant jet interacts with the on-coming hot gas stream. As shown in figure 1-2, these vortices, often referred to as "kidney-shaped" vortices, or kidney-vortices, have a sense of rotation that acts to lift the coolant from the surface. As the coolant

lift-off by mutual
induction

kidney-vortices
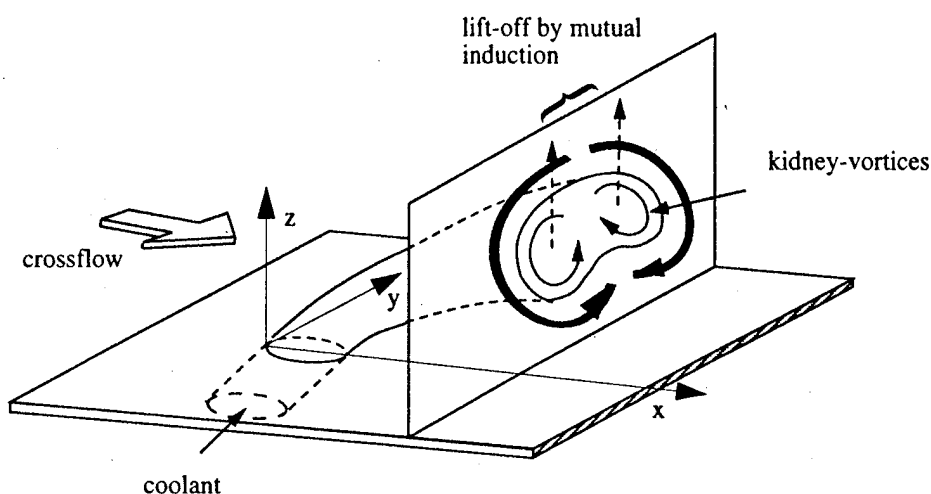
crossflow

coolant

Figure 1-2: Kidney-Vortices formed by a Jet in a Crossflow

leaves the surface, the rotation of the vortices also promotes entrainment of the hot gases down toward the surface. The combination of coolant lift-off and hot gas entrainment can seriously degrade the effectiveness of the film cooling layer to protect the metal surface.

The need for improved cooling performance, coupled with advancement in manufacturing techniques, has lead to the advent of "shaped" holes. These cooling hole designs are characterized by an increase in cross-sectional area toward the exit (e.g. Norton, *et al.*, 1990). Although these new designs have demonstrated superior cooling performance relative to conventional round holes, there are two major drawbacks to their use. First, they are expensive to manufacture for production, and second, at lower blowing ratios, their cooling effectiveness is lower than that for round and straight holes.

Efforts to overcome these drawbacks are thwarted by the countless parameters needed to define the shaped geometry, and by the basic lack of fluid dynamical understanding of why shaped holes work. To make the problem more tractable, this research, therefore, focuses on establishing the link between the kidney-vortex structures and simpler hole geometries. Once a basic fluid dynamical understanding of the kidney-vortices is reached, it then becomes the foundation for more complex hole designs. Before going into further detail, a review of the past research is in order.

1.3 Review of Past Research

In addition to film cooling for turbines, crossflow jets have been used in many diverse technical applications: cooling for combustors, fuel injection for burners, vectored thrust and thrust reversers for propulsive systems, pollutants emitted from chimneys, and effluent discharged from a pipe into rivers. Thus the literature on the subject is scattered among disciplines such as aeronautics, heat transfer, and environmental engineering. Depending on the specific applications, the objectives are naturally different. For film cooling, the attachment of the jet to the wall with minimum entrainment is crucial; however, for an application such as smokestack discharge, the vertical rise of the plume and diffusion into atmosphere are of main concern. Other important differences lie in the presence or absence of the wall as a constraining influence on the jet. In film cooling, the wall causes the formation of an upstream horseshoe vortex system; for the smoke plume, wall effects have little or no bearing on the flow structures.

Historically, Scorer (1958) appears to be among the first who called attention to the presence of counter-rotating vortices in a crosswind. From a simple argument for upward momentum, he deduced that in the absence of buoyancy the jet rises as $z \propto x^{1/3}$. He also proposed that the counter-rotating vortices were formed only from the roll-up of the vorticity at the sides of the orifice; the vortices at leading and trailing edges of the orifice are considered to annul each other.

Turner (1960) appears to be credited with taking the first photograph of a laboratory demonstration of the kidney-pair in water. The photograph does not show the kidney-shaped vortices *per se*; instead, it shows a bent-over buoyant jet, which is split sideways into two streamwise vortices.

In the specific area of turbine engine film cooling, Kadotani and Goldstein (1979) seem to have presented the first definitive data showing a striking similarity between the constant velocity and constant temperature contours within the jet cross-sections. The experiments were conducted in air at a blowing ratio of 0.35, with jets inclined at 35° relative to the crossflow.

Earlier measurements of crossflow jets, such as those by Keffer and Baines (1963), Kamotani and Greber (1972), and Fearn and Weston (1974), were concerned either with the far-field velocity and vorticity distributions or the trajectory of jets. An unexpected and noteworthy result of Fearn and Weston was that the initial strength of the vortex pair is directly proportional to the speed of the jet at the orifice and to the diameter of the jet; and found to be *independent* of the *crossflow speed*.

Near-field velocity and pressure measurements for a round jet were obtained in varying degrees of detail by Bergeles, Gossman, and Launder (1976), Moussa, Trischka and Eskinazi (1977), Sugiyama and Usami (1979), Crabb, Durao, and Whitelaw (1981), Andreopoulos (1982), Andreopoulos and Rodi (1984), Andreopoulos (1985), Sugiyama and Kawase (1985), and Sugiyama (1992). Notable among them are the time-averaged hot-wire data taken by Moussa, Trischka and Eskinazi for a round pipe protruding into a crossflow, which shows the presence of what is called here a 'negative' vortex pair amongst the kidney-vortices. They attribute this 'negative' vortex pair to the generation of negative vorticity by the crossflow in reaction to the 'positive' kidney vortex pair. The negative pair, according to them, originates *within* the crossflow. This view, however, appears to contradict the premise that the vorticity can be generated only from solid boundaries. With the sole exception of Moussa, Trischka and Eskinazi, no reference to this 'negative' pair appears to have been made by other investigators. Andreopoulos (1982) studied how the crossflow affects the *pipe* flow before it reaches the exit plane. He found that the influence of the crossflow is felt up to three pipe-diameters inside the pipe, and that the skewness of the jet velocity profile becomes well established at one and one-half diameters prior to the exit. He also cites the results of flow visualization studies where the pipe flow is observed to separate inside the pipe at the leading edge.

The pressure distribution on the wall around a circular hole was obtained by Vogler (1963), Fearn and Weston (1975), Bergeles, Gossman, and Launder (1976), and Sugiyama (1995). In contrast to the pressure coefficient, C_p, distributions around a solid cylinder, the data common to all crossflow jets show the following features: (1) at the leading edge, C_p is less than 0.7, (*i.e.* the leading edge is not a stagnation point), (2) near $\theta = 90°$, C_p

becomes as low as -4 (compared to $C_p = -3$ for 2-D potential flow around a cylinder), and (3) at $\theta = 180°$, C_p is typically lower than that for the case of a solid cylinder.

. Wake vortex structures resembling a Kármán-vortex street have long been observed downstream of crossflow jets from round holes. These wake vortices were the subject of a detailed study by Fric (1990), and Fric and Roshko (1994). Based on their clear position that the only source of new vorticity within the jet must be from a solid boundary, they conducted smoke flow visualization studies and traced the origin of wake vortices to the separation of the crossflow boundary layer at the downstream side of the hole.

Next we turn attention to crossflow jets from non-circular holes. Goldstein, Eckert, and Burgraff (1974) investigated the film cooling effectiveness of the so-called diffusion, or shaped, hole used in the industry. The cross section of the holes on the plenum side is circular, with the sides of the coolant passage laterally widening at an angle of 10° near the exit to an area ratio of three. The jet is angled 35° relative to the crossflow. Their flow visualization and heat transfer results shows that, compared with circular holes of the same plenum side diameter, the shaped holes have better attachment and a higher film effectiveness. As a proposed explanation, they state, *"One explanation of the increased effectiveness with shaped holes is that the mean velocity of the secondary flow is decreased with the larger exit area. This lower effective blowing rate causes the jet to stay closer to the wall rather than penetrating into the mainstream and accounts for the higher film cooling effectiveness, particularly at high blowing rates."* More recently, Norton *et al.* (1990) conducted extensive investigations of different shaped holes for other industrial uses.

With regard to simpler hole geometries, square holes were investigated by Ajersch *et al.* (1995), and rectangular holes by Brown and Minty (1975), Kikkawa and Nakanishi (1987), and Krothapalli, Lourenco, and Buchlin (1990). For rectangular holes of varying aspect ratios, both Brown and Minty, and Kikkawa and Nakanishi observed that the use of higher aspect ratios is beneficial for film cooling. It should be pointed out, however, that in their experiments, the cross-sectional areas of the holes are not kept constant. As a consequence, as the aspect ratios increase, so do the cross-sectional areas and the corresponding mass flow rates of the coolant.

Trapezoidal holes studied by Makki and Jakubowski (1986), and Takeishi (1995), were found to have improved cooling effectiveness compared to conventional round holes. More complex shapes were investigated by Papell (1984), Wu, Vakili, and Yu (1988), and Liscinsky, True, and Holdeman (1995). Papell used a cusped hole having a kidney-shaped contour. He compared the film effectiveness of a round hole to that of the cusped hole oriented with the cusp toward the leading edge ('top' cusp) and the cusp toward the trailing edge ('bottom' cusp). In general, the top cusp design shows the highest film cooling effectiveness, the bottom cusp the middle, and the round the lowest. In the near field, however, a reversal occurs: the bottom cusp becomes better than the top cusp. This reversal becomes increasingly evident for the higher blowing ratios.

For injection in gas turbine combustors, Liscinsky, True, and Holdeman (1995) investigated six shaped holes at a blowing ratio of 2.9: round, square, ellipse (minor axis aligned along the crossflow), ellipse 90° rotated (major axis aligned along the crossflow), high aspect-ratio rectangle with rounded corners, and low aspect ratio rectangle with rounded corners. For all holes there is no change in passage cross-sectional area. The conclusion they draw from their planar Mie scattering results is that at this high blowing ratio, the mean trajectories are similar, independent of hole shape.

Theoretical modelling of the crossflow jet trajectory may be classified into three categories: integral approach, kidney-pair representation, and vortex sheet modelling. The integral approach, adopted in the plume studies of Hoult and Weil (1972), Adler and Baron (1979), and Schatzmann (1979), uses a control volume constructed at the jet-crossflow interface to balance the momentum brought by entrainment, the pressure gradient across the jet, and the centrifugal force associated with jet bending. In addition, Adler and Baron, and Schatzmann considered the effect of the kidney-vortices upon the entrainment of momentum. In contrast to the integral approach, which necessarily involves many empirical constants, the kidney-pair representation adopted by Durando (1971), Broadwell and Breidenthal (1984), and Karagozian (1986) requires fewer constants, since the representation applies to the far-field where pressure the difference across the jet and centrifugal force vanish. Coelho and Hunt (1989) modelled the jet-crossflow interface as a three-

dimensional vortex sheet, which acts as a sheet of sinks as well as vortices: the sinks simulating entrainment.

The question regarding the origin of the kidney-pair for the round hole was addressed in varying degrees by Moussa, Trischka, and Eskinazi (1977), Andreopoulos and Rodi (1984), Sykes, Lewellen, and Parker (1986), Fric (1990), and Sugiyama (1991). With the exception of Sugiyama (1991), who appropriates the kidney-vortices to the crossflow entrained into the leeside of the jet, they all attribute the origin to the pipe sidewall boundary layer in the same manner as originally proposed by Scorer in 1958. Shi, Wu, and Wu (1991) ascribe the origin to the crossflow in a way similar to Sugiyama (1991) as well as to the pipe sidewall boundary layer. The important question of what happens to the other parts of pipe boundary layer, such as those at the leading and trailing edge, the vorticity of which is aligned transverse to the flow, is either left unanswered or explained by appealing to the vorticity cancellation process originally proposed by Scorer (1958). There does not appear to be a study which tracks the various circumferential parts of the pipe boundary layer after the jet is discharged into crossflow.

1.4 Definition, Organization, and Scope of the Present Research

In light of the past research, it is evident that cooling hole geometry alone can influence the jet cooling effectiveness. For shaped holes, these benefits have been attributed to the reduction in effective blowing ratio by increasing the hole exit area. While this is certainly true, the data of figure 8 by Goldstein *et al.* (1974), suggest that there is more than just the slowing down of the coolant: the film cooling effectiveness for a shaped hole, even when adjusted at a blowing ratio based on the exit velocity, is greater than that for a round hole at the equivalent blowing ratio. Where does this difference arise? We believe that the additional benefit for the shaped hole is attributable to the departure of its hole exit geometry from the round hole, which could change the kidney-vortices significantly.

Since film effectiveness is linked to jet lift-off, and jet lift-off to the kidney-vortices, an investigation of the effect of hole geometry on film effectiveness should begin with a

study to determine how, for holes having constant passage area, hole exit geometry alone affects the kidney-vortices.

The past research, aimed at understanding the kidney-vortex structures, has been limited primarily to round holes. The commonly held view that the kidney-vortices are formed from the hole side-wall boundary layer only, and that the leading and trailing edge boundary layers have no additional contribution, is a question that must then be addressed. The question of what vorticity comprises the kidney-vortices becomes more complex when one considers that any vorticity can be turned in the flow. This is an important consideration, especially at the leading edge of the jet, where the momentum of the crossflow is entrained into the jet, which may deform and realign vortex filaments in the boundary layer. Even at the trailing edge, the reverse flow may cause a similar effect.

For the round hole, the realignment of leading and trailing edge boundary layer vorticity is extremely difficult to detect since the hole curvature make these contributions indistinguishable from the side-wall vorticity. Therefore investigations into the contributions of the leading and trailing edge boundary layer should begin by examining hole geometries such as a square or rectangle, which more clearly separate the leading and trailing edge vorticity from the side-wall vorticity.

By the use of these simpler geometries, the following questions can be addressed: 1) Can the geometry alone influence lift-off without the need to manipulate the hole cross-sectional area? 2) Do the leading and trailing edge boundary layers simply cancel each other, or do they modify the effect of the side-wall boundary layer to influence jet lift-off? 3) Can these fundamental results be used to diagnose and evaluate the more complex holes actually used in industry - even with their complex variations in hole passage cross-section and inclined injection?

These questions provide the framework for the present investigation. Question (1), the effect of hole geometry on lift-off is presented first in §3 after the description of the experimental facilities and techniques in §2. In §3, the hole geometry is systematically changed in such a way as to alter the lateral separation of the side-wall kidney-vortices. The results provide compelling evidence that jet lift-off can be suppressed by geometry alone, without enlarging the jet passage.

Question (2), the contributions of the leading and trailing edge boundary layers to the kidney-vortices, will be examined first by analyzing a model problem of a heuristic nature in §4. This analysis shows that the entrainment of crossflow momentum by the jet can cause the realignment of the jet vorticity by warping the leading edge and trailing edge vorticity, and by tilting the side-wall vorticity. Following this analysis, a detailed study on the observed vortical structures is presented in §5 to provide the background necessary to interpret the experimental results of §6. In §6, the flow structures for different hole geometries will be examined in detail by the use of particle image velocimetry, which enables us to dissect and quantify the complex flow field. Here, the realignment of leading and trailing edge vorticity is found to act as an addition to, or subtraction from, the side-wall kidney-vortices. When the realignment of the leading edge, or trailing edge, vorticity toward the streamwise direction is such that the rotational sense is the same as the kidney-vortices, this additive pair is termed a 'positive' pair. When realignment results in a vortex pair rotating in the direction opposite to the kidney-vortices, it is termed a 'negative' pair. The hole geometry appears to be the discriminator between the cancelling 'negative' pair, or the reinforcing 'positive' pair. In light of this, the previously held view that the leading and trailing edge boundary layers simply annul each other needs to be substantially altered: they, instead, actively engage in the formative process of the kidney-vortices. This includes, as a special case, the much studied round hole.

In §7, which is related to question (3), the insight gained from the basic geometries tested in §6, will be used to interpret the experimental results for three industrial geometries. The hole designs were made available to us by courtesy of IHI Ltd., Tokyo, Japan. These results make more transparent the competing influence of the 'negative' and 'positive' vortex pairs in controlling jet lift-off.

The general scope of study is limited to a single jet in a crossflow. With the exception of the IHI holes, jet injection is normal to the crossflow. All testing was done using water as the jet and crossflow fluid. Since the density of both fluids is the same, the blowing ratio can more simply be expressed at a velocity ratio: $BR = U_j/U_\infty$. The range of blowing ratios using throughout the experiments is 0.4 to 2.0.

The field of study is restricted to the vicinity of the hole, including the flow immediately over the hole. First, this is motivated by our interest related to the jet attachment: if the jet could not cover the proximity of the hole, the very objective of film cooling would not be met. Second, the basic character of the kidney-vortices is established near the hole exit where the jet and the crossflow make physical contact with each other. By the time the jet is several diameters downstream of the hole, all the jet vorticity has merged into the conventional kidney-vortex structures. The wake vortices shown by Fric (1994) are then the only mechanism by which additional vorticity can enter the jet. This means that once the jet leaves the very near wake field region, the basic character of the jet has been established.

Chapter 2: Experimental Facility and Techniques

Flow visualization in water, coupled with quantitative velocity measurements were the techniques used to interrogate the fluid dynamics of a jet in a crossflow. Flow visualization using Laser Induced Fluorescence (LIF) was used to examine the basic vortical structures of the jet in the plane illuminated by a sheet of laser light. Particle Image Velocimetry (PIV) provided the two-dimensional velocity field, from which the corresponding vorticity component perpendicular to the plane was calculated. Although the use of PIV enabled us to acquire important quantitative data, the resolution imposed by the camera pixel field limits its capability to capture fine-grained vortical structures as sharply as LIF does. This chapter contains a brief description of the water tunnel facility and jet supply system, and the set up for both the flow visualization and PIV systems.

2.1 Water Tunnel and Jet Supply System.

The water tunnel shown in figure 2-1 is a closed circuit recirculating facility with a 3.0m x 0.7m x 0.7m glass test section. The tunnel maximum speed capability is 70 cm/s, with a free stream turbulence level approximately 0.3% of the mean flow for all tunnel speeds. A detailed description of the facility is given by "Eroglu (1991). All experiments were conducted below a tunnel speed of 10 cm/s.

An acrylic flat plate 1.0 m x 0.5 m was suspended in the test section approximately 7 cm below the free surface of the tunnel. Two plate configurations were used which differed in the distance from the leading edge of the plate to the jet. For the flow visualization experiments, the jet was located 26 cm from the leading edge. Due to imaging consider-
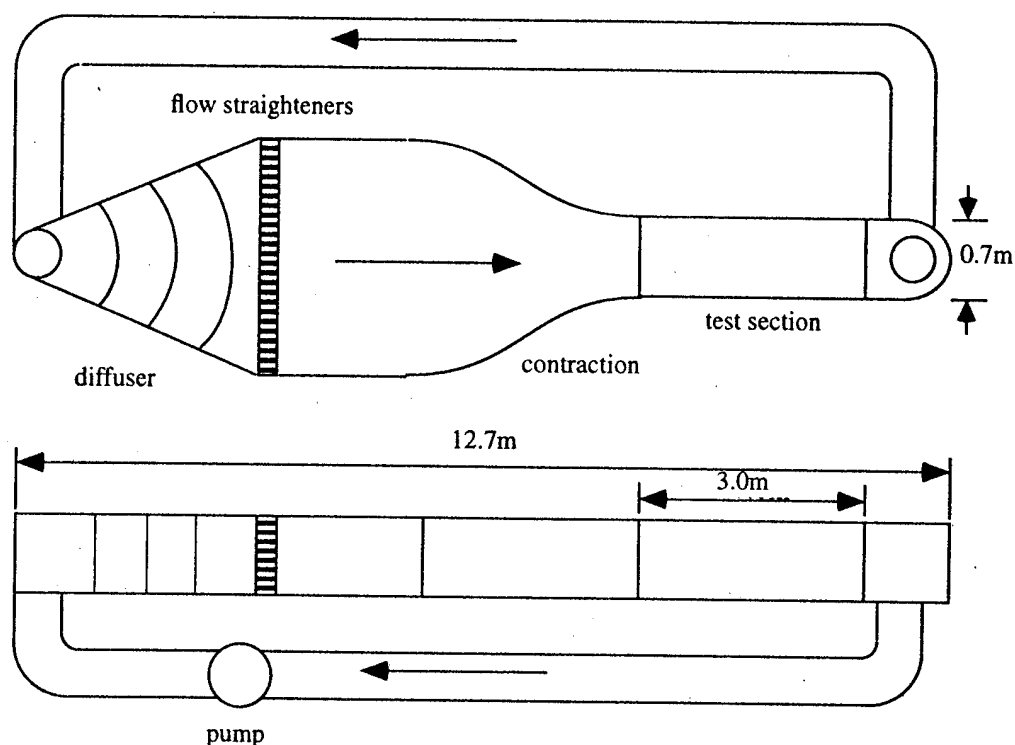
Figure 2-1: University of Washington Water Tunnel Facility.

ations with the PIV system, the hole position was moved further downstream to a location 52 cm from the plate leading edge. The boundary layer thickness, δ, was estimated using the Blasius solution for flow over a flat plate: $\delta \approx 5\sqrt{vx/U_\infty}$. For a crossflow velocity of 8 cm/s, the approximate boundary layer thickness at 26 cm and 52 cm downstream is 0.9 cm and 1.3 cm, respectively.

The jet fluid supply system, shown in figure 2-2, consists of a 200 liter preparation tank, 120 liter pressurized supply tank, metered flow valves and a small settling chamber prior to the hole passage. The settling chamber and hole passages were fabricated from acrylic. A more detailed description of the jet supply system is given by Simpson (1995). The jet fluid for the laser induced fluorescence experiments was prepared by mixing 2 x 10^{-4} grams of disodium fluorescein per liter of water. For the PIV experiments, the water in the preparation tank was seeded with 4 μm nylon spherical particles at approximately 7 x 10^{-4} grams per liter of water. The specific gravity of the nylon particles is 1.02.

from building air supply

metered flow valves

to vacuum pump

pressurization
reservoir

settling
chamber

different
geometries

flat plate

crossflow

jet

to water source

manifold
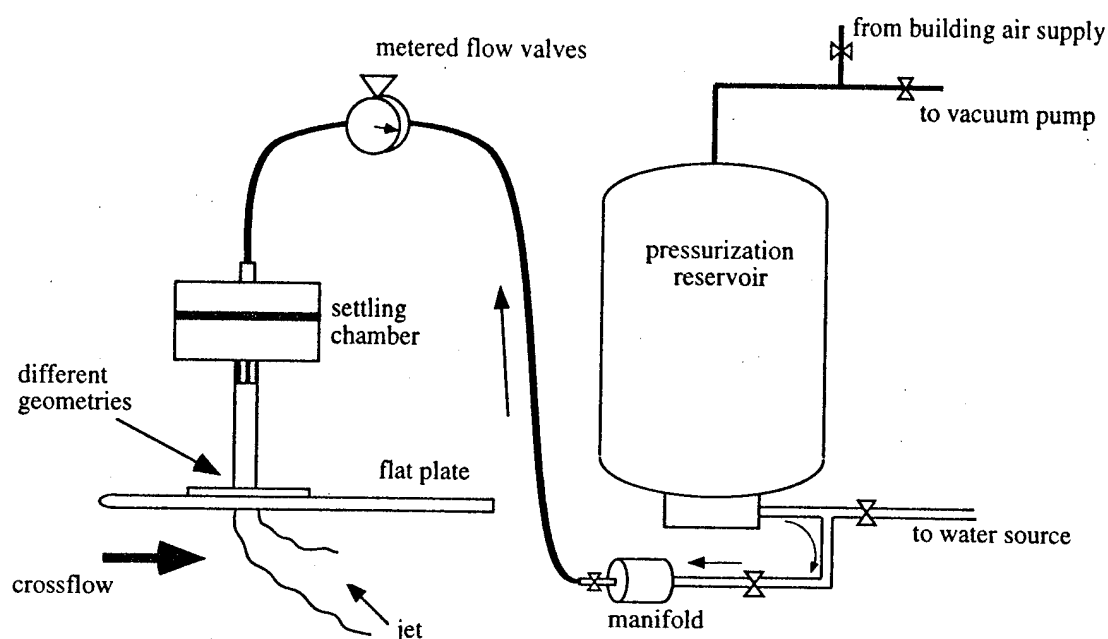
Figure 2-2: Jet Fluid Supply System.

2.2 Laser Induced Fluorescence Technique

The laser sheeting technique, laser induced fluorescence, used a laser sheet generated by a nominal 5 watt argon ion laser (Spectra Physics Model 2020-5) and a 1200 Hz scanning mirror (General Scanning Model IDS-2512) to illuminate the jet fluid. The jet fluid, seeded with disodium fluorescein, fluoresces when excited by the green (514.5 nm) laser light. As the laser sheet intersects the jet, the fluorescing fluid shows up as a white image when recorded by a Cohu 4910 series RS-170 CCD (charged couple device) camera. The images from the camera were recorded on video tape using a SVHS video recorder. From the tape, the images were digitized using a frame grabber then stored in a computer.

The laser sheet was oriented along three different planes to view clearly the jet trajectory and discern the vortex structures within the jet in the planes parallel and perpendicular to the plate as shown in figure 2-3. The general layout for the flow visualization experiments is illustrated in figure 2-4.

jet trajectory   perpendicular plane   parallel plane

laser sheet

viewing direction

laser sheet

laser sheet

viewing direction

x-z plane   y-z plane   x-y plane

(a)   (b)   (c)
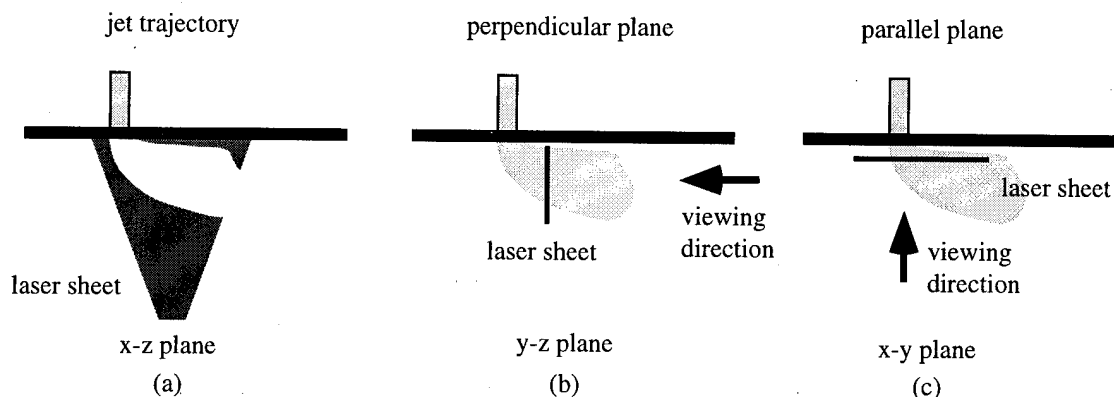
Figure 2-3:   Laser Sheet Orientation

test section   CCD camera

flat plate

camera mirror

laser sheet

crossflow

scanning mirror

mirror   focusing lens   laser
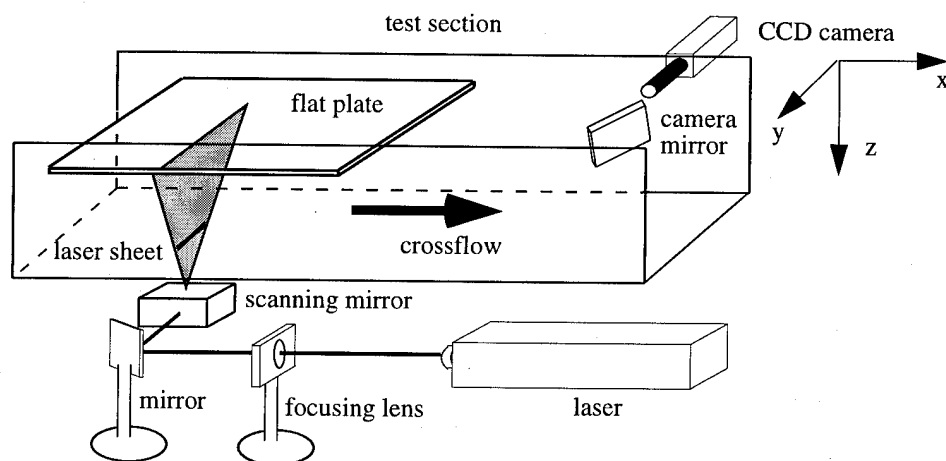
Figure 2-4:   Flow Visualization Set-up using Laser Induced Fluorescence.

To record the images as the jet passed through the laser sheet, the camera had to be placed perpendicular to the image plane. This was difficult when the laser sheet was oriented perpendicular to the sides of the tunnel (figure 2-3b). To avoid placing the camera in the test section, a small mirror, 5 cm x 5 cm, was located downstream of the plate at a 45 degree angle. The camera was then positioned outside the tunnel and the image recorded off the mirror.

2.3 Particle Image Velocimetry (PIV)

Quantitative flow field measurements were acquired using a TSI Incorporated Particle Image Velocimetry (PIV) system. PIV is a non-intrusive optical imaging technique which measures the planar displacement of particles within a flow field over a given time. This technique allows for the simultaneous acquisition of hundreds of velocity vectors at any location in the flow field by illuminating the area of interest using a laser sheet then recording the particle images with a camera as the fluid passes through the laser sheet. The laser sheet was oriented along the same planes described in figure 2-3. Again, a mirror was used downstream of the plate to record the jet cross-section in the y-z plane (figure 2-3b). For the best results, the PIV image must fill as much of the video frame as possible. The distance between the camera and the image becomes more of a factor than for laser induced fluorescence. The original jet location of 26 cm from the leading edge of the plate caused the image to be too small when viewed from the downstream mirror. To resolve this problem, the hole was moved further downstream to 52 cm, which shortened the distance between the image and the camera.

The velocity is obtained by measuring the particle displacement within the laser sheet between two lasers pulses. The particle locations, corresponding to each laser pulse, are recorded on a separate video frames using a modified CCD camera. A cross-correlation algorithm is then run on each pair of images to determine the particle displacement in pixels.

2.3.1 Basic System Components

The PIV system is comprised of a laser, beam modulator, synchronizer, light sheet optics, camera, and computer (figure 2-5). The laser is the same 5 watt argon ion laser used in the flow visualization experiments. After the installation of a new plasma tube prior to purchasing the PIV system, the maximum output of the laser prior to entering the beam modulator was increased to approximately 8 watts.

The beam from the laser passes through a collimating lens into the beam modulator (TSI Model 620010). The beam modulator uses the first order beam from a Bragg cell to
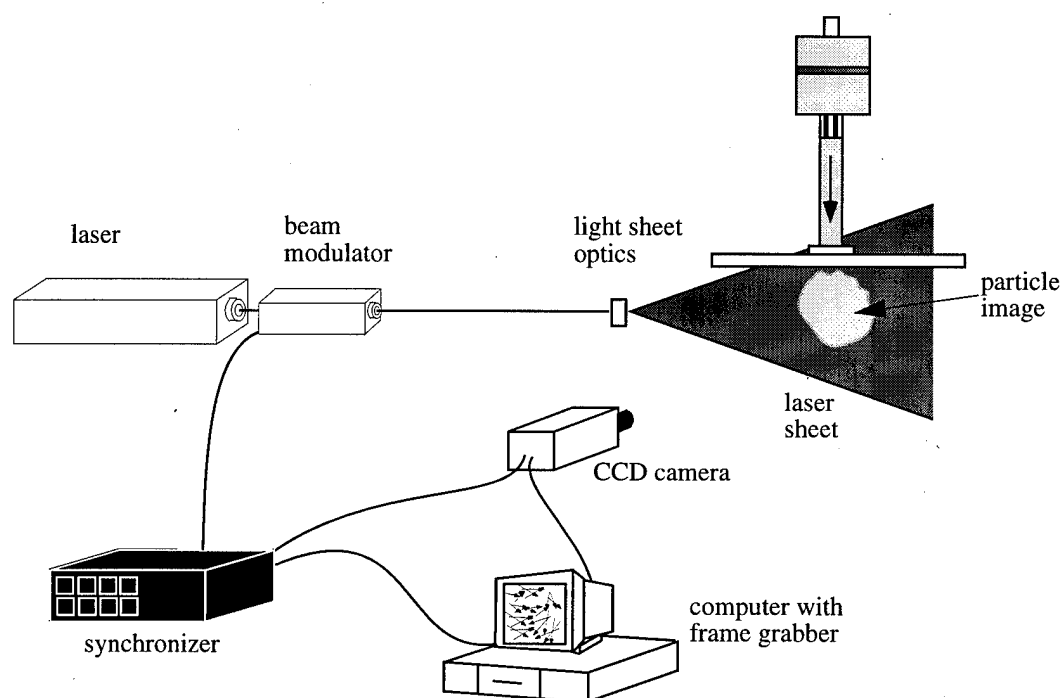
Figure 2-5: Particle Image Velocimetry Set-up

turn the laser beam on and off. It is important that only the first order beam is allowed to pass through the knife-edge at the modulator's outlet in order to obtain a coherent light sheet for illuminating the flow; using any other order beam results in a color separation of the laser beam. The details regarding the set up of the modulator can be found in the TSI Instruction Manual. A 40 MHz signal was sent from the synchronizer (TSI Model 610030) to control the beam modulator.

The synchronizer provides the signaling control for the laser beam modulator and camera. For two video frame cross-correlation, the synchronizer settings are shown in table 2-1 (TSI PIV Instruction Manual, 1995).

To generate the laser sheet, the beam was directed through a cylindrical and spherical lens combination. The focal length of the cylindrical lens is -12.7 mm, providing a 30 degree divergent sheet. A spherical lens having a focal length of 500 mm was used to focus the laser sheet near the region of interest. The resulting laser sheet thickness at the waist of the sheet was approximately 0.2 mm.

Table 2-1: Synchronizer Parameter Setup

Synchronizer Button	Parameter Settings	Description of Parameter
Pulse		
Mode	Pulse Mode Double Pulse	Generates two pulses at the programmed separation time
Laser Type (2nd Function)	Argon	Type of laser being used
Duration	Pulse Duration 50% Duty Cycle	Time the laser is on during a pulse (percentage of the pulse separation time - 50% maximum)
Separation	Pulse Separation 0.0015 s	1.5 ms separation between two consecutive laser pulses
Camera		
Mode	Video Camera Triggered	Allows the camera to be the timing master
# of Frames	00 Frames	Camera is fired continuously until RUN/STOP button is pressed
Frame Rate	N/A	Does not apply to video triggered mode
Pulse Delay (2nd Function)	Pulse Delay Time 49 ms	Used with Pulse Separation of 1.5 ms. See Instruction Manual, pg 4-4, for approximate pulse delays for other pulse separations
External		
Start	00 Seconds	
Stop	00 Seconds	
Trigger		
Run/Stop		Activates laser pulsing
Int/Ext	Trigger Source Internal	Set to internal when no image shifting is being used.

The camera (TSI Model 630044) is a CCD video camera having a frame rate of 30 frames per second and a resolution of 640 pixels horizontally and 480 vertically. The camera was modified to eliminate the interlaced video output problems associated with standard CCD camera. The camera allows for two different images to be recorded on two consecutive video frames on the order of 0.02 ms apart. This is done by exposing the entire CCD array at the very end of one frame, transferring that signal to the in camera

memory, then taking a second exposure very near the beginning of the next video frame. The two video frames are then transferred to the computer and stored in the frame grabber memory. A total of 13 consecutive images could be stored in the available frame grabber memory. The camera was originally equipped with a 4:1 zoom lens. This lens was replaced by a longer focal length Nikon Macro lens (AF Micro-Nikkor, 105 mm, f/2.8D) having a maximum magnification of 10:1. The long focal length was needed to focus on the images appearing in the y-z plane because of the additional focusing distance introduced by the mirror. The macro lens was used for the majority of the PIV experiments.

The computer is a 90MHz Pentium equipped with four dedicated math accelerator boards for efficiently computing FFTs (Fast Fourier Transforms). Two dimensional FFTs are performed on each video image to determine the location of the peak particle intensities for a given interrogation area. The displacement, in pixels, of these intensity peaks from one video frame to the next is then obtained by comparing the two dimensional FFT results for the two frames. Once the particle displacements have been calculated, post-processing was done using two TSI software packages: Insight^{TM} and Datashow^{TM}.

Insight^{TM} governs the acquisition and processing of the particle displacements from the raw image data. The software processing setup used for the majority of experiments is shown in table 2-2.

Table 2-2: Insight^{TM} Software Processing Setup

Setup Parameter	Setting	Explanation
Peak Search Algorithm	Gaussian	Best Algorithm for Argon laser
Signal Levels		Signal-to-noise ratio (SNR) is mainly a function of the number of "paired" particles within an interrogation region
SNR #1	0.05	D.C. peak vs. highest data peak amplitudes
SNR #2	1.25	Data peak vs. second highest peak amplitudes - determines validity of a displacement
SNR #3	0.10	Ratio of total energy under data peak to total energy in auto-correlation excepting the D.C. peak
Signal Cutoff	10	

Table 2-2: Insight^{TM} Software Processing Setup

Grid		
Spacial Resolution	40	Interrogation region size: 40x40 pixels
Aspect Ratio	0.98	Adjusts for digitized images not having exactly square pixels
x-grid	32	x and y grid - gives 50% overlap between adjacent interroga-
y-grid	22	tion regions
x_{min}	20	Used to specify the minimum and maximum corresponding
y_{min}	20	to an area-of-interest calculation
x_{max}	620	
y_{max}	460	

The Insight^{TM} software offers a choice of four search algorithms to determine the location of the peak particle intensities with sub-grid accuracy: Centroid, Parabolic, Whittaker, and Gaussian. The Centroid algorithm was rejected because it is designed to be used with interlaced video images. The images from the TSI Camera are non-interlaced images. During the setup of the system, the Parabolic and Whittaker search algorithms gave results which differed by 9% and 8%, respectively, when measurements of the same flow field were taken at different laser pulse settings. The Gaussian search algorithm was selected because it repeated values within 1% of the mean velocity for nine different laser pulse separation-times between 1.3 ms and 2.6 ms.

Datashow^{TM} was used to post-process the pixel displacement fields calculated in Insight^{TM}. The displacement vectors were first validated to remove the obvious bad vectors. During validation, the local average x and y pixel displacements are computed. The difference between the local average and the point displacement is compared against a threshold value. Values exceeding this threshold are removed from the data set. The 'Find Holes' command is used to interpolate the displacement vector field and replace bad vectors with interpolated vectors. The algorithm locates the positions of 'good' vectors in the neighborhood of the vectors removed during validation or dropped due to a low signal-to-noise ratio during processing. A least squares curve-fit is performed using the neighboring vectors to give an estimate of the displacement for the missing data point.

The individual vector files, after being processed by Datashow^{TM} can be averaged, provided the files are the same size. A typical averaged file presented in these results is
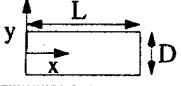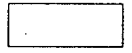
made using between three and six individual vector files. The time to process a single image pair made it prohibitive to average routinely a larger number of files.

Further processing of the displacement fields enabled the calculation of velocity and vorticity. The displacement vector data was read into the program Transform^{TM}, where it was converted first into velocity, then into vorticity using a finite difference scheme to approximate the cross-derivatives, $\frac{\partial v}{\partial x} - \frac{\partial u}{\partial y}$. Color and graphical presentation of the velocity and vorticity fields was accomplished using Transform^{TM} in conjunction with the three-dimensional graphics package, Slicer^{TM}. Slicer^{TM} enabled the simultaneous presentation of multiple files generated by Transform^{TM}.

2.4 Hole Configurations

The hole geometries used throughout the experiments are shown in table 2-3.

Table 2-3: Hole Configurations

Hole	Hole Shape	Dimensions (cm) D x L	Length (normal to page) (cm) H	Aspect Ratio (AR) AR = $\frac{D}{L}$
1		1.34 x 3.66	25	0.37
2		1.75 x 3.50	25	0.5
3		2.48 dia	27	1
4		2.19 x 2.19	25	1
5		3.50 x 1.75	25	2.0
6		3.66 x 1.34	25	2.7
1a		1.95 x 5.27	14	0.37
2a		2.54 x 5.08	17	0.5
4a		3.20 x 3.20	14	1
5a		5.08 x 2.54	17	2
6a		5.27 x 1.95	14	2.7

The first six holes all have the same exit area. The majority of flow visualization experiments and all of the PIV experiments were accomplished using these six holes. The remaining five holes are scaled-up versions of the original six. These larger holes were used to obtain a better look at the smaller vortical structures within the jet. The flow visualization pictures associated with these larger hole configurations will be used to supplement the PIV and flow visualization results for the first six holes listed in table 2-3.

The uniformity of the flow exiting three of the holes was examined by obtaining the free jet velocity profile (i.e. $U_\infty = 0$) along the centerline of the hole. This was to determine how much, if any, skewing of the velocity profile was caused by the settling chamber. Figure 2-6 contains the velocity profiles for a number of nominal jet velocities which were obtained just outside the hole exit. Each profile was obtained by averaging six consecutive instantaneous vector files. For the most part, the profile is uniform over the exit, suggesting the settling chamber is introducing essentially no bias into the crossflow jet measurements.
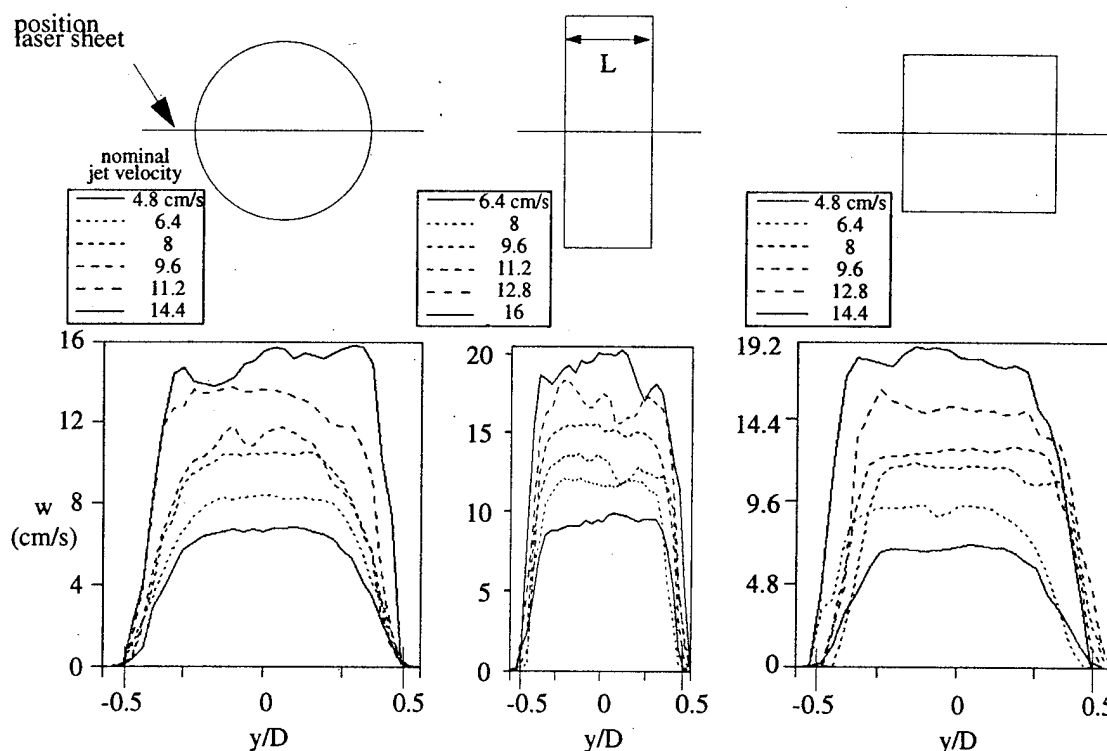
Figure 2-6: Free Jet Velocity Profiles for Holes 1, 3, and 4; $Re_L = U_jL/\nu$ Range is from 850 to 3540

2.4.1 Non-Dimensionalization

Non-dimensionalization of the quantitative measurements will be accomplished using the following presented in table 2-4. The characteristic length used to non-dimensionalize the

Table 2-4: Non-Dimensional Parameters

Quantity	Dimensional Designation	Multiplier	Non-Dimensional Designation
x-direction	x	$1/L$	x'
y-direction	y	$1/D$	y'
z-direction	z	$1/D_{hole3}$	z'
u-velocity	u	$1/U_\infty$	u'
v-velocity	v	$1/U_j$	v'
w-velocity	w	$1/U_j$	w'
Vorticity	ω	D_{hole3}/U_j	ω'

z-direction and vorticity was arbitrarily chosen as the diameter of the round hole, D_{hole3}. The reason for this selection was to allow for the recalculation of the vorticity directly from the value of ω' without the need to know the contributions from each of the non-dimensionalized derivatives, since they are non-dimensionalized with different character-istic lengths. Also, the z-locations for the laser sheet were the same for all holes; therefore, one consistent length scale was desired to facilitate comparison of data for the different holes.

For all experiments using holes 1 through 6 in table 2-3, the crossflow was maintained at 8 cm/s. The blowing ratio is therefore proportional to the jet velocity, $BR \propto U_j$. For holes 1a through 6a, the crossflow velocity was reduced to 5.4 cm/s in order to attain the same blowing ratios with the existing jet supply system.

Chapter 3: Effect of Hole Geometry on Jet Trajectory

We investigate here how changes in the exit geometry of holes alter the attachment of jets to the surface.

3.1 Kidney-Vortices Due to Side-Wall Vorticity

According to the view initially proposed by Scorer (1958), kidney-vortices are the downstream manifestation of vorticity initially arising from within the side-wall boundary layer of the hole passage. As illustrated in figure 3-1 for a rectangular hole geometry, the side-wall of the hole generates vorticity aligned with the x-direction. This vorticity then shows up in a laser sheet oriented in the y-z plane as the kidney-vortices, represented as $(\omega_x, -\omega_x)$.
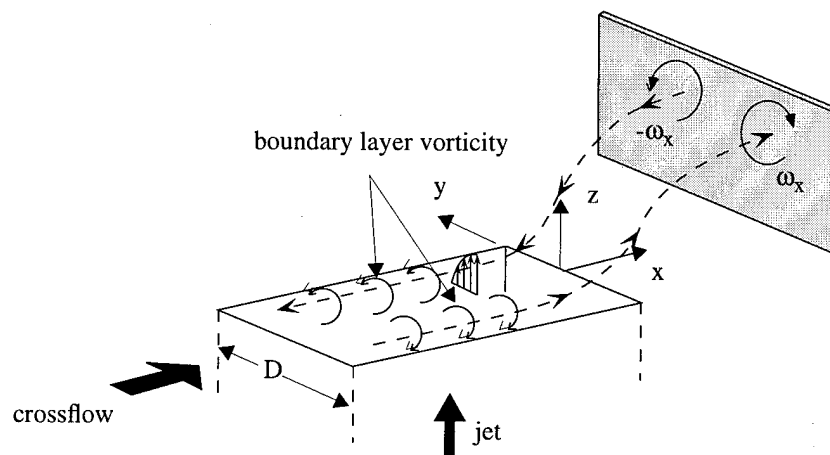
Figure 3-1:   Kidney-Vortices due to Hole Side-Wall Vorticity

A more precise description, however, must also consider vorticity which is not initially aligned in the x-direction. All vorticity originating within the hole is subject to twisting and turning as the jet interacts with the crossflow. This means that vorticity generated on the front and back walls of the hole, though not initially aligned in the x-direction, can be turned such that additional x-components of vorticity appear in the y-z plane. The crossflow boundary layer can likewise be realigned due to the interaction with the jet. We shall return to the subject of vorticity realignment later as it has an important bearing on the lift-off behavior of the jet. For now we will ignore this realigned vorticity and proceed by focusing attention on the hole side-wall boundary layer.

3.2 Link Between Kidney-Vortices and Jet Lift-Off

When we examine only the vorticity generated by the side-wall of the hole, it is reasonable to expect that the lateral separation of the kidney-shaped vortices can be manipulated by changing the hole geometry: even for the same cross-sectional hole area, the larger the cross-stream dimension of the hole, D, such as in the case of hole 6, the larger the lateral distance separating the kidney-shaped vortices (figure 3-2). The increased separation decreases the mutual induction due to the vortex pair; the net result is that the jet tends to stay near the surface. On the other hand, as the kidney vortices are brought closer by decreasing the cross-stream dimension, as in the case of hole 1, the mutual induction increases and the jet lifts off the surface. By proceeding along this line of reasoning, one
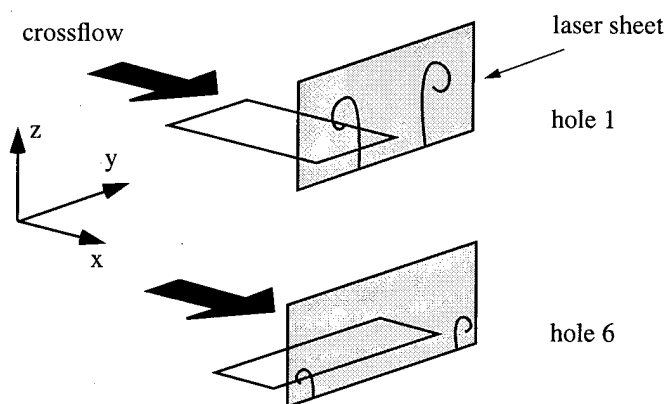
Figure 3-2:   Kidney-Vortices due to Hole Side-Wall Vorticity

can arrive at the 'spectrum of shaped holes' displayed in figure 3-3 for holes 1 to 6. Note here that the cross-sectional areas of all holes are the same.
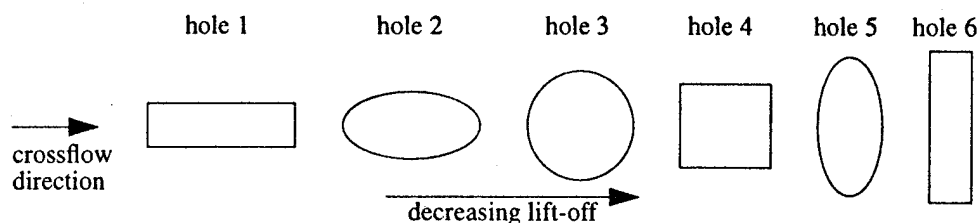
Figure 3-3: Trend of Jet Lift-Off with Geometry

Confirmation of these trends is shown in figures 3-4 through 3-6. The blowing ratio corresponding to these figures is 1.6. Figure 3-4 is the view perpendicular to the crossflow which shows the kidney-vortices that appear at the downstream side of the hole, $x' = 1$. Distinct vortex structures are evident for each jet configuration (pictures in figures 3-4 and 3-5 correspond to the view depicted in figure 3-2). Even a casual inspection of figures 3-4 and 3-5 reveals that vortical structures appear to be stacked on top of one another: they are labelled as 'steady' and 'unsteady' vortices. The 'steady' structures can be seen as the lowermost vortices, with the 'unsteady' vortices riding over the top of the 'steady' ones. We defer their discussion to §5.

As previously mentioned, the lift-off of the jet is expected to be affected by the lateral position of these vortices with respect to each other. This can be seen in figure 3-5 as the laser sheet is moved 5.08 cm downstream of the hole trailing edge. Comparison of hole 1 with 6, shows a marked decrease in the jet lift-off. The mutual induction between the kidney-vortices for hole 1 is responsible for the dark crossflow boundary layer fluid being drawn into the bottom part of the jet.

The trajectory along the jet centerline in the x-z plane, shown in figure 3-6, confirms the change in lift-off behavior seen in the cross-sectional views of figures 3-4 and 3-5. For holes 1 through 6, there is a progressive increase in the degree of jet attachment to the wall. It is important to emphasize that this change in the lift-off behavior is not brought about by any enlargement of the hole passage, but only by the change in the two-dimensional geometry of the hole.
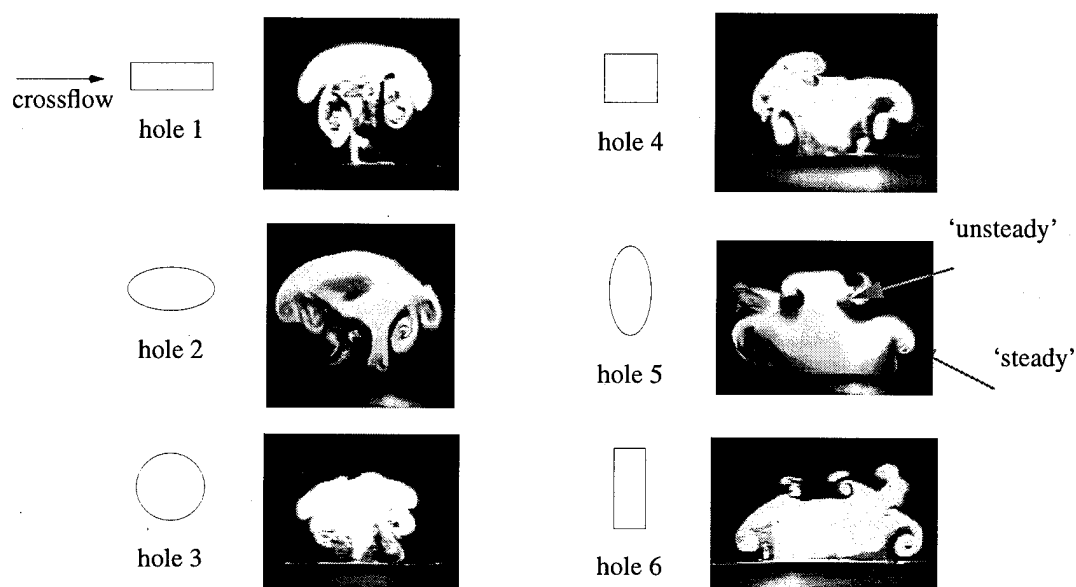
Figure 3-4: Kidney-Vortices at Downstream Edge of Hole, BR = 1.6
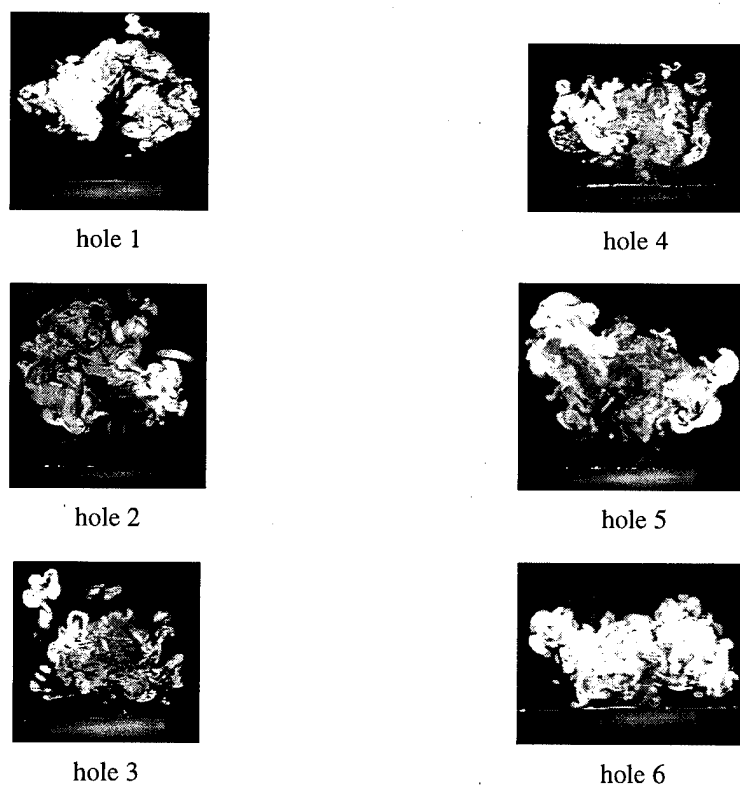
Figure 3-5: Kidney-Vortices at 5.08 cm Downstream of Hole Trailing Edge, BR = 1.6

hole 1

hole 4

hole 2

hole 5

hole 3

hole 6
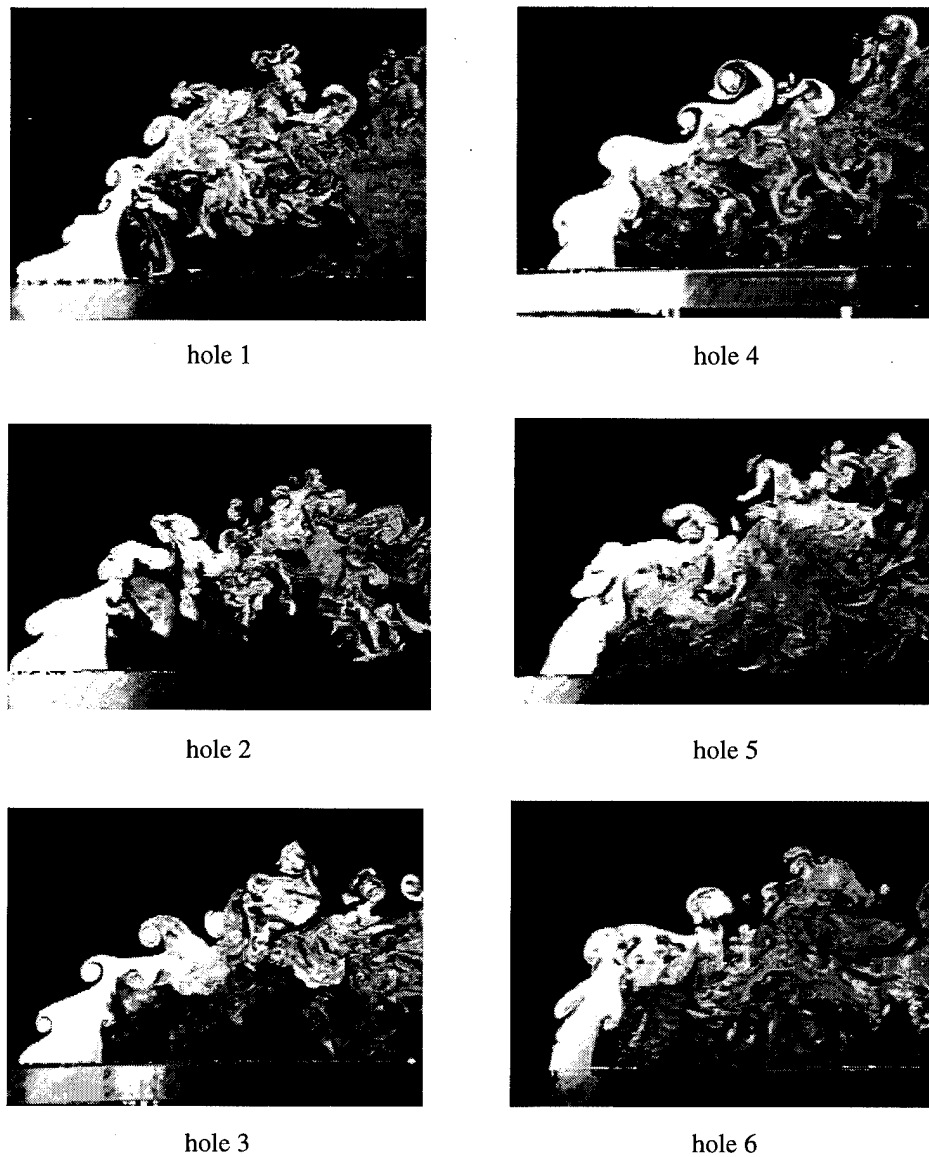
Figure 3-6: Jet Trajectory along Centerline for BR = 1.6

By coincidence, Liscinsky, True and Holdeman (1995) also investigated holes of similar shapes. Contrary to our results at a blowing ratio of 1.6, they did not find any noticeable difference in jet trajectory at a blowing ratio of 2.9. Obviously, once the jet is blown off the surface at the higher blowing ratios, the hole geometry appears to have little effect on the subsequent behavior of the jet.

Chapter 4: Theory - Vorticity Realignment

We now direct our attention to the vorticity realignment briefly touched on in §3.1, and start by considering the leading edge boundary layer as it emerges from the hole. When we construct a control surface at the interface of the frontal part of the jet and the crossflow (figure 4-1), the momentum entrained from the crossflow into the jet acts as the surface force imposed on the jet. Since the entrained momentum, or the surface force, varies from the jet center to its edge, the interface warps in the direction normal to the paper.
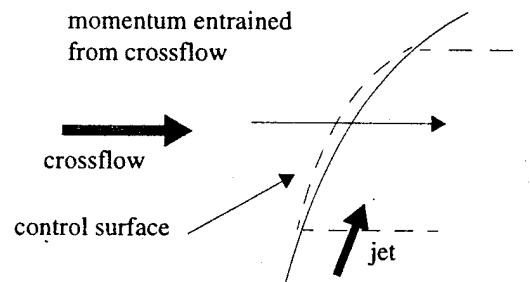
Figure 4-1:   Control Surface at the Jet - Crossflow Interface

A consequence of the warping is this: as shown in the analysis to be developed here and substantiated later in §5 and §6, the vorticity within the deformed interface can realign itself to induce a 'negative' pair, that is, a vortex pair that has a rotational sense opposite to the kidney-vortices, or 'positive' pair. The 'negative' and 'positive' pairs can potentially annihilate each other either by direct contact or cross-diffusion, the net result of which can reduce the detrimental effects of the kidney-vortices. For this annihilation to occur, however, the opposing vortices must be close enough to interact with the kidney-vortices. As the 'negative' pair is brought closer to the kidney-vortex pair, the mutual induction

between the kidney-vortex pair is suppressed as shown in figure 4-2. As the vortices move closer, the vortex structures combine into a single vortex pair having a reduced vorticity compared to the original kidney-vortices.

mutual induction by 'negative' pair

vorticity reduced through annihilation

'negative' pair

$+\omega_{x,1}$ $-\omega_{x,2}$ $+\omega_{x,2}$ $-\omega_{x,1}$

$+\omega_{x,3}$ $-\omega_{x,3}$

kidney-vortices

mutual induction by kidney-vortices

$+\omega_{x,3} = (+\omega_{x,1}) + (-\omega_{x,2})$

$-\omega_{x,3} = (-\omega_{x,1}) + (+\omega_{x,2})$
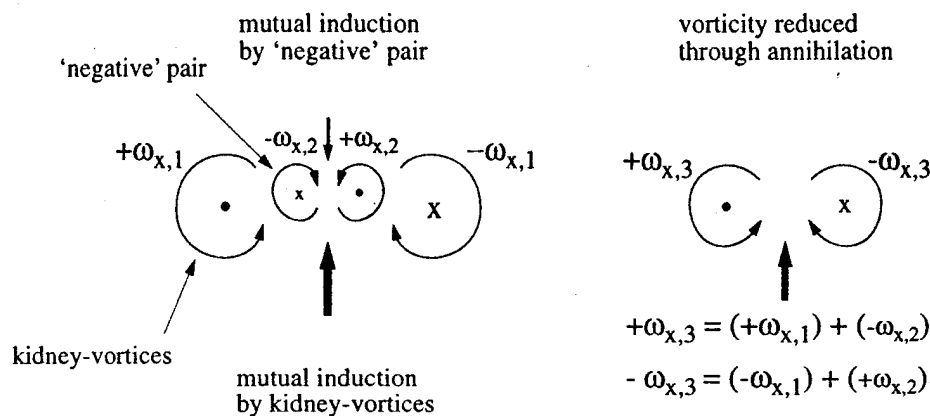
Figure 4-2: Vorticity Cancellation through Annihilation

Even for the trailing edge boundary layer, reverse flow present in the wake causes similar warping and the resultant 'negative' pair (§6). A simple heuristic model problem for the warping of the leading and trailing edge vortex sheets is presented here to illustrate how the 'negative' pair can result from the realignment of the jet boundary layer vorticity.

4.1 Governing Equations

The dynamic equation that governs the distribution of vorticity in the flow field corresponding to the experimental studies is the incompressible vorticity transport equation given by (4-1). This equation is obtained by taking the curl of the momentum equation under the assumptions that the flow field is incompressible, barotropic, and isothermal.

$$\frac{D\vec{\omega}}{Dt} = (\vec{\omega} \bullet \vec{\nabla}) u + \nu\nabla^2\vec{\omega} \qquad (4\text{-}1)$$

This equation states that the rate of change of a particle's vorticity is equal to the vorticity increase due to vortex stretching and turning (or decrease due to vortex contraction), plus the net diffusion flux of vorticity by viscous action. It is important to note that there

are no vorticity source terms in equation (4-1). This means that all the vorticity in the flow comes from the imposed initial, and/or solid wall boundary conditions.

Equation (4-1) can be further simplified to examine the vorticity realigned by the warping of the jet vortex sheet as the jet interacts with the crossflow. For this case, viscous diffusion can be neglected since the effect of diffusion would be very small in the near field, compared to the vorticity realigned by the stretching and turning of the vortex sheet due to the crossflow momentum. The governing equation then becomes

$$\frac{D\vec{\omega}}{Dt} = (\vec{\omega} \bullet \vec{\nabla}) u. \tag{4-2}$$

The three component vorticity transport equations are as follows:

x-component: $$\frac{D\omega_x}{Dt} = \omega_x \frac{\partial u}{\partial x} + \omega_y \frac{\partial u}{\partial y} + \omega_z \frac{\partial u}{\partial z}, \tag{4-3a}$$

y-component: $$\frac{D\omega_y}{Dt} = \omega_x \frac{\partial v}{\partial x} + \omega_y \frac{\partial v}{\partial y} + \omega_z \frac{\partial v}{\partial z}, \tag{4-3b}$$

z-component: $$\frac{D\omega_z}{Dt} = \omega_x \frac{\partial w}{\partial x} + \omega_y \frac{\partial w}{\partial y} + \omega_z \frac{\partial w}{\partial z}. \tag{4-3c}$$

4.2 Model Problem (1): Warping of Leading Edge Jet Vortex Sheet

To render the leading-edge warping problem tractable, we pose and solve a time-dependent equivalent. The vortex sheet, which initially corresponds to the one at the leading edge of a free jet, is suddenly subjected to the crossflow. The jet then begins to be deflected and its interface warped by the influx of the crossflow momentum.

Before the crossflow is turned on, an infinite vortex sheet lies in the y-z plane. At $x = 0$, the jet exits the hole vertically with a velocity $w = w_0$. The induced velocity due to the vortex sheet is ignored: therefore for $x < 0$, $w = 0$. The only component of vorticity is the one aligned with the y-axis, ω_y, having a strength η_0.

a) At $t < 0$, $\omega_y = -\eta_0$,

$$\omega_x = \omega_z = 0,$$

$$w = \begin{cases} w_0 & x > 0, \\ 0 & x < 0, \end{cases}$$

$$u = v = 0.$$
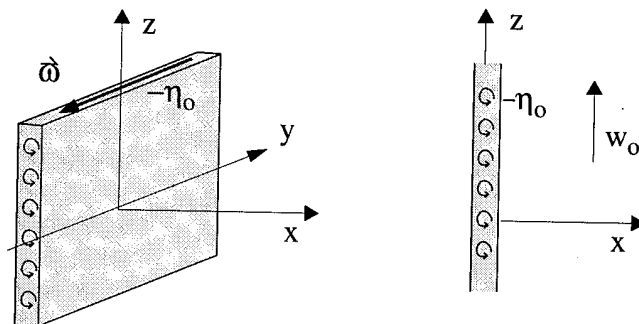
At $t = 0^+$, the crossflow is turned on. We assume complete entrainment of the cross-flow into the jet at the interface; the horizontal velocity is independent of x. We further assume that both horizontal and vertical velocities vary only with y; the transverse velocity remains zero. Vorticity then remains constant along the z-direction.

b) At $t = 0^+$,

$$u = u(y),$$

$$w = w(y),$$

$$v = 0,$$

$$\frac{\partial}{\partial z}\vec{\omega} = 0.$$

$u = u(y)$

$w = w(y)$
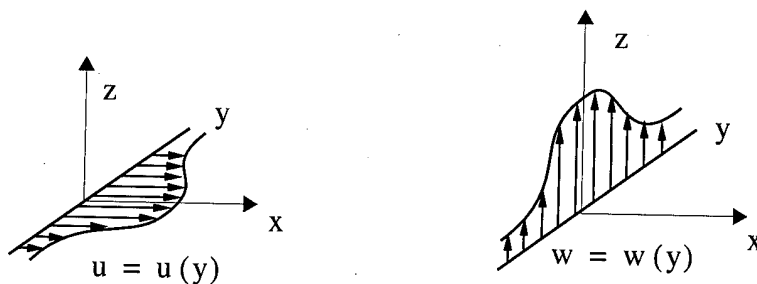
Under the above assumptions, the three vorticity transport component equations are reduced to the following:

x-component:
$$\frac{\partial \omega_x}{\partial t} + u\,(y)\frac{\partial \omega_x}{\partial x} = -\eta_0\frac{du}{dy}, \qquad (4\text{-}4a)$$

y-component:
$$\frac{\partial \omega_y}{\partial t} = 0, \qquad (4\text{-}4b)$$

z-component:
$$\frac{\partial \omega_z}{\partial t} + u\,(y)\frac{\partial \omega_z}{\partial x} = -\eta_0\frac{dw}{dy}. \qquad (4\text{-}4c)$$

(According to the present formulation, vorticity arising from the variation of u and w, and present outside of the vortex sheet, is simply convected downstream, without interacting with the vorticity contained within the vortex sheet. Thus, the vorticity outside can be decoupled from the vorticity within the vortex sheet and dropped from the left side of equations (4-4a) through (4-4c). Therefore, the quantities ω_x, ω_y, and ω_z refer only to the vorticity embedded in the vortex sheet; the vorticity, originally outside the vortex sheet, vanishes.)

Equations (4-4a) and (4-4c) can be solved by taking the Laplace transform in t.

$$\tilde{\omega}_x \equiv \int_0^\infty \omega_x e^{-st}dt \qquad (4\text{-}5)$$

Taking the Laplace transform of equation (4-4a) results in the following ordinary differential equation in x.

$$s\tilde{\omega}_x + u\,(y)\frac{d\tilde{\omega}_x}{dx} = -\eta_0\frac{1}{s}\frac{du}{dy} \qquad (4\text{-}6)$$

Setting the right side of equation (4-6) to zero and solving the homogeneous equation,

$$\frac{d\tilde{\omega}_x}{dx} + \frac{s}{u\,(y)}\tilde{\omega}_x = 0, \qquad (4\text{-}7)$$

gives the following result:

$$\tilde{\omega}_x = C\exp\left(-\frac{s}{u\,(y)}x\right). \qquad (4\text{-}8)$$

From the constraint that $\tilde{\omega}_x$ must vanish outside of the vortex sheet, the constant C must be equal to zero. Therefore, the only non-trivial solution of equation (4-6) must come from the inhomogeneous solution:

$$\tilde{\omega}_x = -\eta_0 \frac{du}{dy} \frac{1}{s^2}.$$ (4-9)

Taking the inverse Laplace transform of equation (4-9), and performing similar operations on equation (4-4c) then gives the following results:

$$\omega_x = -\eta_0 t \frac{du}{dy},$$ (4-10a)

$$\omega_y = -\eta_0,$$ (4-10b)

$$\omega_z = -\eta_0 t \frac{dw}{dy}.$$ (4-10c)

Equations (4-10a) and (4-10c) show that a streamwise component of vorticity, ω_x, is induced on the vortex sheet by the lateral variation in the streamwise velocity, u. Likewise, a vertical component of vorticity, ω_z, is induced by a variation in the vertical velocity, w. And the lateral component, ω_y, remains unchanged. The magnitude of the vorticity is thereby increased by the stretching of the vortex sheet:

$$|\vec{\omega}| = \eta_0 \sqrt{1 + \left(t\frac{du}{dy}\right)^2 + \left(t\frac{dw}{dy}\right)^2}.$$ (4-11)

As an example of the above results, if u(y) distribution is such that for y>0, $\frac{du}{dy} < 0$, as shown below,
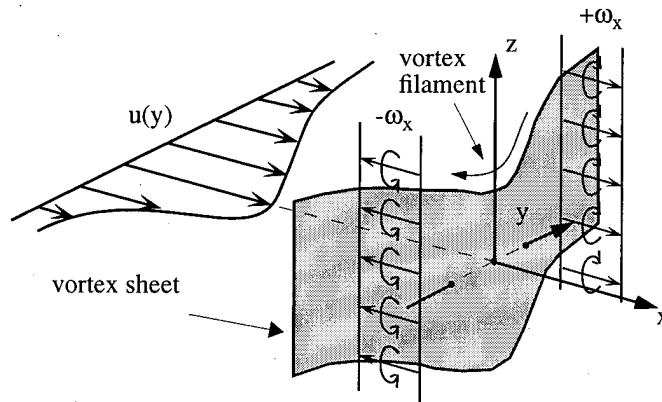
then the warping yields positive ω_x for y>0 and negative ω_x for y<0. This corresponds to the 'negative' pair sketched in figure 4-2.

On the other hand, if u(y) is such as shown below, the warping yields a 'positive' pair.
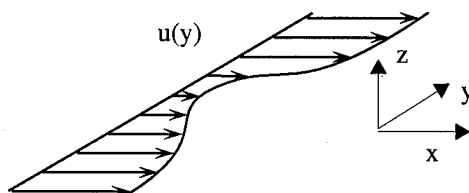
In applying the above time-dependent results for the present steady problem, time, t, may be replaced with the distance from the hole, z.

When we consider a single vortex filament lying on the warped vortex sheet as its representative, the appearance of the 'negative' pair as detected by laser sheets is schematically shown below in figure 4-3. Here the vortex filament is drawn to be lifted upwards by w(y) as well as pushed downstream at its center by u(y). This will induce a negative pair, which appears as $(-\omega_x, \omega_x)$ on the laser sheet normal to the x-axis and $(-\omega_z, \omega_z)$ normal to the z-axis. We shall make reference to this later.
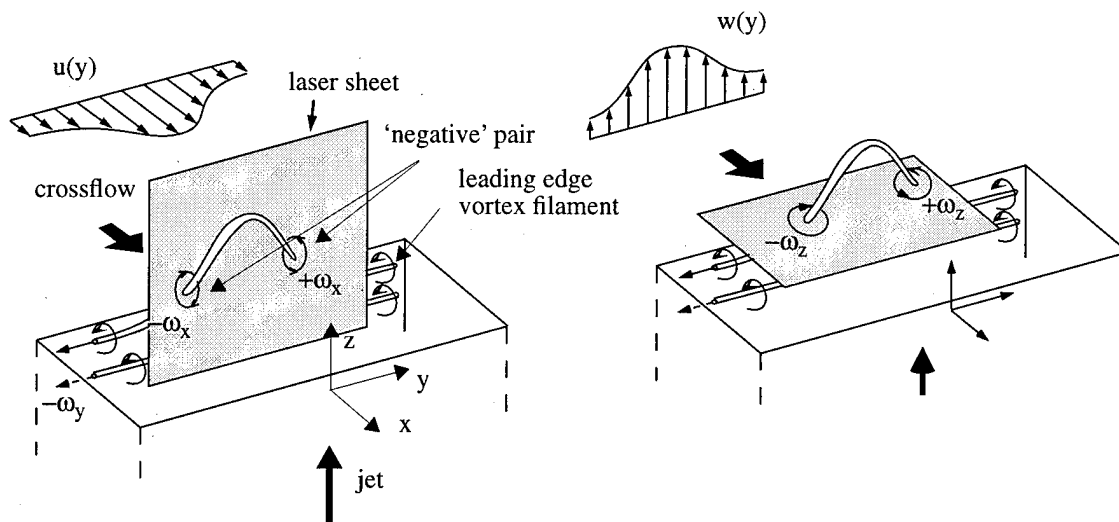
Figure 4-3: Deformation of Leading Edge Vortex Filament to Generate a 'Negative' Pair

4.3 Model Problem (2): Tilting of Side-Wall Vortex Sheet

A similar analysis to that previous given can be used to look at the formation of a z-component of vorticity due to the tilting of the jet side-wall vortex sheet under the influence of a crossflow. The effect of the crossflow on the jet is like a partial cover placed near the leading edge (Andreopoulis and Rodi (1984)). As a result, the jet starts to deflect downstream even within the hole passage, resulting in the streamwise variation in the jet velocity. Again as a time-dependent equivalent to this, we assume that w, which is initially uniform, suddenly starts to vary in the x-direction. For this case, the strength of the vortex sheet originally aligned in the x-direction is assumed constant and is given as $\omega_x = \xi_0$.
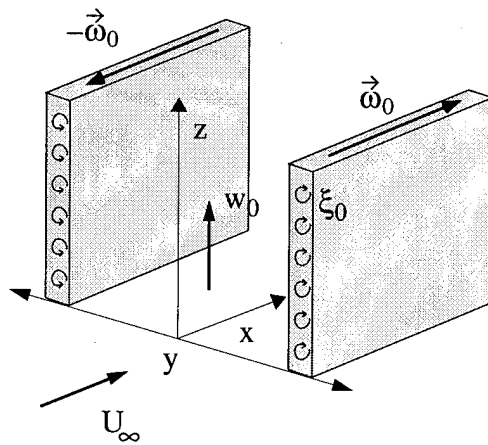
At $t = 0^-$
$u = U_\infty$: crossflow velocity
$v = 0$
$w = w_0$: jet velocity

$\omega_x = \xi_0$
$\omega_y = 0$
$\omega_z = 0$

At $t = 0^+$
$u = U_\infty$
$v = 0$
$w = w(x)$

It is also convenient to consider the case where $\dfrac{dw}{dx}$ is a constant.

For the given conditions, the only relevant component of the vorticity transport equation is that in ω_z (equation (4-3c)), which reduces to

$$\frac{\partial \omega_z}{\partial t} + U_\infty \frac{\partial \omega_z}{\partial x} = \xi_0 \frac{dw}{dx}. \tag{4-12}$$

Taking the Laplace transform in t, then solving the ordinary differential equation, gives the following complete solution:

$$\tilde{\omega}_z = C\exp\left(-\frac{sx}{U_\infty}\right) + \xi_0 \frac{1}{s^2} \frac{dw}{dx}. \tag{4-13}$$

Inverting, we obtain

$$\omega_z = C\delta\left(t - \frac{x}{U_\infty}\right) + \xi_0 t\frac{dw}{dx} \quad . \tag{4-14}$$

The first term in (4-14) is irrelevant; therefore, C must be zero.

$$\omega_z = \xi_0 t\frac{dw}{dx} \tag{4-15}$$

The equation states that any change in the vertical velocity profile in the x-direction will generate a vertical component of vorticity, ω_z. And, as in the case of the warping of the leading edge vortex sheet, the magnitude of the vorticity will also increase by the stretching of the vortex sheet.

$$|\vec{\omega}| = \xi_0 \sqrt{1 + \left(t\frac{dw}{dx}\right)^2} \tag{4-16}$$

For the present steady case, the induction of ω_z, caused by the above vortex is schematically shown below.
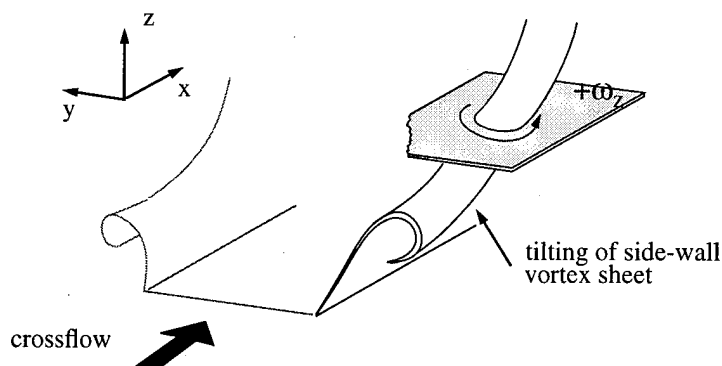
We shall return to equations (4-10a), (4-10c) and (4-16) in §6, where they will be found to provide interpretive assistance to the results of the flow visualization and PIV.

Chapter 5: Basic Vortical Features

In the foregoing chapter, the normally discrete vortices of the rolled up shear layer are smeared into a vortex sheet so that one can analyze the broad effect caused by its gross deformation. Here, in this chapter, we regard the discrete vortical structures as such and discuss their individual, localized behavior. These vortical structures are commonly found in all the shaped holes of §3 and will be discussed again in more detail in §6. Although certain vortices present themselves more conspicuously than the others, they all comprise important components of the entire flow structure. For convenience, here we collectively discuss them.

5.1 Lateral Spillage and Roll-Up

As illustrated in figure 5-1 for a y-z cross-section, as the jet leaves the hole, the crossflow above the jet forces the jet fluid to turn laterally outward 90°, spilling over the edges of the hole and rolling up. The spillage and roll-up of the side wall vorticity forms the 'steady' kidney-vortices briefly mentioned in §3.1. The vector plot on the right in figure 5-1, obtained by PIV for the round hole at a blowing ratio of 0.8, shows the outward motion of the jet fluid as it leaves the hole. In addition to the lateral spillage, the crossflow also forces the jet fluid near the leading edge to turn again toward the streamwise direction. This lateral spillage and turning toward the streamwise direction can be seen in figure 5-2, flow visualization and PIV results, for the round hole at a blowing ratio of 0.8.

The local acceleration associated with both the spillage and turning of the jet fluid is believed to be the explanation for the results of Vogler (1963), Fearn and Weston (1975)
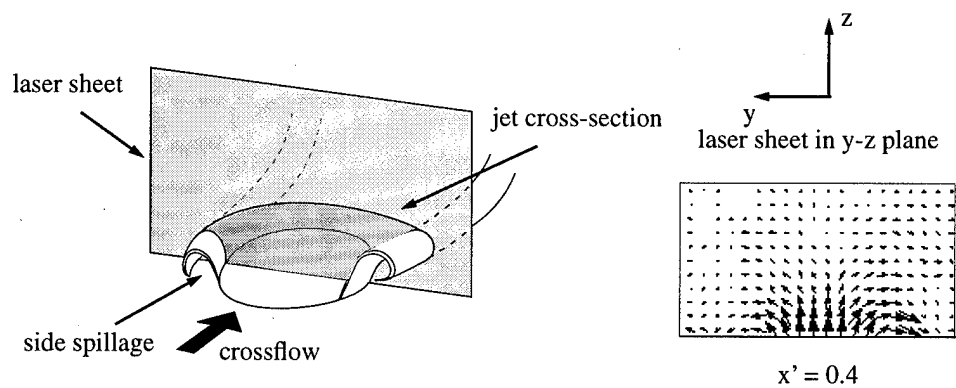
Figure 5-1: 'Steady' Kidney-Vortices due to Side-Wall Spillage
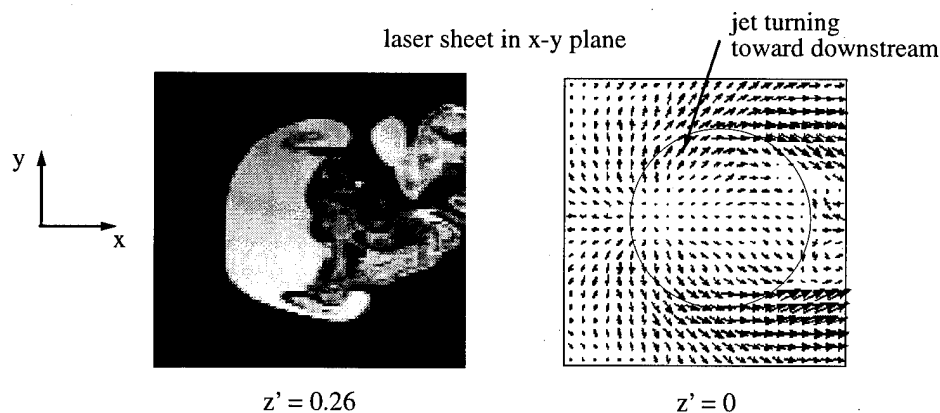
Figure 5-2: Evidence of Jet Lateral and Streamwise Spillage, BR = 0.8

and Sugiyama's (1995) which all show the static pressure around the sides of a jet to be lower than that for a two-dimensional cylinder in the same crossflow. They used an array of circumferentially spaced static pressure holes at different radial distances to obtain the pressure coefficient around a circular hole. Sugiyama's results, for instance, show that for a jet injected perpendicular to the crossflow at a blowing ratio of 0.98, the pressure coefficient at the lowest point, which is located at the sides of the hole, was around -2.5; this is lower by a factor of two compared to the lowest value for the cylinder of -1.2. By increasing the blowing ratio to 1.96, the lowest pressure coefficient at the same point is decreased to a value of -4.4.

5.2 Vorticity in the Vicinity of the Jet Leading Edge

The adverse pressure gradient created upstream of the hole, due to the presence of jet, causes the crossflow boundary layer to roll up into a horseshoe vortex. This structure entraps the plate boundary layer vorticity and diverts it around the hole. For the most part, the vorticity within the horseshoe vortex remains separated from the jet vorticity until it is past the hole. Once past the hole, the low pressure region behind the jet draws this passing crossflow boundary layer fluid into the bottom side of the jet.

The behavior of the horseshoe vortex is seen in figure 5-3. Here a trace of red dye is injected just upstream of the round hole to track the horseshoe vortex. The red dye is seen accumulating in front of the hole for both blowing ratios 0.8 and 2.0. A streak of red dye then flows along the side of the hole, near the plate, until it reaches the trailing edge where the dye is lifted off the plate and drawn into the underside of the jet. The entry of the cross-flow boundary layer vorticity into the jet wake region will be discussed in§5.4.
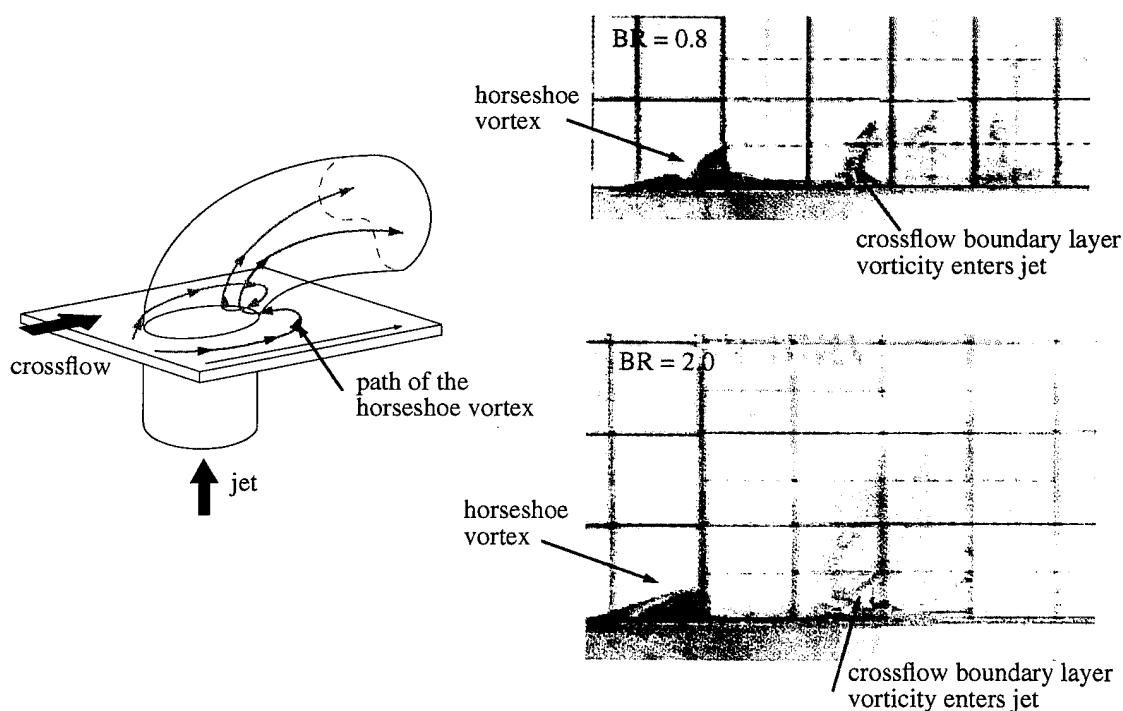
Figure 5-3: Interaction Between Jet and Horseshoe Vortex

Although the horseshoe vortex does not appear to penetrate the jet at the leading edge, its presence can be felt well within the jet passage. The induced velocity of the horseshoe acts to suppress the jet flow inside the hole leading edge. The jet leading edge boundary layer senses this blockage while still in the hole passage. The adverse pressure gradient thus imposed on the jet leading edge boundary layer causes it to roll up and separate from the passage wall. This jet separation mirrors the crossflow separation as a horseshoe vortex and was observed earlier by Andreopoulos (1982) for a round hole.

The rolling up and separation of the jet boundary layer along the leading edge side of the hole is seen in the flow visualization results for the large rectangular hole, hole 1a (figure 5-4). The image was taken using a mirror placed below the plate at an angle to allow the camera to see inside the hole. The viewing angle is 30° relative to the y-axis. Although
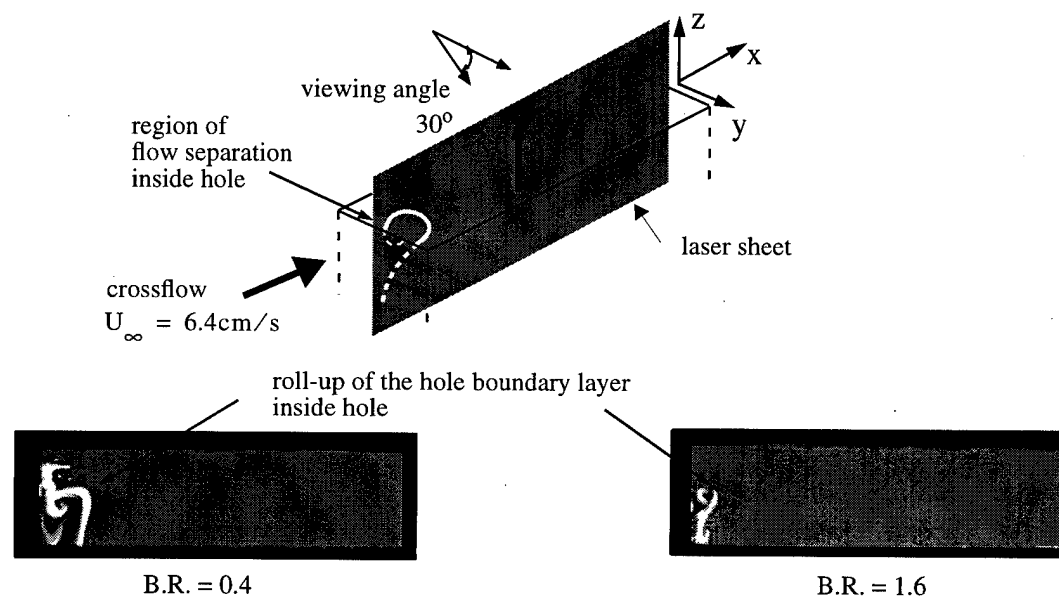
Figure 5-4: Flow Separation at the Hole Leading Edge

the roll-up of the boundary layer inside the hole occurs at both the low and high blowing ratios, the separation inside the hole appears more pronounced for the blowing ratio of 0.4. As illustrated in figure 5-5, the competition between the jet leading edge and the crossflow boundary layer determines the location of separation and roll-up within the jet. As the blowing ratio is increased, the position of the jet boundary layer roll-up and separation

moves toward the hole exit, as obvious from the fact that for the limiting case of a free jet, $BR \rightarrow \infty$, roll-up takes place completely outside the jet, with no separation of the jet fluid.
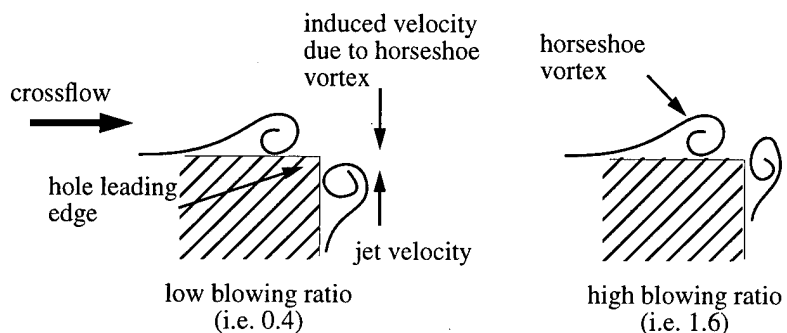
Figure 5-5: Competition between the Horseshoe Vortex and Jet Leading Edge Vortex

After the jet boundary layer vorticity rolls up, it is periodically shed into the cross-flow. The picture on the left of figure 5-6 shows the roll-up of jet vorticity inside the hole. In this same picture, the previously shed vortex has a trace of fluorescent dye at its center. At another instant, the leading-edge shed vortex is seen just outside of the jet. This same behavior regarding the oscillatory roll-up and convection of the hole leading edge shear layer was also reported recently by Kelso, Lim, and Perry (1996).
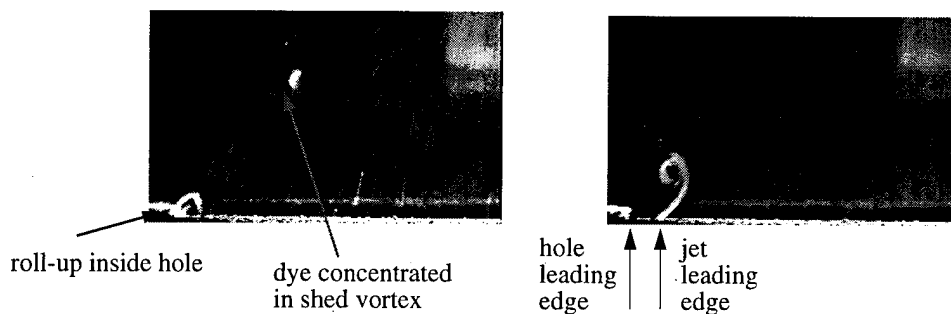
Figure 5-6: Roll-up and Shedding of Hole 1a Leading Edge Vorticity, BR = 1.6

5.3 Spillage of Leading Edge Vorticity and Realignment

As just mentioned, when the leading edge boundary layer finally leaves the hole, part of the boundary layer periodically rolls up and starts to ride on top of the jet. In y-z cross-sections such as figures 3-4 and 3-5, these vortical structures appear intermittently as 'unsteady' vortices located above the 'steady' vortices discussed in §5.1. The realignment of the leading edge boundary layer, the vorticity of which is initially aligned along the y-direction (ω_y), toward the x-direction (ω_x) observable in these pictures is caused by the warping of the jet frontal interface discussed in §4. Dep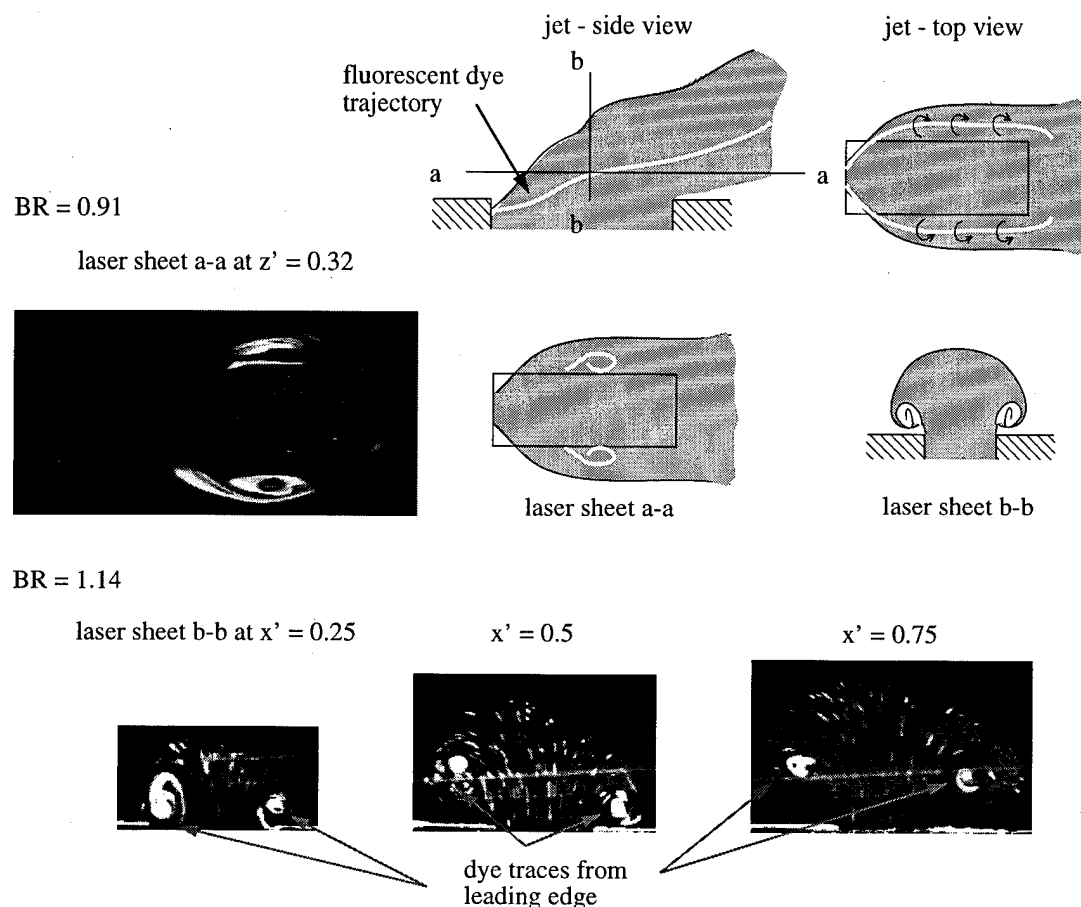ending on how the warping takes place, the 'unsteady' vortices appear either as 'positive' or 'negative' vortex pairs. This point will be pursued further in §6.

In addition to this periodic shedding related to the central portion of the leading edge boundary layer, the remainder near the side walls spills sideways and combines with the side-wall boundary layer. This behavior is seen in two different cross-sectional views of the jet for hole 1a in figure 5-7: views parallel to the plate, and perpendicular to the cross-flow. (In viewing the vortical structures shown in these and elsewhere, it is important to keep in mind that these images correspond only to the vorticity component projected on each plane of the laser sheet.) In both views, the leading edge of the jet was seeded with two traces fluorescein dye inside the hole, 2.1 cm from the exit. In the parallel view (a-a section), the dye is seen spilling outward as it exits the hole from the leading edge. Although the leading edge vorticity is initially aligned parallel to the a-a plane, it still appears here as out-of-plane vorticity due to its upward tilting. Perpendicular to the cross-flow (b-b section), the cross-section of the jet shows that the dye has been drawn to the center of the side-wall vortices indicating that the leading edge jet boundary is being turned in the direction of the crossflow and is combining with the side-wall boundary layer. Thus, even close to the hole leading edge, the kidney-vortices contain not only the side-wall vorticity, but also leading edge vorticity that has been turned by the influence of the crossflow.

Figure 5-7 is further evidence that the hole leading edge vorticity contributes to the side-wall kidney-vortex pair.

jet - side view   jet - top view

fluorescent dye trajectory

BR = 0.91

laser sheet a-a at z' = 0.32

laser sheet a-a   laser sheet b-b

BR = 1.14

laser sheet b-b at x' = 0.25   x' = 0.5   x' = 0.75

dye traces from leading edge

Figure 5-7: Combining of the Leading Edge and Side-wall Boundary Layers, Hole 1a

5.4 Wake Vortices

Large vortical structures have been observed on the downstream side of the jet. These wake vortices were shown by Fric (1994) to be comprised only of crossflow boundary layer fluid. These vortices are the only mechanism for introducing new vorticity into the jet once it leaves the hole. This new vorticity comes from the crossflow boundary layer and enters the bottom side of the jet. Although this new vorticity contributes to the downstream strength of the kidney-vortices, they do not change the very near field character of the jet. Since the focus of this research is on the jet characteristics in the immediate vicinity of the hole, the role of wake vortices will not be discussed in further detail.

Chapter 6: Flow Structure Details

The experimental results presented here combine flow visualization and quantitative velocity field measurements to investigate the effect of hole geometry on the very near field characteristics of the jet. The results for the six basic hole geometries described in §2.4 will be discussed here in detail. General features common to all hole geometries are the presence of a steady kidney-vortex pair due to the hole side-wall vorticity, plus an additional unsteady vortex pair riding over the top of the steady pair. The appearance of a 'negative' vortex pair, however, is geometry dependent and may be found not only at the leading edge, but also near the trailing edge of the hole. The appearance of a 'negative' pair at the trailing edge is believed to be the result of the warping of the trailing edge vortex sheet under the influence of the strong reverse flow immediately downstream of the jet.

The blowing ratios of interest are from 0.4 to 2.0. The jet velocity was determined by dividing the volume flow rate by the exit area of the hole. The crossflow velocity for holes 1 through 6, was set to 8 cm/s. For the larger holes, 1a through 6a, the crossflow velocity was set to 5.4 cm/s. The crossflow was held to a constant velocity; therefore, the blowing ratio was changed strictly by changing the jet velocity, or $BR \propto U_j$. The Reynolds number, based on jet cross stream dimension, D, and crossflow velocity, U_∞, ranged from 1,040 to 2,900.

For each hole geometry, Particle Image Velocimetry (PIV) measurements were made in the same three orthogonal planes depicted in figure 2-3. The vorticity field was then obtained by subtracting the cross-derivatives of the planar velocity components:

$$\omega_x = \left(\frac{\partial w}{\partial y} - \frac{\partial v}{\partial z} \right), \qquad (6\text{-}1a)$$

$$\omega_y = \left(\frac{\partial u}{\partial z} - \frac{\partial w}{\partial x} \right), \qquad (6\text{-}1b)$$

$$\omega_z = \left(\frac{\partial v}{\partial x} - \frac{\partial u}{\partial y} \right). \qquad (6\text{-}1c)$$

The general color coding for the PIV results is as follows: blue for negative values of vorticity and velocity, red for positive, and white for the values near zero. For each PIV plot, the magnitude of the measured velocity or vorticity at a given point is represented by the associated color at the corresponding point. As stated in §2, the vorticity is non-dimensionalized with respect to the jet velocity and a length scale selected as the diameter of the round hole, hole 3. The vertical and cross-stream velocities, w and v, respectively, are non-dimensionalized by the jet velocity. The streamwise velocity, u, is non-dimensionalized using the crossflow velocity. Laser Induced Fluorescence results complement the PIV data by displaying an overall picture of the flowfield.

The general presentation sequence for all hole results will be the following: 1) the steady kidney-vortices and 'negative' vortex pair appearing in the plane normal to the crossflow, or y-z plane, 2) the vorticity component, ω_z, appearing in the plane parallel to the plate, due to the tilting of the side-wall vortex sheet, 3) the unsteady vortices due to the warping of the hole's leading edge vorticity, and 4) the region of reverse flow immediately downstream of the hole due to the tilting of the hole's trailing edge vorticity.

6.1 Square Hole

The square hole is presented as the baseline configuration, since the lack of hole curvature separates the side-wall vorticity and that coming from the leading and trailing edges of the hole. The square also exhibits all the basic features as the other geometries with the exception of the 'negative' vortex pair (A single 'negative' pair is observed at the trailing edge of the hole only for the highest blowing ratio, 2.0. The reason for its appearance is discussed later in §6.4.4 where the 'negative' pair at the trailing edge is more prevalent.) The discernible sources of the jet vorticity, the essential lack of a 'negative' vortex pair, and an aspect ratio of unity, makes the square hole the cleanest configuration. Once its flowfield is

described, the additional features peculiar to the other holes will be presented as variations to the square hole.

6.1.1 'Steady' Kidney-Vortex Pair

Figure 6-1 compares flow visualization results with the vorticity data for three blowing ratios 0.8, 1.6, and 2.0. The laser sheet was oriented normal to the crossflow, in the y-z plane, at various positions along the x-axis. The flow visualization picture was taken at the downstream edge of the hole, whereas, the PIV processed images are presented for laser sheet positions equally spaced from the hole leading edge to the trailing edge. At each x-location, the vorticity profile was obtained using the average of four velocity field measurements.

The steady side-wall positive kidney-vortex pair can be seen in both the flow visualization pictures and vorticity profiles in figure 6-1. Since the non-dimensional vorticity is comparable for the three blowing ratios, the lift-off and strength of the kidney vortices must increase with jet velocity (This is consistent with the results of Fearn and Weston (1975), who found that, for a round hole, the initial strength of the vortex pair is directly proportional to the jet velocity). Near the leading edge, x' = 0, 0.09 and 0.18, a weak vortex pair is observed outboard of the hole. This pair is believed to be the crossflow boundary layer vorticity being rolled up into the horseshoe vortex and diverted around the hole. For the higher blowing ratios, 1.6 and 2.0, the flow visualization pictures show a stacking of the steady and unsteady kidney-vortices at the trailing edge of the hole. The distinction between the two vortex pairs can be seen also in the PIV vorticity plots, although the averaging of the files reduces the ability to capture accurately the unsteady behavior. As mentioned, the vortical structures appearing in the plane of the laser sheet represent only the x-component of vorticity, ω_x; there may be other components of equal or greater magnitude hidden from view.

The cross-stream and vertical velocity plots, v' and w', corresponding to the vorticity profiles of figure 6-1, are shown in figures 6-2 and 6-3, respectively. The v'-velocity plots show the side spillage of the jet along the front half of the hole. However, as the jet exits
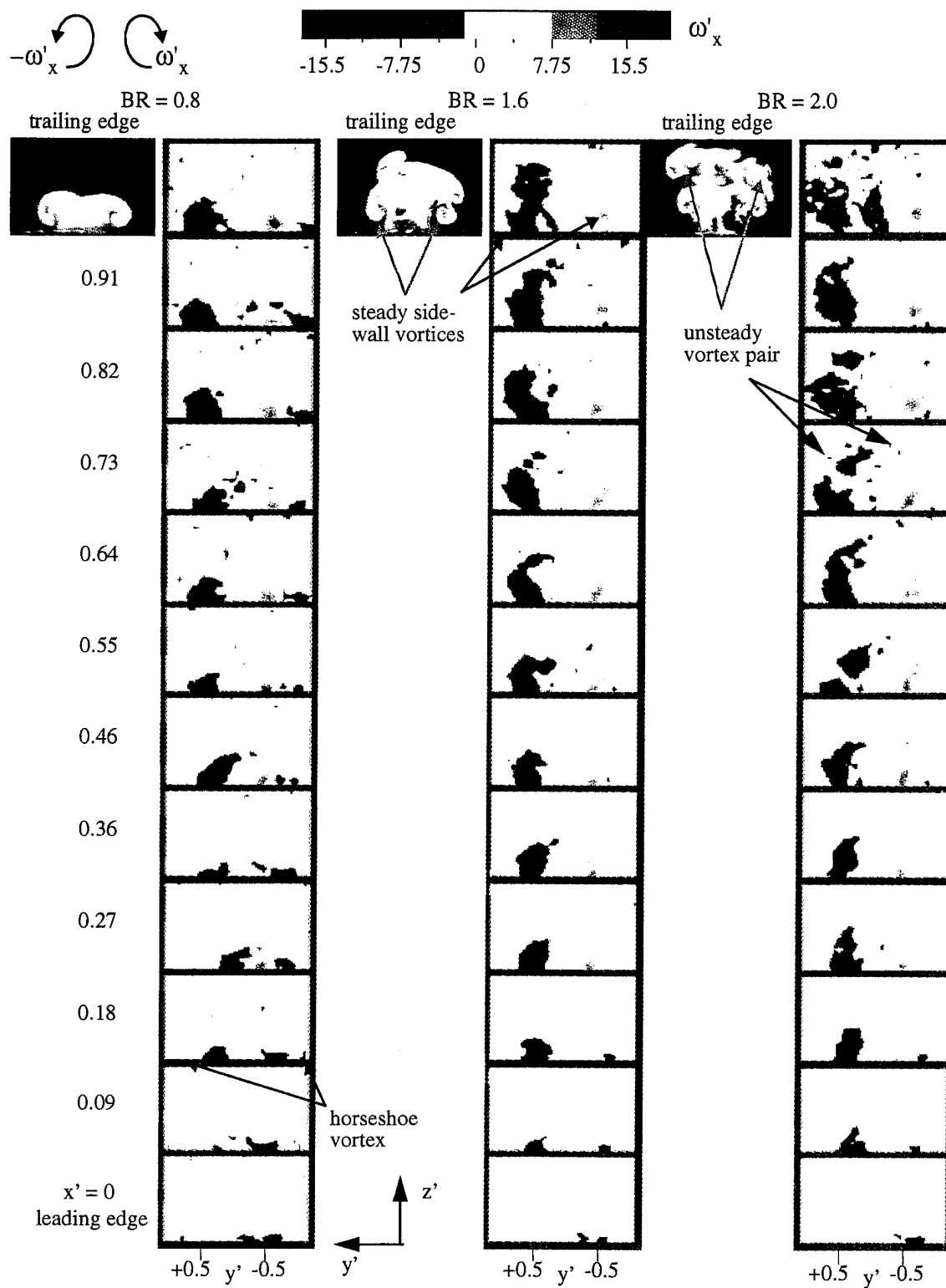
Figure 6-1: Hole 4: Flow Visualization and PIV Vorticity Plots, BR = 0.8, 1.6, and 2.0

the hole nearer the trailing edge, the steady kidney-vortices are lifted off the plate, resulting in an induced velocity at the bottom of the vortices laterally and toward the centerline.

For all three blowing ratios, the vertical velocity, w', at the leading edge of the hole is in the negative z-direction (blue areas). This is the result of the induced downward velocities of both the horseshoe vortex and the jet leading edge vortex sheet at the hole exit. As the jet velocity decreases, the negative velocity induced by the horseshoe vortex overwhelms the jet near the leading edge, and increases the region of negative velocity. Downstream of the leading edge, the negative vertical velocity on the sides, which surrounds the positive one at the center, is induced by the side-wall positive kidney-pair.

6.1.2 Vorticity Realignment by Tilting of Side-Wall Vortex Sheet

The interaction of the jet with the crossflow alters the jet velocity profile at the hole exit. The effect of the crossflow on the jet is described by Andreopoulos and Rodi (1984) as the equivalent of placing a partial inclined cover over the front part of the jet exit. The 'partial cover' skews the velocity profile inside the hole, lowering the velocity at the leading edge and increasing it toward the trailing edge. This skewing of the velocity profile at the hole centerline and along the side-walls is shown in figure 6-4. The skewness is more pronounced at lower BR and, as BR increases, the centerline velocity profile tends to become more uniform, as expected.

The saddle-shaped velocity distribution at the edge of the hole, which becomes more distinct at higher BR, appears to be caused by the following corner effect: at the corners of the hole, the induction by the vorticity from the leading-edge or trailing-edge boundary layer adds to the vertical component of the velocity, whereas at the center of the hole, $x' = 0.5$, the leading and trailing edge boundary layers are too far separated to have an additive effect. (If this explanation is valid, the saddle distribution should depend on the aspect ratio of the hole. For high aspect ratio holes, the decreased separation of the leading and trailing edge boundary layers will eliminate the depression near the center of the hole, resulting in a profile that closely matches that taken along the centerline of the hole. This will be found to be indeed the case in §6.2)
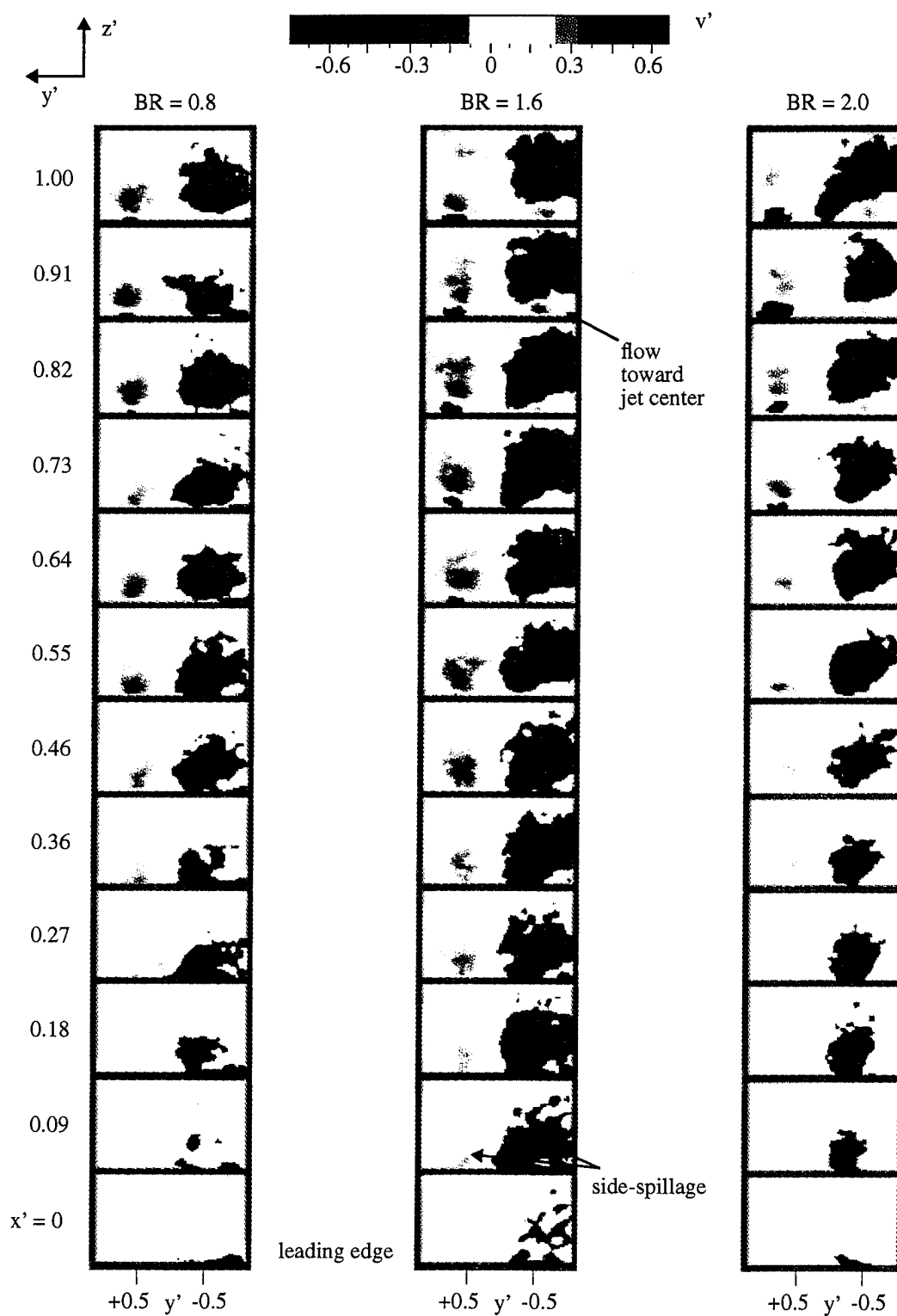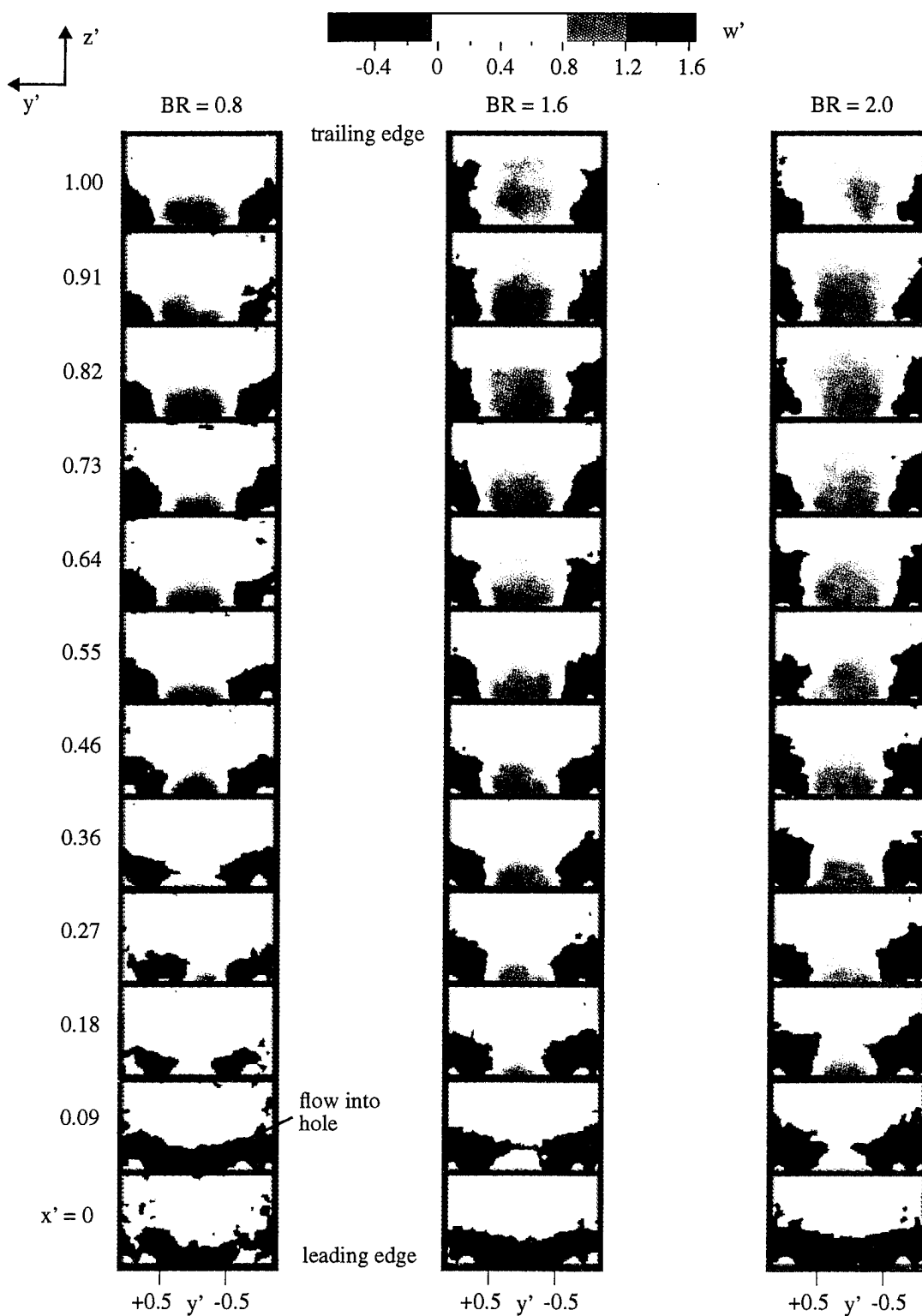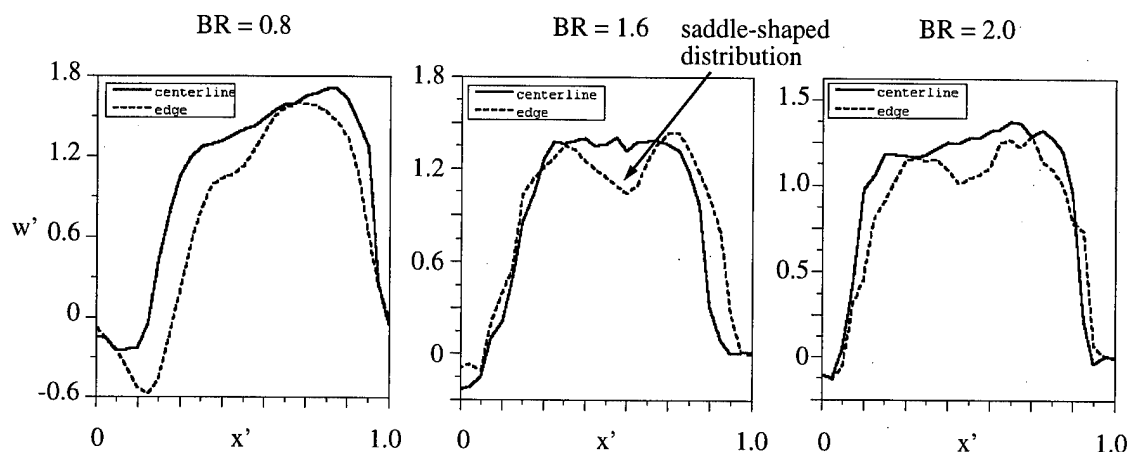
**Figure 6-2:** Hole 4: v'-Velocity Plots, BR = 0.8, 1.6, 2.0

**Figure 6-3:** Hole 4: w'-Velocity Plots, BR = 0.8, 1.6, and 2.0

Figure 6-4: Hole 4: Side Wall Velocity Profiles for BR = 0.8, 1.6, 2.0

Aside from the saddle-distribution, the general skewness in the vertical velocity with x' along the side of the hole indicates that the aforementioned steady kidney-vortices near the trailing edge of the hole will be lifted up compared to the vortices nearer to the leading edge. This velocity gradient, as discussed in §4.3, causes the tilting of the side-wall vortex sheet, as illustrated in figure 6-5, generating a component of vorticity in the z-direction, ω'_z, just above the hole exit. Figure 6-6 shows the vorticity field in the plane parallel to, and just above, the surface. The jet side-wall vorticity is clearly seen along the length of the hole. (The vorticities, which are located outboard and with signs opposite to the ones of the side-wall vorticity, correspond to that of the crossflow boundary layer entrained upwards by the jet.) The appearance of ω'_z even at the exit plane implies that such vortex
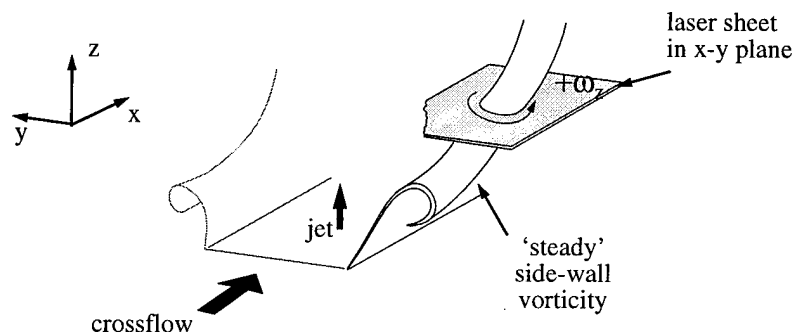
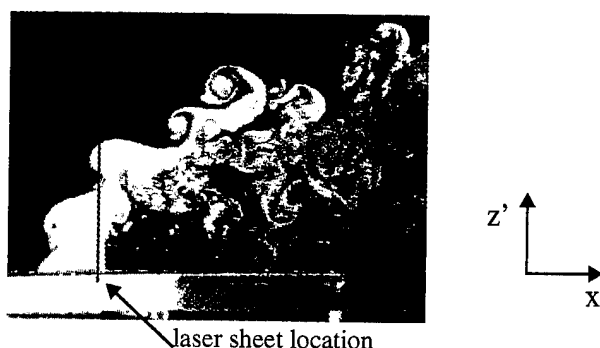**Figure 6-5:** z-Vorticity due to Tilting of Side-Wall Vortex Sheet
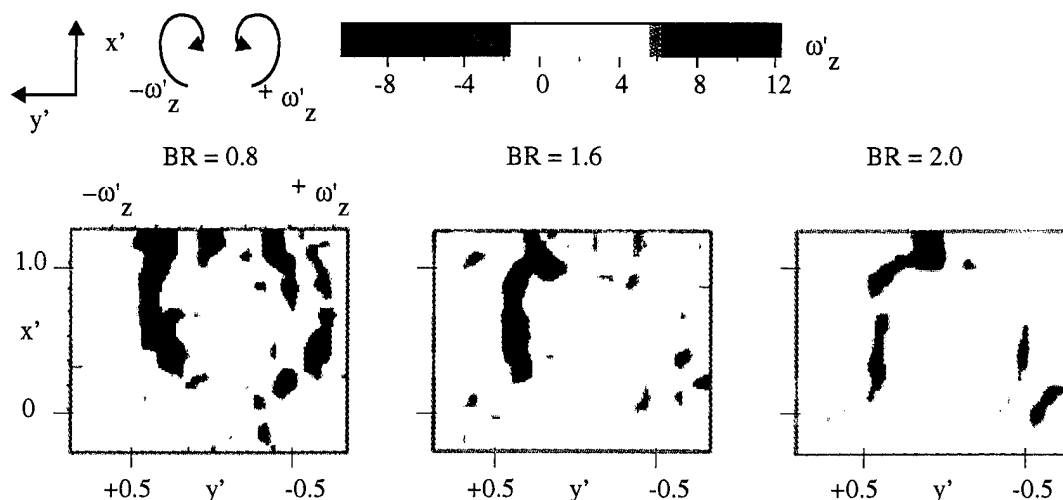
Figure 6-6:   z-Vorticity at z' = 0 due to Tilting of Side-Wall Vortex Sheet

tilting already starts well inside the hole. At lower BR, ω'_z becomes more intense towards the trailing edge; this is in agreement with the velocity profile. This tilted side-wall vorticity, after convecting downstream, will realign itself in the streamwise direction, eventually becoming part of the kidney-pair.

6.1.3 Vorticity Realignment by Warping of Leading Edge Vortex Sheet

As shown in §5.3, the leading edge boundary layer is stretched and turned by the cross-flow. In addition to the migration of leading edge boundary layer fluid toward the outside of the jet, the central portion of the leading edge boundary layer rolls up and passes intermittently over the top. The view of the jet trajectory, in figure 6-7, shows the roll up of the vorticity at the leading edge. As this vorticity passes through a laser sheet oriented in the y-z plane, it shows up as an intermittent vortex pair riding on top of the steady kidney-vortices as shown in the time-accurate vorticity plots in figure 6-7 (The corresponding time-averaged plot can be found in figure 6-1). A similar flow visualization result, presented by Ajersch *et al.* (1995), shows the movement of this 'unsteady' vortex pair over five consecutive flow visualization video images. However, their interpretation of these vortex structures differs from ours.

jet trajectory, BR = 1.6

z'

x'

laser sheet location

instantaneous cross-sections for
laser sheet in y-z plane, BR = 1.6

$-\omega'_x$ ω'_x

-30 -20 -10 0 10 20 30 ω'_x

'unsteady'
vortices

z'

y'   t = 0 ms   'steady'   t = 66 ms   t = 132 ms   t = 198 ms
vortices
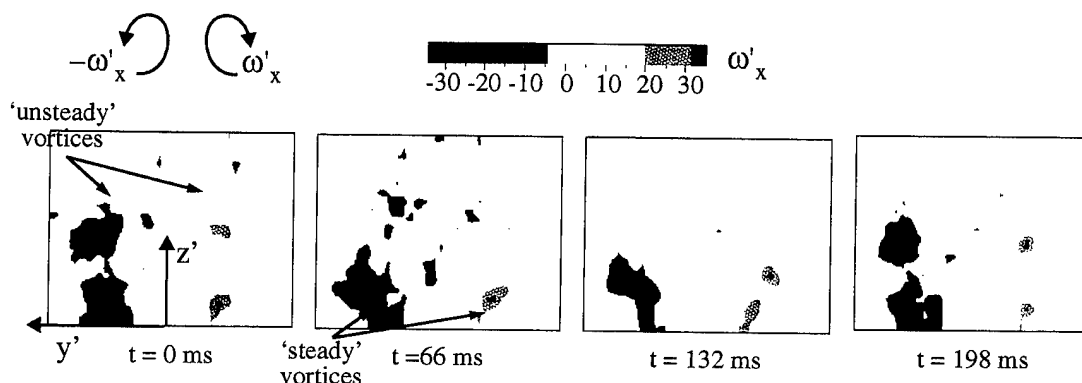
Figure 6-7:   Jet Trajectory and Cross-section Time-accurate Plots of Vorticity at x' = 0.82

As discussed in §4.1, the way in which the jet-crossflow interface at the leading edge is warped determines the sign of the vorticity as it passes through the laser sheet. The streamwise velocity profiles, u', in the plane parallel to the plate at z' = 0.32, are shown in figure 6-8. The lateral variation in u, $\frac{du}{dy}$, indicates that the leading edge vortex sheet is being warped to induce the unsteady vortex pair having the same sign as the kidney-vortex pair, as illustrated in figure 6-9.

Regardless of whether the leading edge vortices appear as unsteady vortices near the centerline, or they migrate toward the sides of the jet, all eventually coalesce with the side-wall vorticity as the kidney-pair sufficiently downstream.
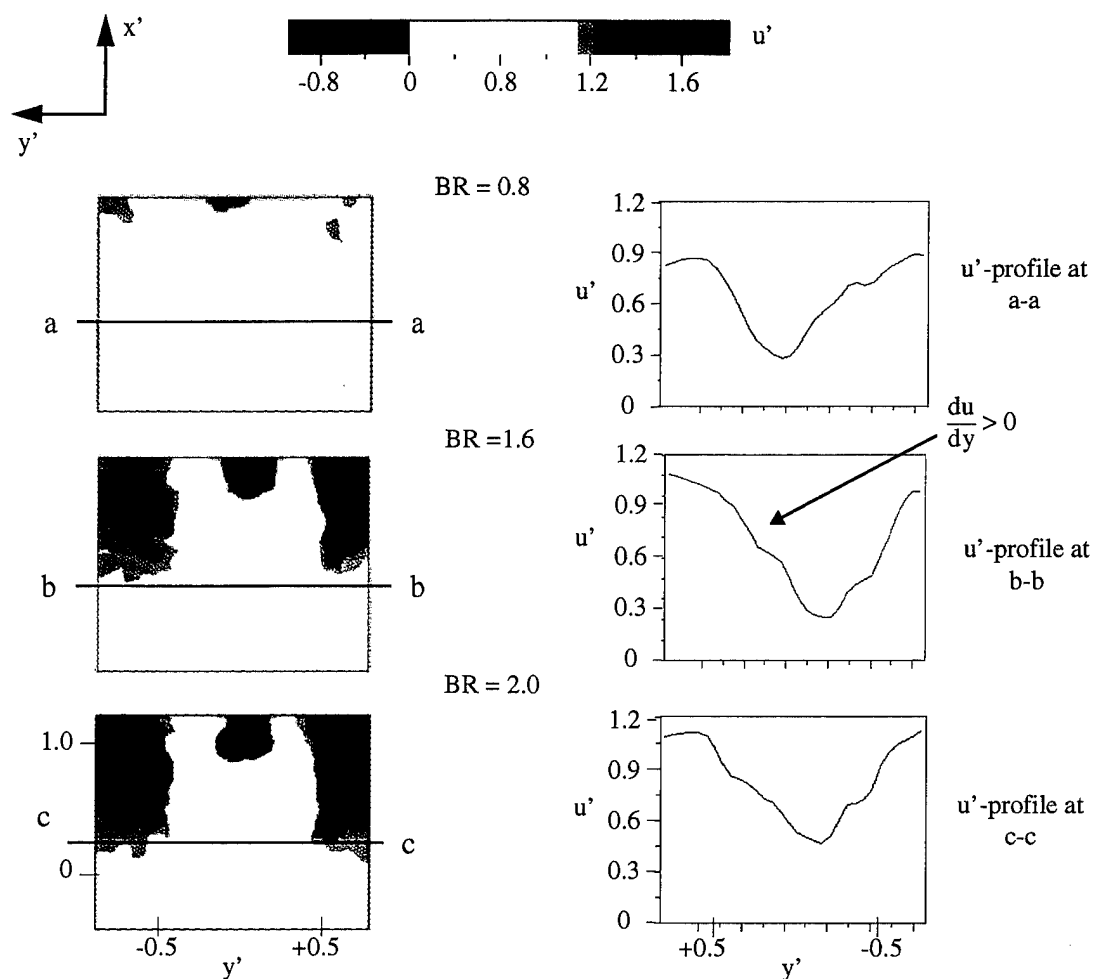
Figure 6-8: u'-Velocity at z' = 0.32, BR = 0.8, 1.6, 2.0

6.1.4 Tilting of Hole Trailing Edge Vorticity

As shown previously in figure 5-3, on the downstream side of the jet there exists an area of reverse flow that penetrates into the jet. The extent of the reverse flow region on the under-side of the jet was investigated by positioning the laser sheet parallel to the plate at eight different z-locations (figure 6-10). At low blowing ratios, the jet is bent such that the higher laser sheets cut across the top part of the jet where there is no reverse flow.
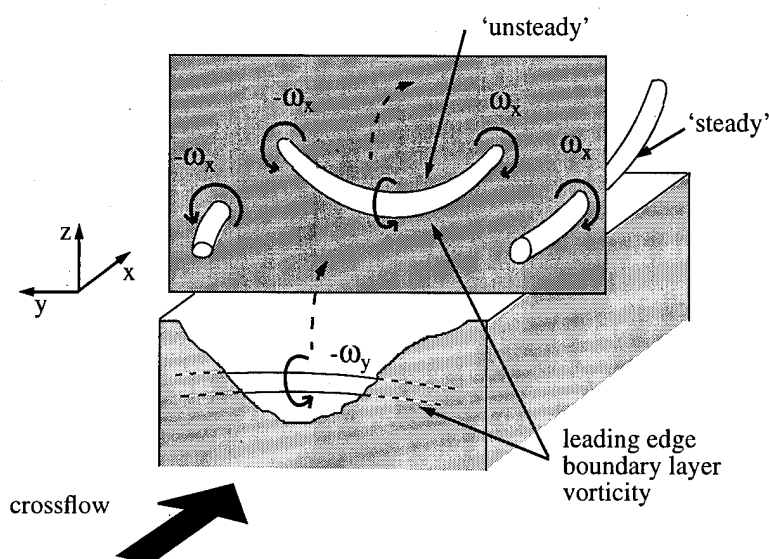
Figure 6-9: Streamwise Vorticity due to Warping of the Leading Edge Boundary Layer
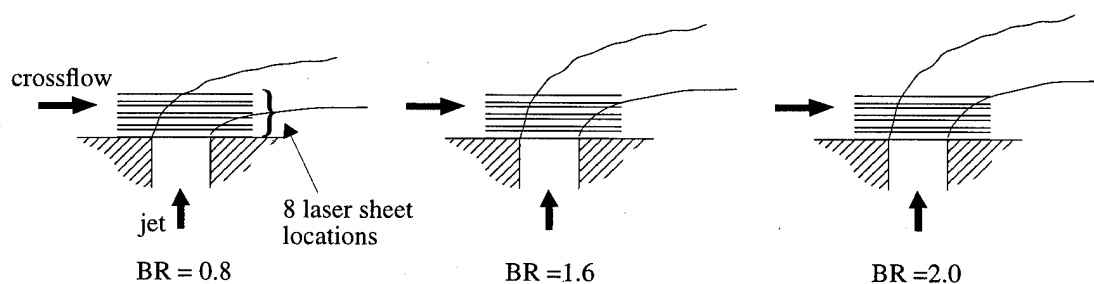
Figure 6-10: Laser Sheet Position for Parallel Velocity Profiles

Figure 6-11 shows the streamwise velocity along planes corresponding to figure 6-10. The area of reverse flow at the hole trailing edge is formed on the underside of the jet and extends well off the plate, its vertical extent increasing with blowing ratio. For the lowest blowing ratio, 0.8, the reverse flow region extends only to $z' = 0.40$ because the jet is bent such that the laser sheet slices through the top part of the jet.

The two reasons for this reverse flow region are illustrated in figure 6-12. First, the bending of the jet creates a low pressure region to balance the centrifugal forces acting on the jet (to be precise, the momentum balance at the jet/crossflow interface must also be considered). Second, the upward tilting of the trailing edge vortex sheet near the center of
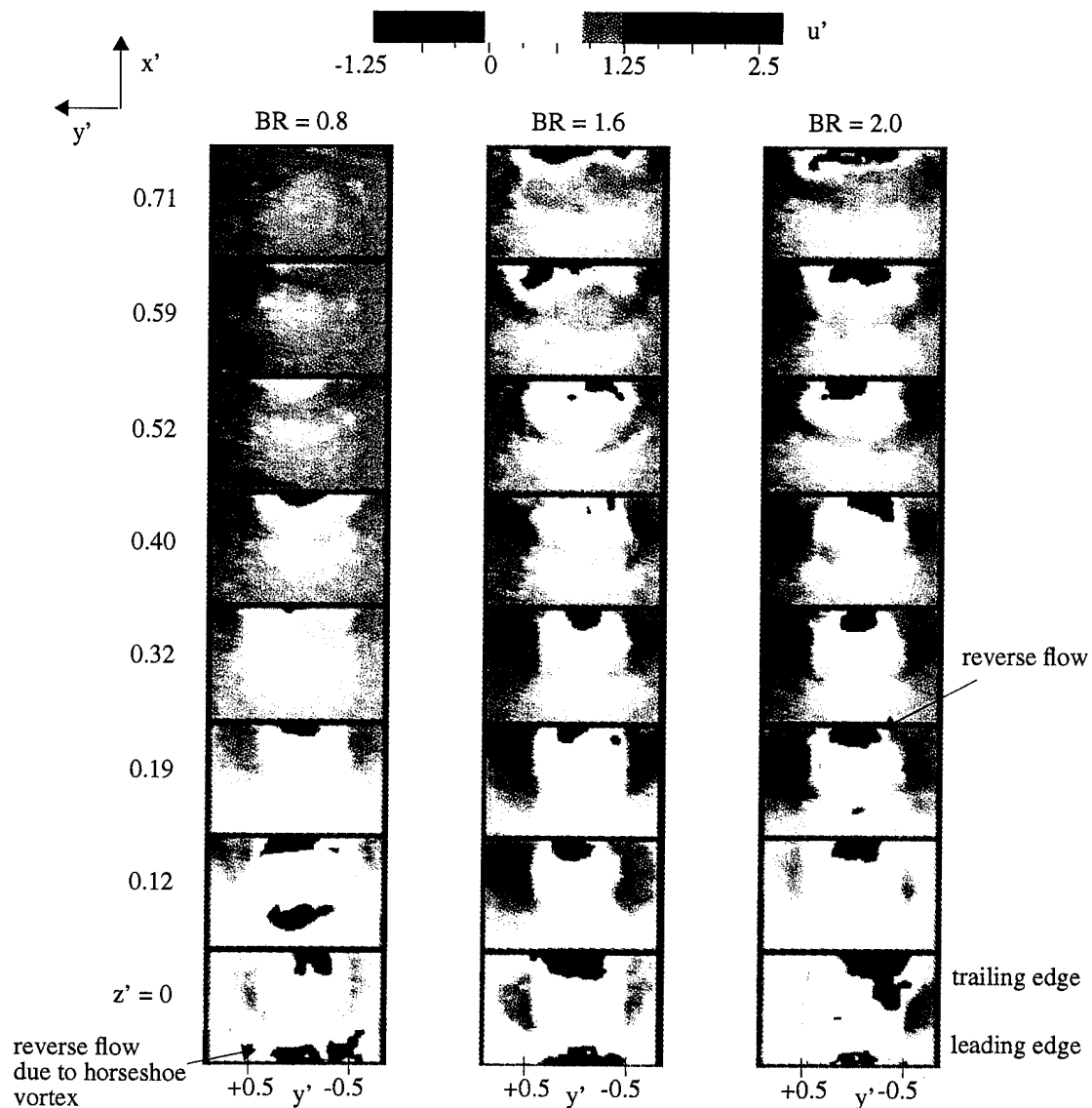
Figure 6-11: Hole 4: u'-Velocity in Planes Parallel to the Surface

the trailing edge, to be discussed below, realigns the vorticity toward the z-direction causing an induced velocity between the vortex pair in the negative x-direction.

Figure 6-13 gives the w'-velocity profile at the downstream edge of the hole, which shows the expected peak at the center, and a flow visualization picture at a laser sheet position of z' = 0.26. In reference to equation (4-10c), the presence of a velocity gradient, $\pm\dfrac{dw}{dy}$, on each side of the centerline suggests that a vortex pair aligned in the z-direction
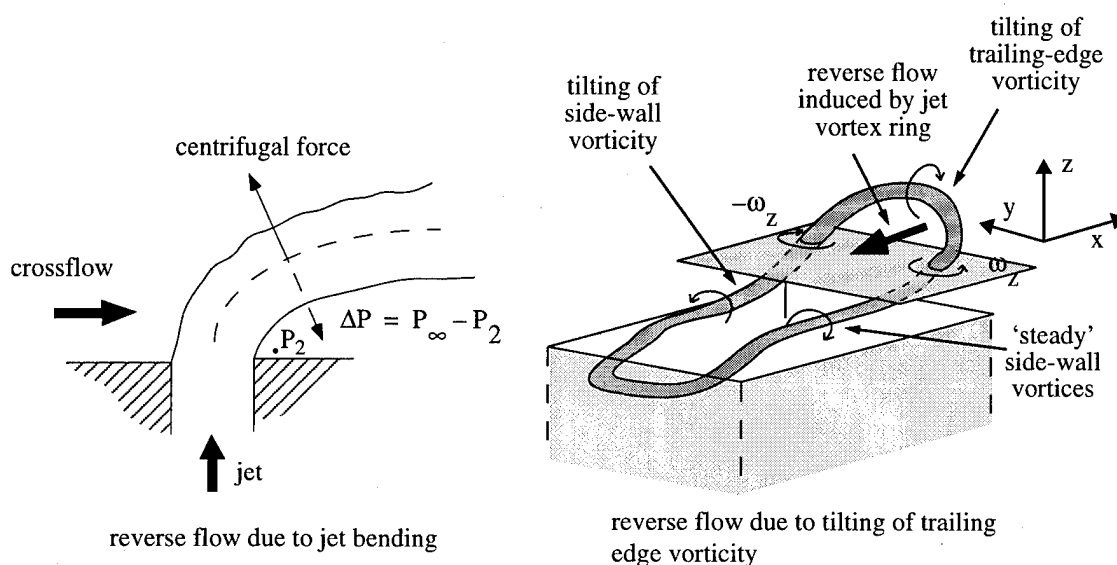
Figure 6-12: Reverse Flow due to Jet Bending and Tilting of Trailing Edge Vorticity

will be induced at the trailing edge of the hole by the vorticity tilting (see figure 6-12, right) similar to the one along the side-wall. Flow visualization on the right of figure 6-13 confirms that such a vortex pair, $(\omega_z, -\omega_z)$, exists at the downstream corners of the hole. Further downstream, these trailing edge vortices also become part of the kidney-pair. The kidney-vortices therefore consist of vorticity originally emanating from all walls of the hole.
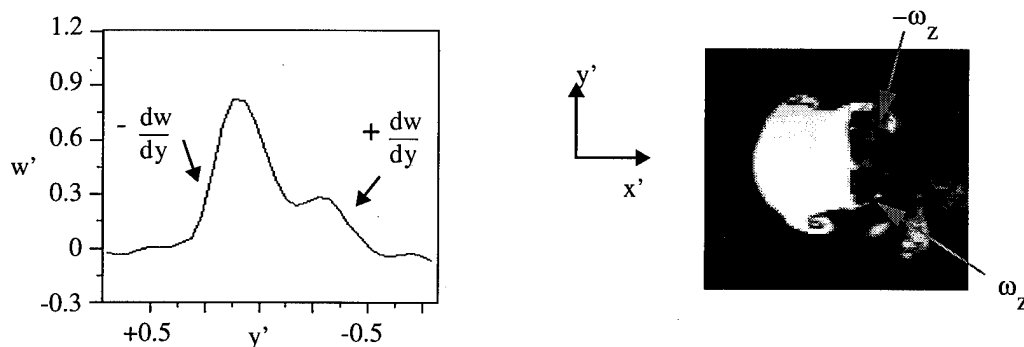
Figure 6-13: Hole 4: w'-Velocity Profile at Hole Trailing Edge; Flow Visualization at z'= 0.26, BR = 2.0

6.2 High Aspect Ratio Rectangle (Hole 6): $\longrightarrow$ ▯
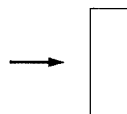
Compared to the square hole, the high aspect ratio rectangle, hole 6, has better attachment characteristics in the region downstream of the hole. As discussed in §3.2, the superior performance is predominantly due to the increased separation of the vortices formed from the side-wall vorticity. However, in addition to this increased separation, the hole geometry facilitates the formation of a 'negative' vortex pair. It is believed that such a negative pair can interact with the formative kidney-vortices, reducing their overall strength through annihilation.

6.2.1 'Steady' Kidney-Vortices and 'Negative' Vortex Pair

Evidence of a 'negative' vortex pair is seen in both the flow visualization pictures and PIV data. In figure 6-14a, a laser sheet intersecting the jet at the downstream edge of the hole reveals, not only the steady kidney-vortices due to the jet side-wall boundary layer already observed for a square hole, but an additional pair riding on top of the jet rotating in the opposite direction. This newly observed 'negative' vortex pair is contrary to what was seen previously for the square hole. In an experiment using the larger area rectangular hole, hole 6a, the leading edge boundary layer of the jet was seeded with a trace of fluorescein dye which was introduced inside the hole, 2.1 cm from the exit. The picture in figure 6-14b, taken at the mid-point of the hole, shows the dye pooling in the area where a 'negative' vortex pair is present. This suggests that the jet leading edge boundary layer is being warped in such a way as to induce a 'negative' vortex pair.
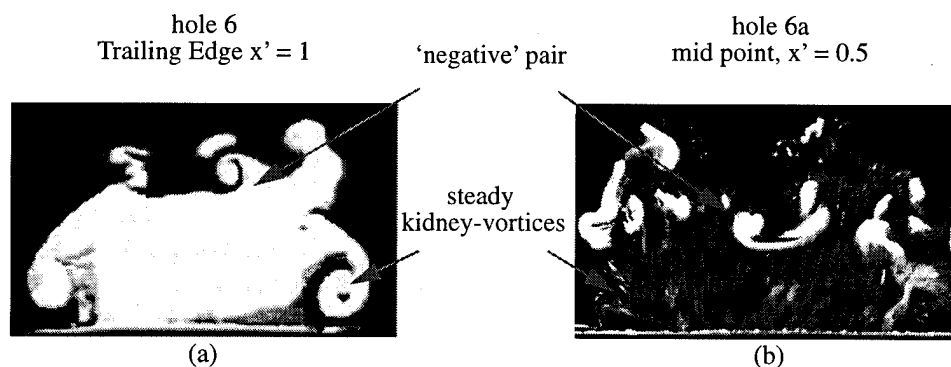
Figure 6-14: a) Entire Jet Dyed, b) Leading Edge Dye Traces for BR = 1.6

The PIV data in figure 6-15 gives further insight into the formation of the 'negative' pair. The vorticity plots for each blowing ratio represent the averaged flow field measurements taken at equal intervals along the x-axis of the hole, beginning at x' = 0.15. A distinct difference between these plots and those for the square hole (figure 6-1) is the addition of vortex pairs between the 'steady' side-wall kidney-vortices. Sitting near the hole centerline is a vortex pair which has the opposite sign relative to the kidney-vortex pair (e.g. x' = 0.45, BR = 2.0). The appearance of these additional vortex pairs is much less prevalent at the lower blowing ratios, showing up only at the trailing edge for a blowing ratio of 0.8. The flow visualization pictures, on top and taken at the downstream edge of the hole, confirm the presence of a 'negative' vortex pair for all blowing ratios.

Plots of the lateral velocity, v', for all three blowing ratios show the same side spillage as that for the square hole (figure 6-16). Because the side-wall vortices stay closer to the surface, the lateral flow back toward the centerline only happens at the downstream edge of the hole and for the highest blowing ratio.

The vertical velocity plots in figure 6-17 exhibit low velocity regions near the centerline of the hole (compare with figure 6-3 for a square hole). These depressions correspond to the 'negative' vortex pairs observed in figure 6-15. As in the case of the square hole, there is a region of negative w'-velocity near the leading edge of the hole for blowing ratios of 0.8 and 1.6. At the highest blowing ratio, 2.0, the jet overcomes the negative velocity induced by the horseshoe vortex and emerges from the hole near the leading edge at x' = 0.15 (data were not taken at x' = 0).

6.2.2 Vortex Realignment by Tilting of Side-Wall Vortex Sheet

The w'-velocity profiles along the hole centerline and edge are shown in figure 6-18 for blowing ratios of 0.8 and 1.6. The velocity gradient along the side of the jet indicates the upward tilting of the side-wall vorticity as it is convected downstream. The saddle-shaped velocity distribution previously observed for the square hole along its edges is absent here., as expectd; for the high aspect ratio rectangle, the close proximity of the leading and trailing edges eliminates the middle depression in the induced velocity. Vorticity plots in the plane parallel to the plate at z' =0.12 show vorticity concentrations, ω'_z, along the sides of the jet due to the realignment of the side-wall vorticity toward the z-direction.

63
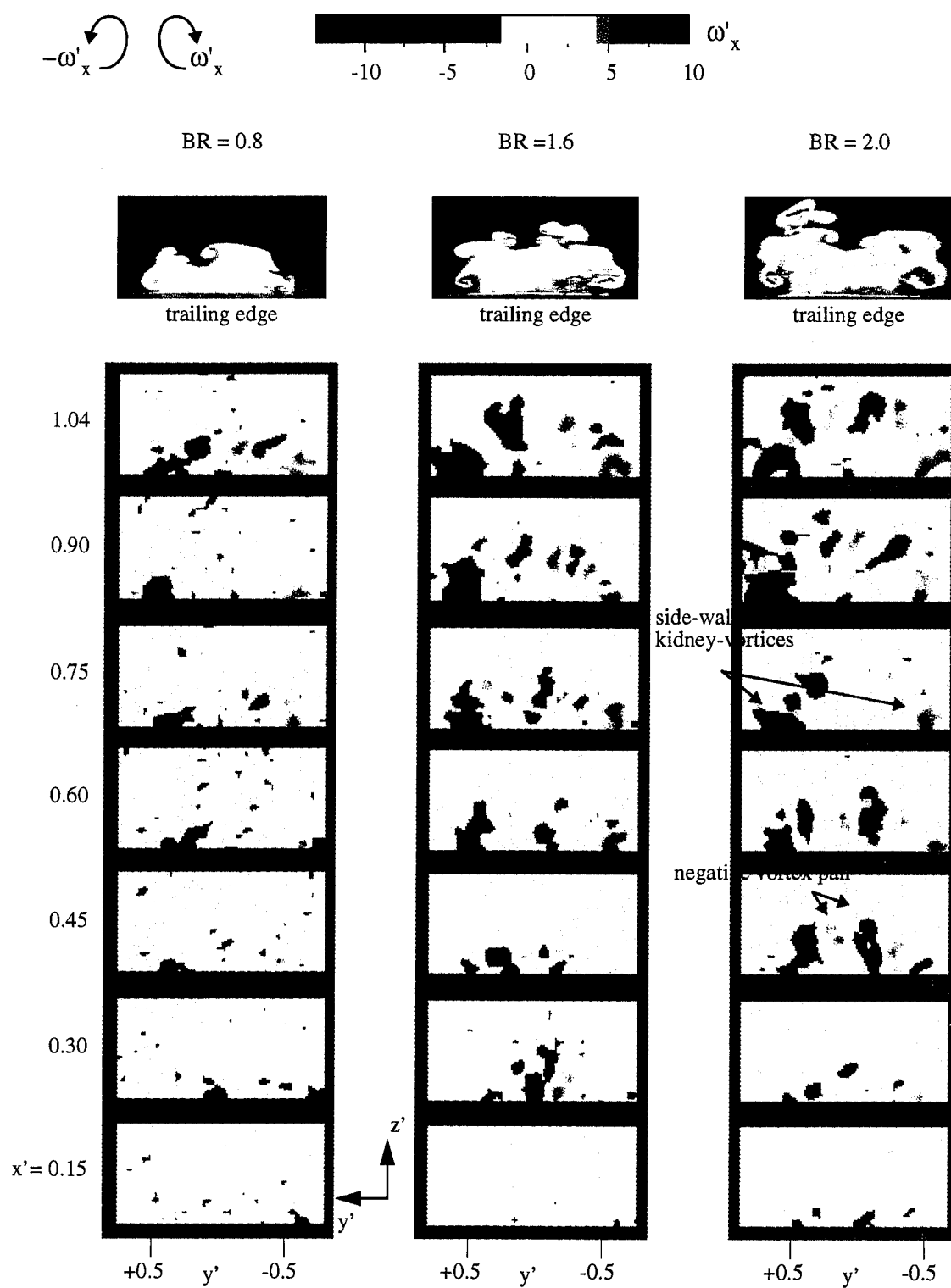
Figure 6-15: Hole 6: Flow Visualization and PIV Vorticity Plots, BR = 0.8, 1.6, and 2.0
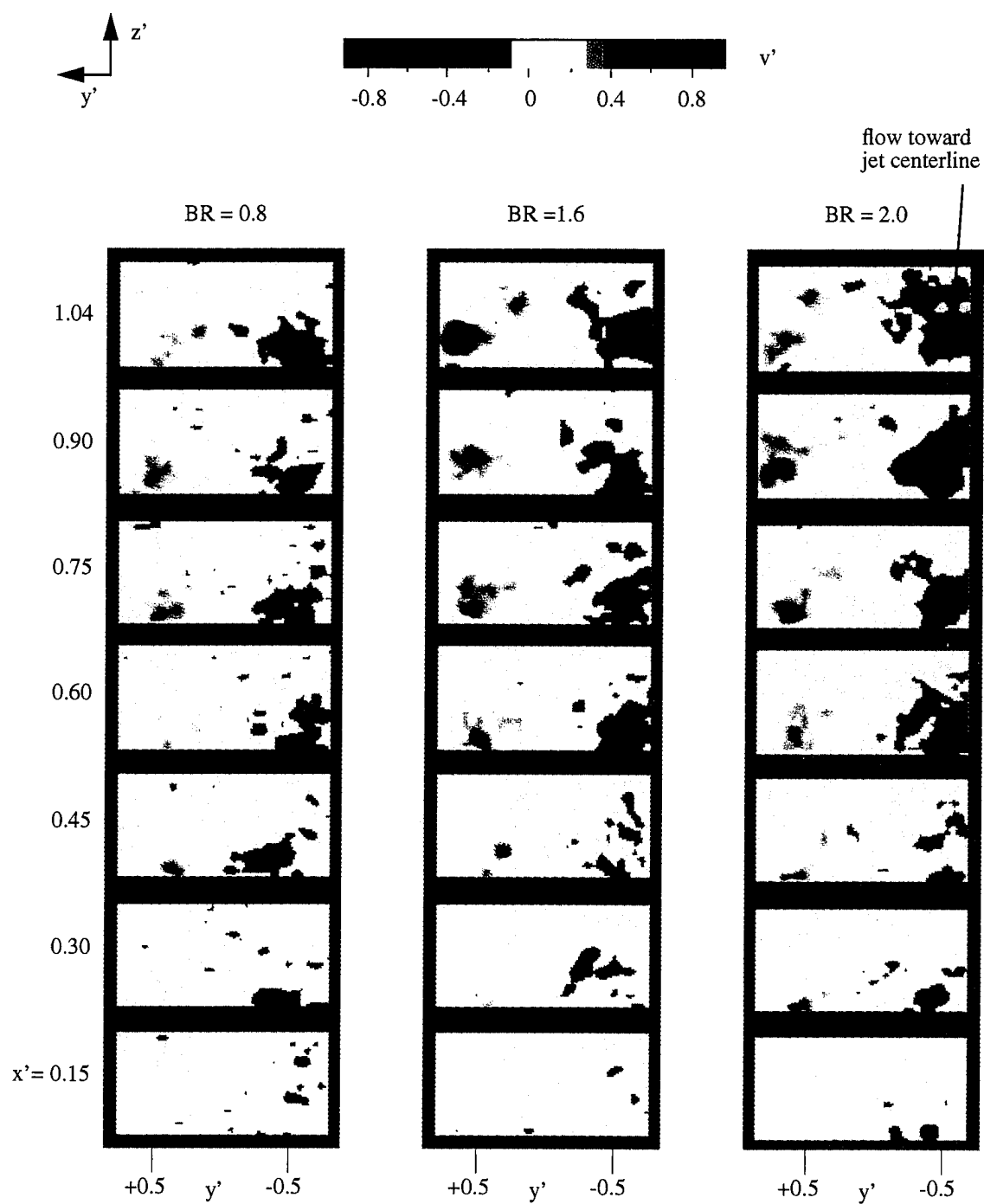
Figure 6-16: Hole 6: v'-Velocity Profile, BR = 0.8, 1.6, 2.0
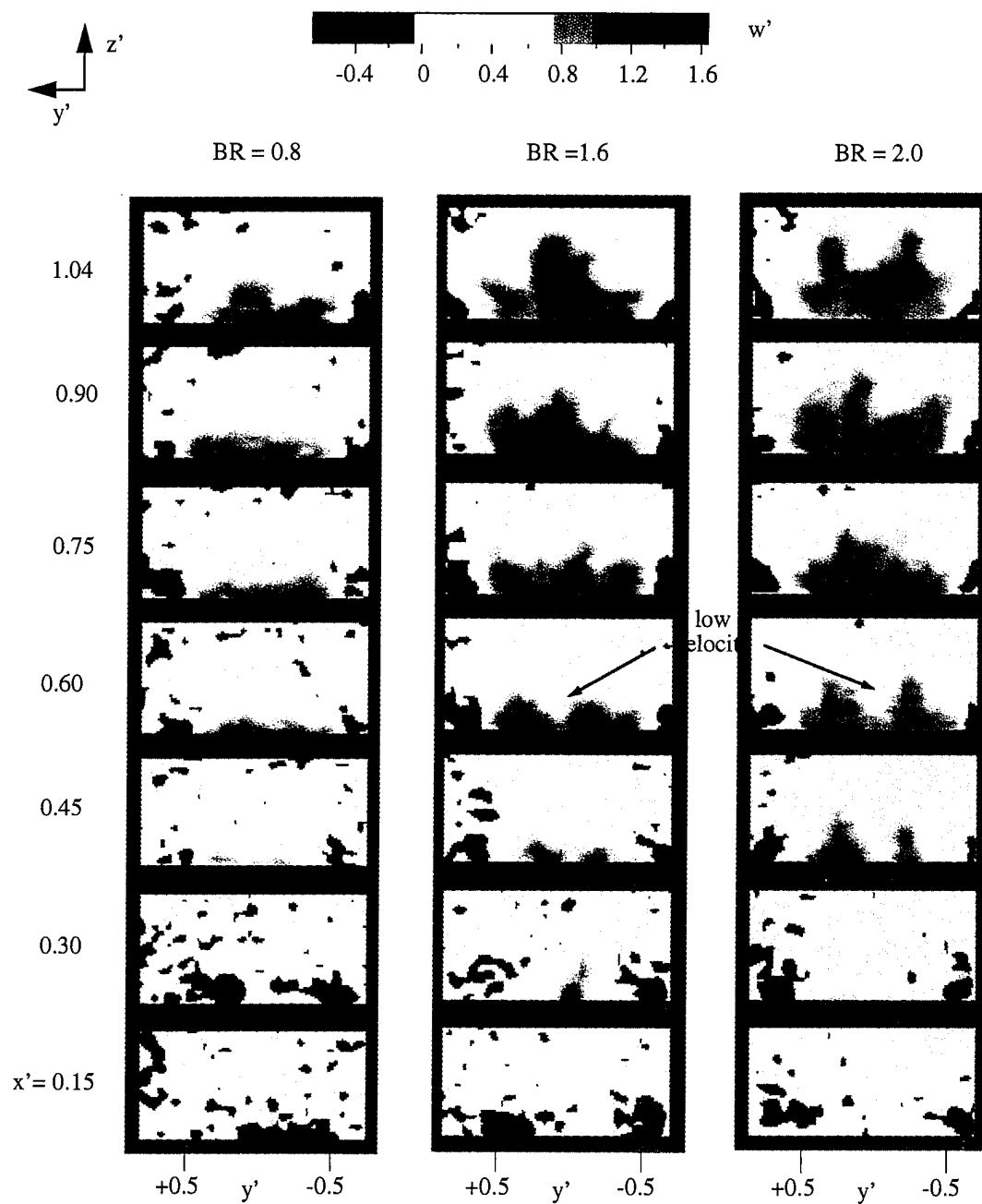
Figure 6-17: Hole 6: w'-Velocity Profile, BR = 0.8, 1.6, 2.0.

Again, the jet side-wall vorticity is seen all along the sides of the hole, beginning just downstream of the leading edge.
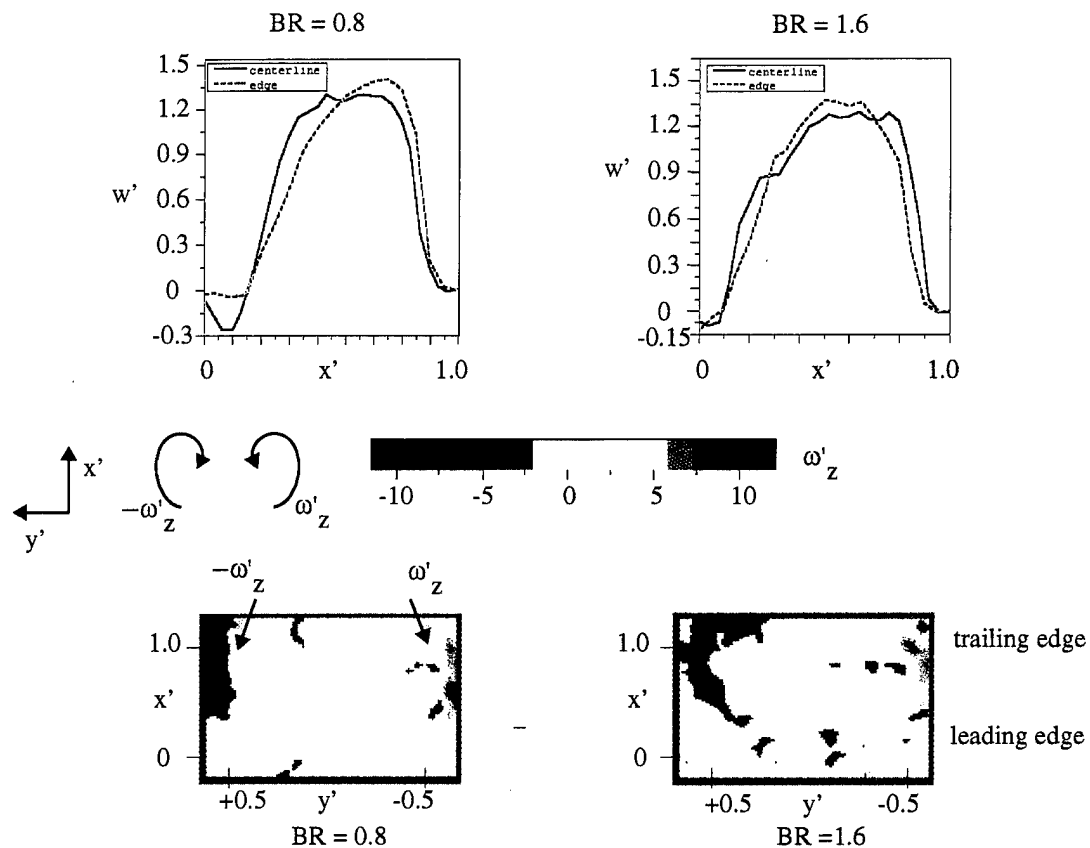
Figure 6-18: Hole 6: Side-wall Velocity Profiles and Vertical Vorticity at z' = 0.12, BR = 0.8 and 1.6

6.2.3 Vorticity Realignment by Warping of Leading Edge Vortex Sheet

The vorticity formation by the warping of the leading edge vortex sheet is more complex for the rectangular hole than the square. While for the square hole, the warping produced an unsteady vortex pair having the same sign as the kidney-vortices. For the rectangular hole, this warping can induce a 'negative' vortex pair as already seen in figure 6-14. A proposed mechanism for the formation of the 'negative' pair was proposed previously in §4.2: when the crossflow interacts with the jet, it pushes the leading edge vortex sheet downstream and upward as illustrated in figure 6-19. This stretching and realignment of vorticity induces both perpendicular and streamwise vorticity components, ω_z and ω_x, having the sense of rotation of the 'negative' pair.
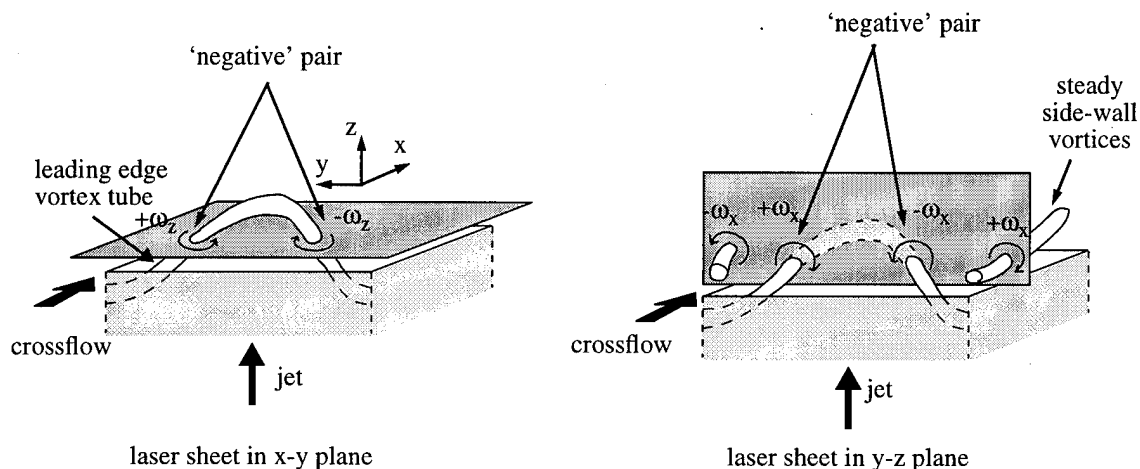
Figure 6-19: Hole 6: Vorticity Realignment due to Tilting of Leading Edge Vorticity

Figure 6-20 shows the velocity vector plot, u'-velocity profile, and the vorticity plot for a blowing ratio of 1.6 in the horizontal plane at z' = 0.52. In the u'-velocity profile, a peak is present near the center, while for the square hole, a depression was present there (figure 6-8). The sign of the lateral variation of u, $\dfrac{du}{dy}$, is therefore reversed from the one for the square hole. This corresponds to the 'negative' pair shown near the center of the PIV vorticity plot ($-\omega'_z$ for y<0 and ω'_z for y>0).

The 'negative' pair is clearly observable in the flow visualization picture on the right of figure 6-20, which shows the top part of the jet. In this picture, the blowing ratio is 0.91 and the laser sheet is located at z' = 0.71. Cutting near the top of the jet reveals two large counterrotating vortices, or 'negative' vortex pair, at the leading edge of the jet. The dark crossflow fluid along the centerline of the jet indicates a region of higher streamwise velocity. This counter-rotating vortex pair is formed within the jet fluid on either side of the penetrating crossflow, which then induces an additional streamwise velocity component. This induced velocity reinforces the penetration of the crossflow further into the jet as shown in figure 6-19.
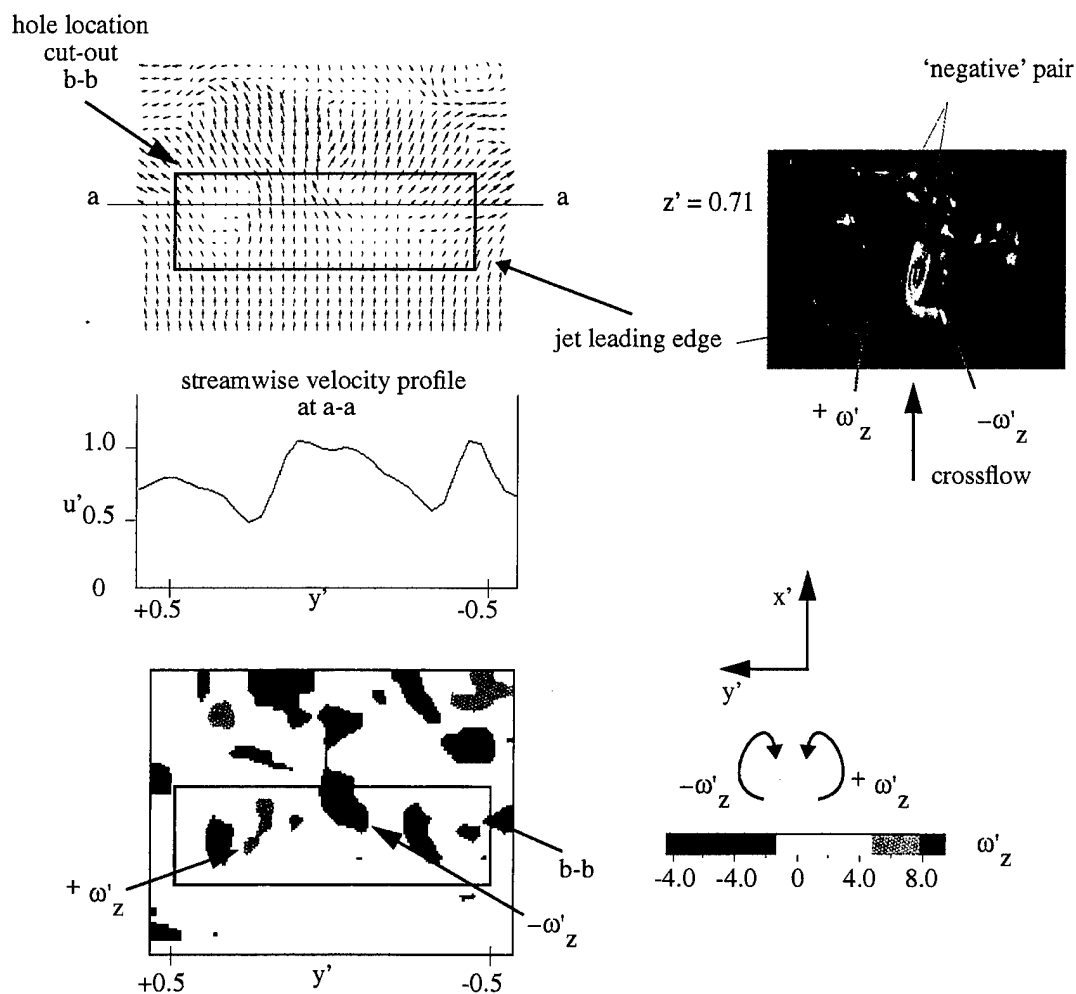
Figure 6-20: Hole 6: z-Vorticity Realignment at Jet Leading Edge

6.2.4 Tilting of Hole Trailing Edge Vorticity

The reverse flow region just downstream of the jet shown in figure 6-21 is similar to that seen for the square hole (figure 6-11). It extends to the entire span of the hole, basically following the straight line of the hole exit contour, with greater penetration at the corners (for a direct flow visualization of this, refer to Krothapalli, Lourenco, and Buchlin, 1990).

The proposed mechanism for this is again due to the bending of the jet and the tilting of the trailing edge vorticity.
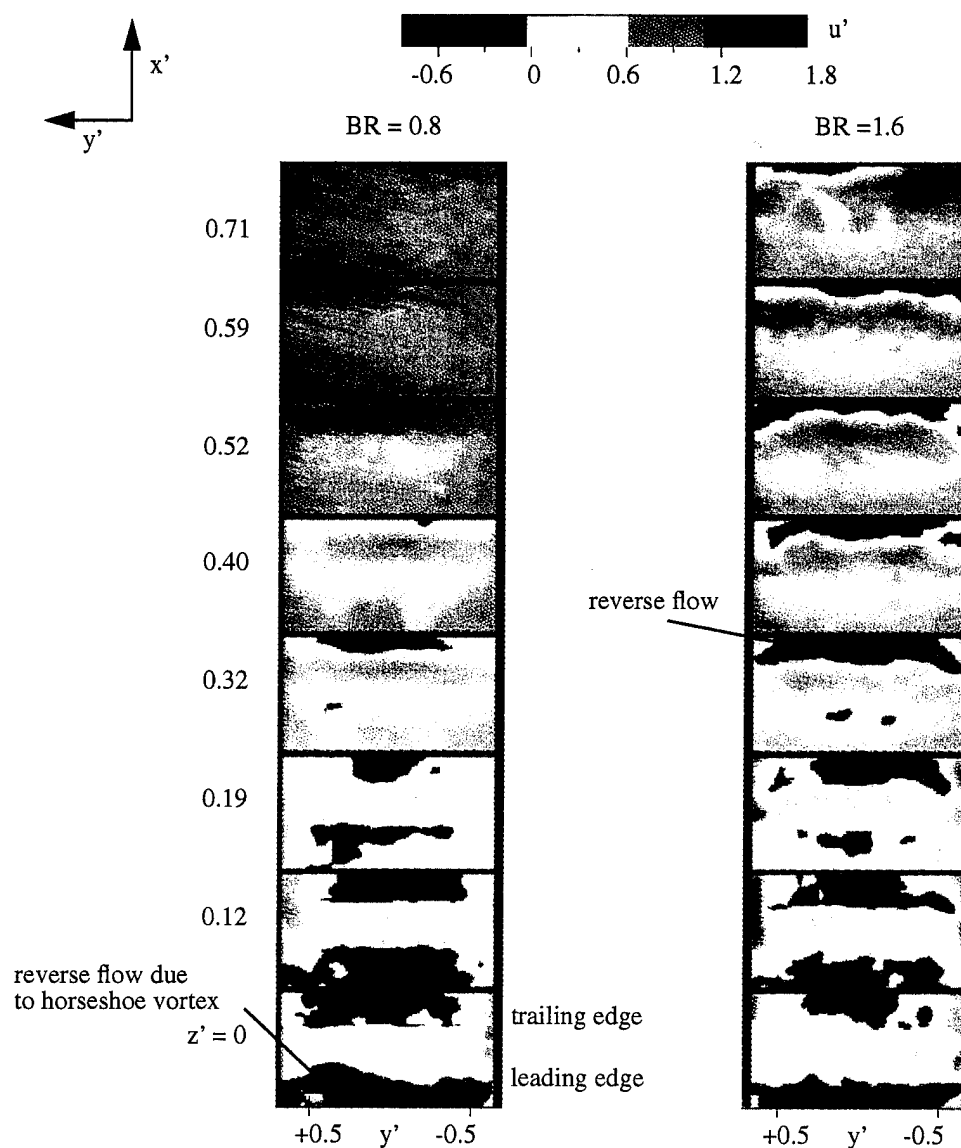
Figure 6-21: Hole 6: u'-Velocity in Plane Parallel to Plate, BR = 0.8 and 1.6

The w'-velocity profile at the trailing edge of the hole is given in figure 6-22. The adjacent flow visualization picture taken for z' = 0.26 shows the two counter-rotating vortices at the downstream corners of the hole that are induced as the result of the tilting of the trailing edge vorticity.
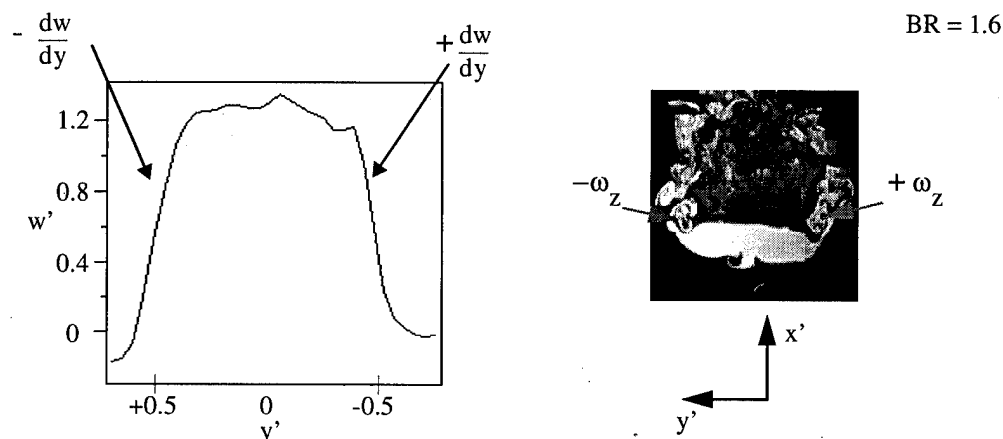
Figure 6-22: Hole 6: w'-Velocity Profile at x' = 1.0 and Flow Visualization Parallel to the Plate at z' = 0.26, BR = 1.6

6.3 High Aspect Ratio Ellipse (Hole 5): ⟶ ◯
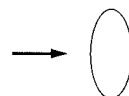
Not surprisingly, the high aspect ratio ellipse has many of the same characteristics as the high aspect ratio rectangle, including the appearance of a 'negative' vortex pair on top of the jet. The rectangle was presented prior to the ellipse because the geometry more clearly distinguishes the different sources of vorticity within the jet passage, i.e. side-wall, leading edge, and tailing edge boundary layers.

6.3.1 'Steady' Kidney-Vortices and 'Negative' Vortex Pair

The PIV data in figure 6-23 are instantaneous vorticity fields showing the presence of additional 'negative' vortex pairs between the side-wall kidney vortices for the blowing ratios of 1.6 and 2.0. For the lowest blowing ratio, 0.8, a 'negative' pair is only seen near the leading edge at x' = 0.34.
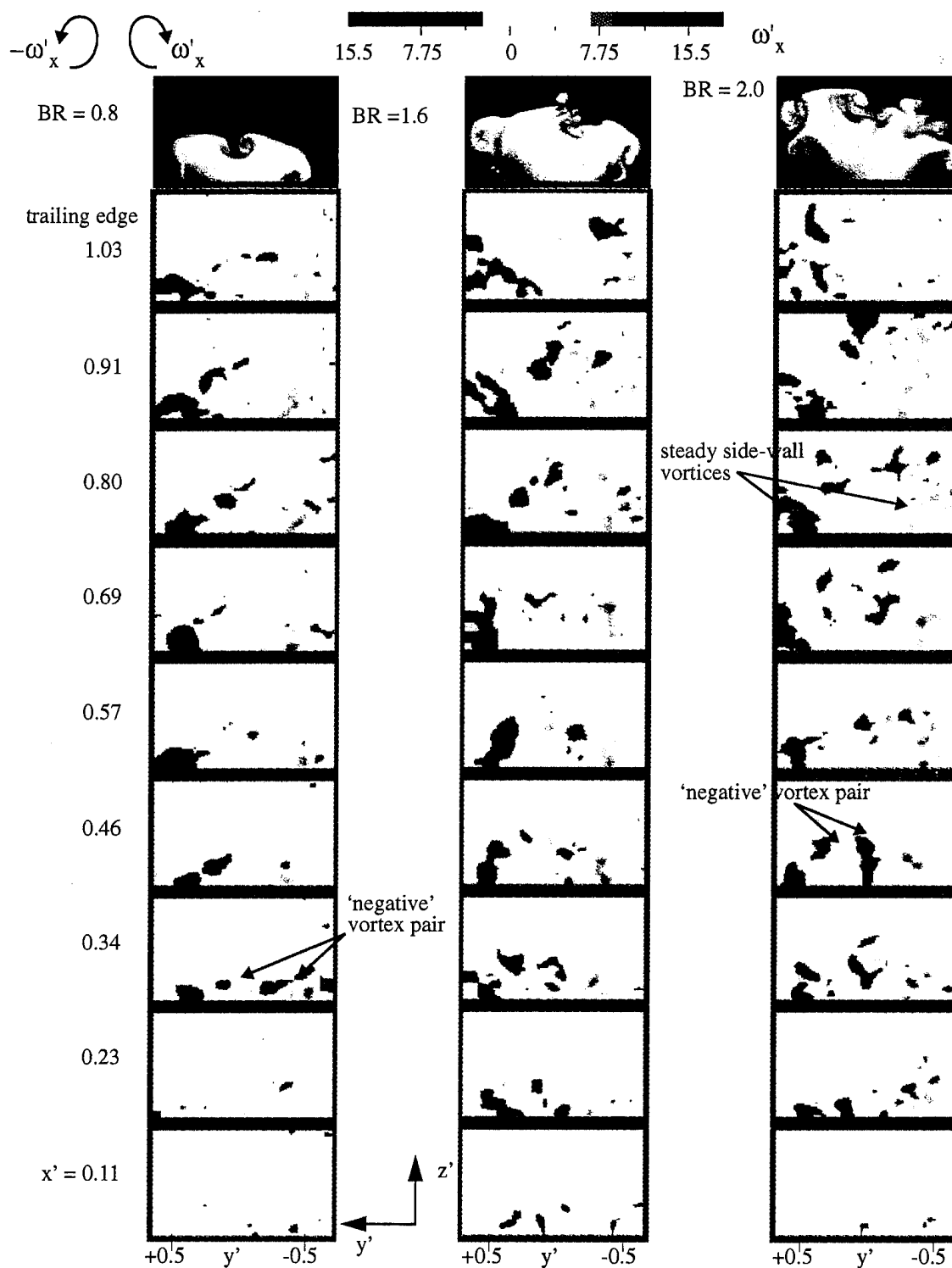
Figure 6-23: Hole 5: Flow Visualization and Instantaneous PIV Vorticity Plots, BR = 0.8, 1.6 and 2.0

The corresponding vertical velocity plots, in figure 6-24, reveal again a velocity deficit near the centerline of the hole where the 'negative' vortex pair was observed in figure 6-23. Flow visualization shown at the top of figure 6-23 confirms once again that the depression caused by the velocity deficit corresponds to the 'negative' pair.

The flow visualization pictures in figure 6-25, taken in the y-z plane at the middle of the hole, x' = 0.5, highlight the 'negative' pair. The crossflow boundary layer was seeded with fluorescein dye 4 cm downstream of the plate leading edge. As the crossflow rides over the top of the jet, the crossflow fluid, along with the fluorescent dye, is drawn into the jet by the vortex pair at the top of the jet. At the lower blowing ratios, where the jet has less penetration into the crossflow, the fluorescein dye from the crossflow collects in the depressed region of the jet. The outline traced by the fluorescent dye is that of a counterrotating 'negative' vortex pair. As the blowing ratio increases, the amount of fluorescent dye captured by the jet decreases. An explanation is that the higher jet velocity creates more of an obstruction to the crossflow causing the earlier roll-up of the crossflow boundary layer boundary layer into the horseshoe vortex. The horseshoe vortex, along with the fluorescent dye, is then forced around the sides of the jet, minimizing the amount of fluorescent dye that makes it into the depressed regions of the jet.

6.3.2 Vortex Realignment by Tilting of Side-Wall Vortex Sheet

The vorticity plots shown in figure 6-26, taken at the plate surface, are similar to those for the low aspect ratio rectangle. Along the edges of the hole, the vorticity has been tilted so that the z-component is induced, the elliptical outline of which corresponds to the hole contour.

6.3.3 Vorticity Realignment by Warping of Leading Edge Vortex Sheet

The warping of the leading edge, as mentioned in §6.1.3, is an intermittent, or unsteady, processes. Therefore, the vorticity associated with the leading edge of the jet shows up intermittently in the flow visualization pictures and PIV data.

Figure 6-27 compares the averaged vorticity (averaged using four sets of data) to one of the instantaneous files for each z-location above the plate for BR = 1.6. The averaged
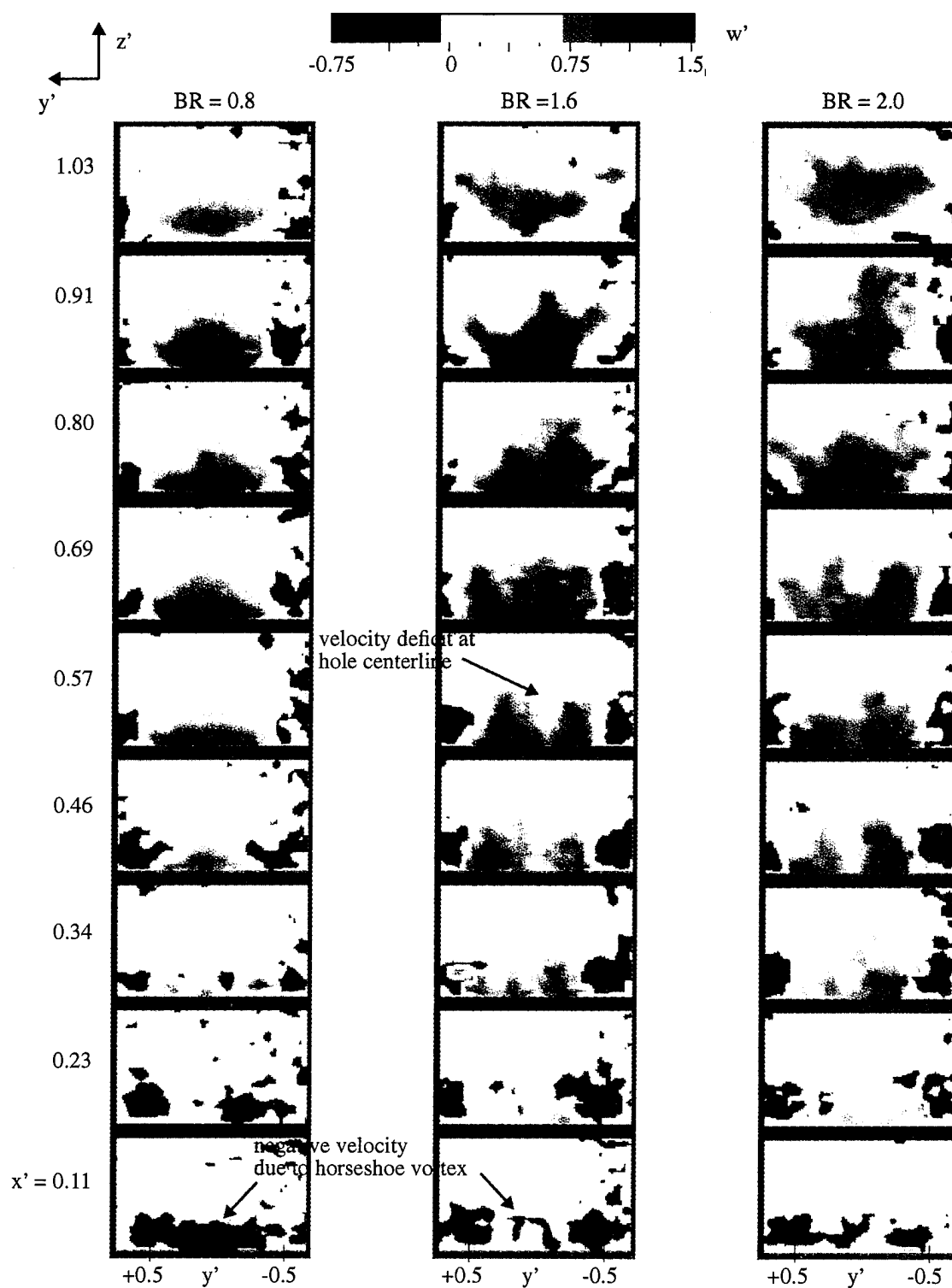
Figure 6-24: Hole 5: Instantaneous w'-Velocity Plots, BR = 0.8, 1.6, and 2.0
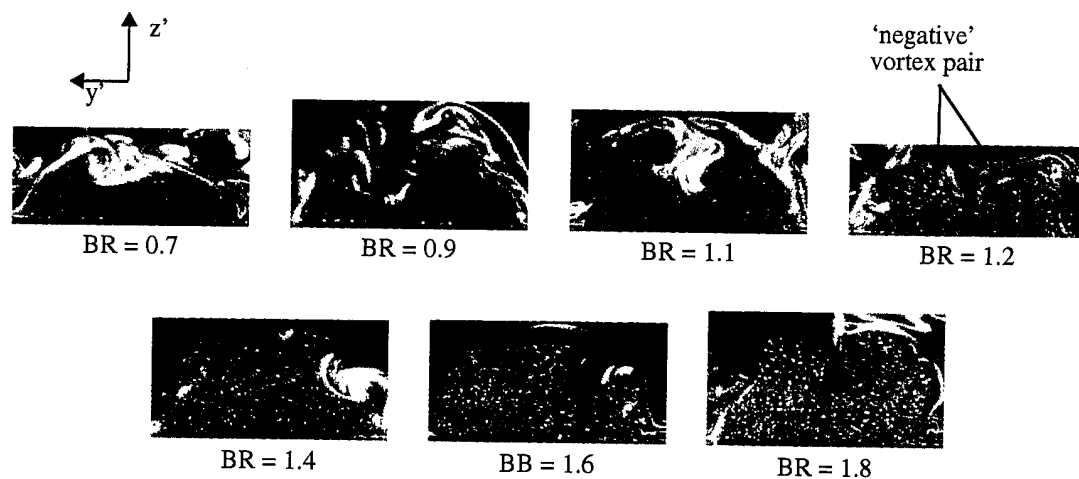
Figure 6-25: Hole 5: Flow Visualization - Boundary Layer Seeded with Fluorescein Dye, Laser Sheet at $\dot{x}' = 0.5$
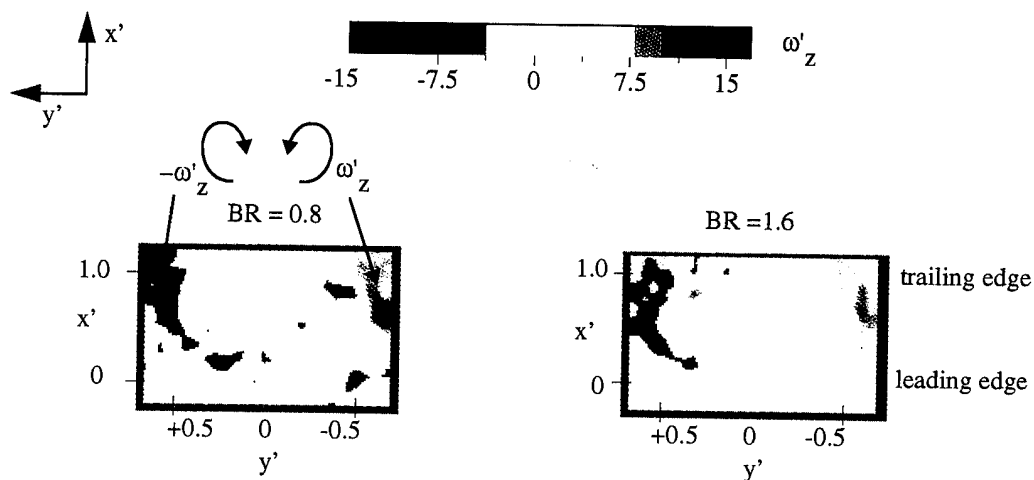
Figure 6-26: Hole 5: Side-wall Velocity Profiles and Vertical Vorticity, $z' = 0$, BR = 0.8 and 1.6

file shows virtually no vorticity toward the leading edge of the jet, as already observed on the right of figure 6-26. The instantaneous file, however, shows much more activity. For the cross-sections at $z' = 0.19$ and $z' = 0.40$, additional 'positive' vorticity (ω'_z on the right, $-\omega'_z$ on the left) is induced, having the same sense of rotation as the kidney-vorti-

ces. At z' = 0.32, the instantaneous plot shows the presence of a 'negative' vortex pair ($-\omega'_z$ on the right, ω'_z on the left) at the jet leading edge. At the furthest location away from the plate, z' = 0.71, there are multiple vortex pairs, indicating extensive warping of the leading edge boundary layer vorticity. It should be kept in mind that the sequence of plots shown in figure 6-27 does not portray the entire jet at a single instant in time; rather each individual cross-section was acquired independently.
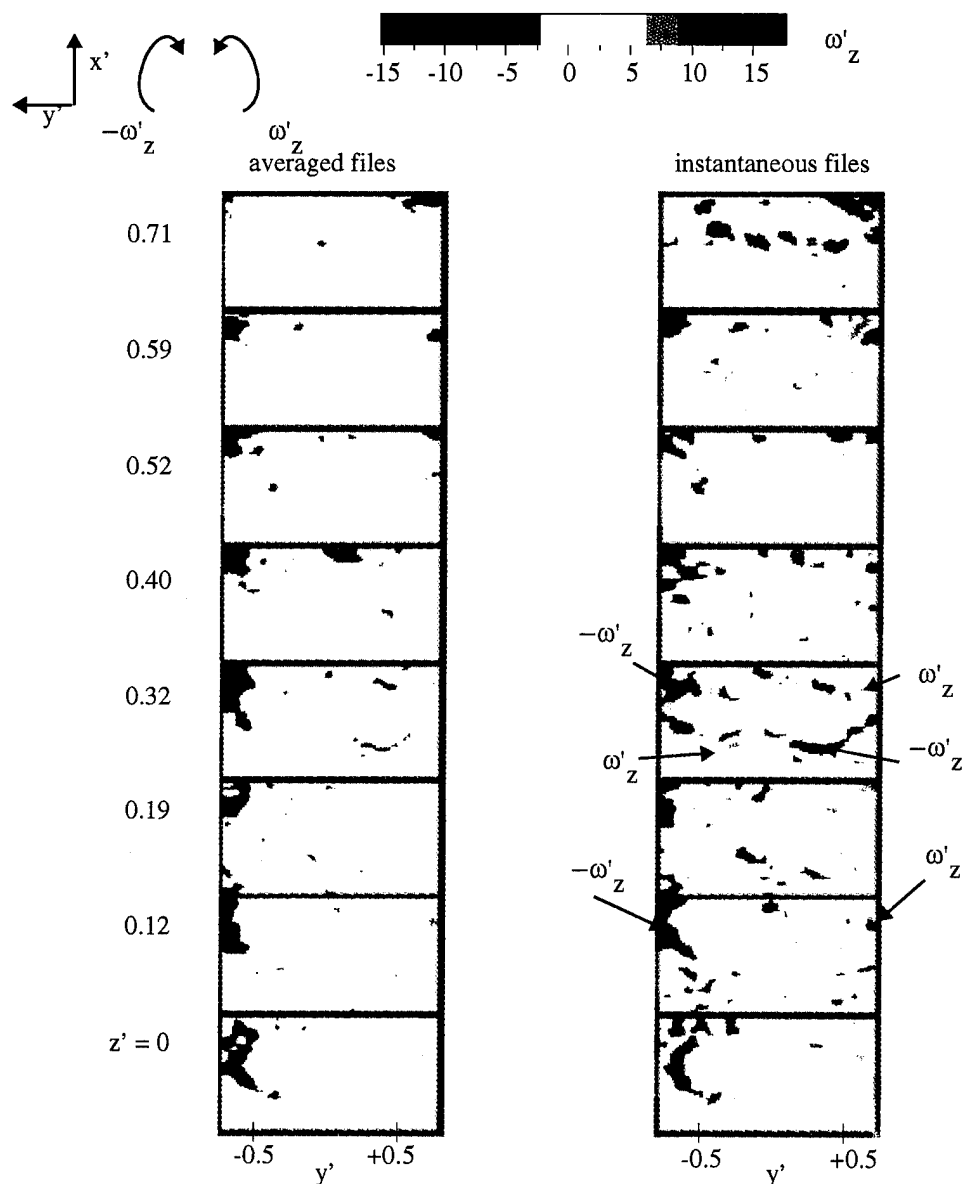
Figure 6-27: Hole 5: Averaged and Instantaneous Vorticity Plots, BR = 1.6

Flow visualization pictures taken at z' =0.26 above the surface show the slight deformation at the leading edge of the jet (figure 6-28). For a blowing ratio of 2.0, a 'negative' vortex pair is clearly present.

BR = 1.6   BR = 2.0

crossflow   leading edge deformation   'negative' vortex pair
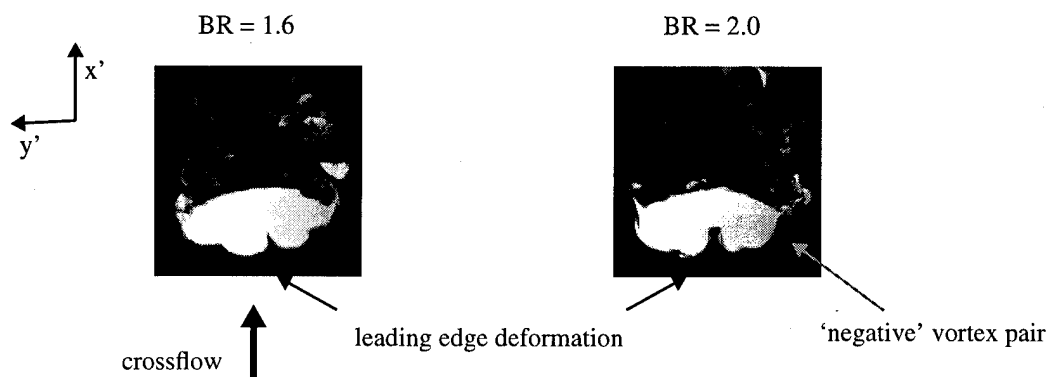
Figure 6-28:   Hole 5: Jet Deformation at Leading Edge, z' = 0.26

6.3.4 Tilting of Hole Trailing Edge Vorticity

The flowfield at the trailing edge of hole 5 is similar to that for the high aspect ratio rectangle, hole 6. The curvature of the hole, however, slightly alters the location where the trailing edge vorticity is turned toward the z-axis. The flow visualization pictures in figure 6-29 show a pair of counterrotating vortices near the middle of the hole. This is in contrast to the rectangular hole where the vortices were seen closer to the downstream corners of the hole (figure 6-22).

BR = 0.8   BR = 1.6   BR = 2.0

crossflow   vortices formed near middle of hole
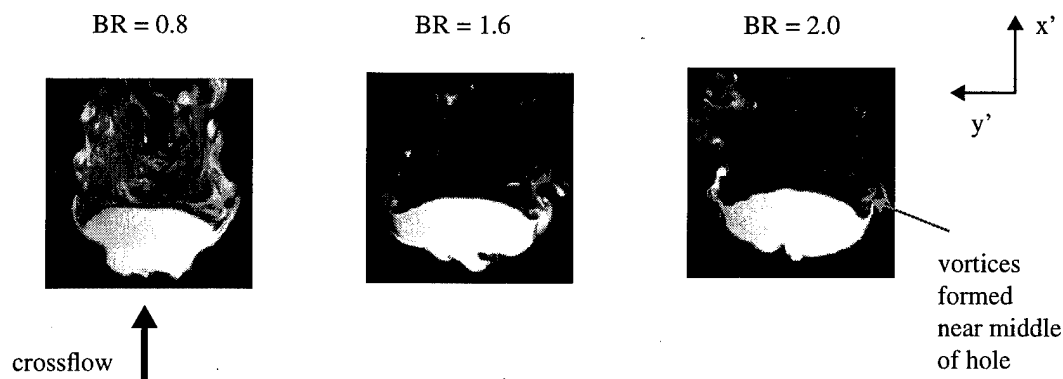
Figure 6-29:   Hole 5: Lift up of Trailing Edge Vorticity, z' = 0.26

As in the case of hole 6, the negative u'-velocity is due to the bending of the jet and the induced velocity associated with the lifting of the trailing edge vorticity.
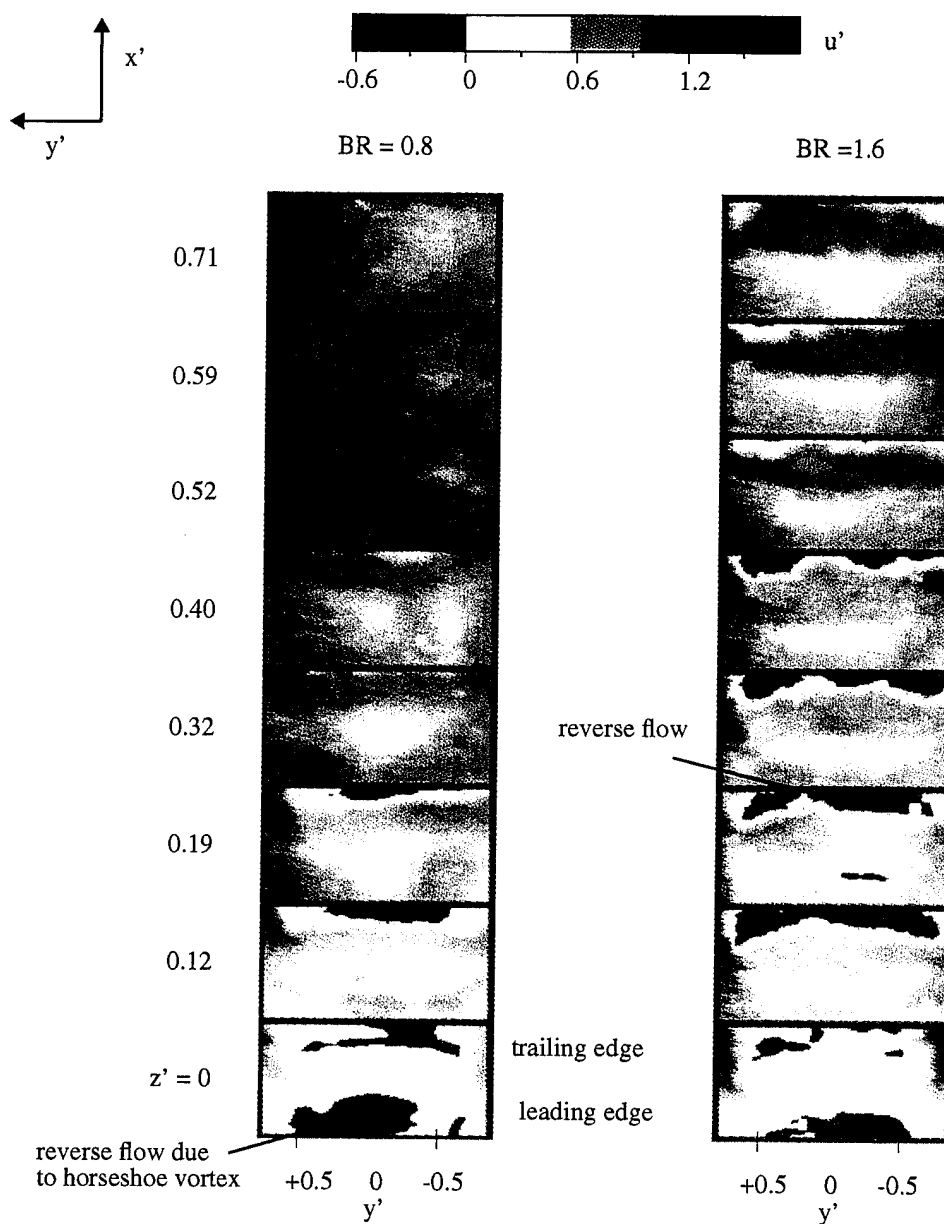
Figure 6-30: Hole 5: u'-Velocity in Plane Parallel to Plate, BR = 0.8 and 1.6

6.4 Round (Hole 3)

The round hole is by far the most studied geometry for a jet in a crossflow. From the stand-
point of understanding the vortex dynamics, however, the round hole is perhaps the most
difficult because its curvature eliminates any distinction between the vorticity arising from
the leading and trailing edges, and that due to the hole side-wall boundary layer.

The overall characteristics of the round jet are similar to those found in the literature.
For instance, the u'-velocity profiles, measured by PIV at three points along the hole cen-
terline, shown in figure 6-31, are consistent with those obtained by Andreopoulos and
Rodi (1984, figures 5a and 6) for BR = 0.5 and 1.0. Additional comparisons with other
available data will be presented shortly.
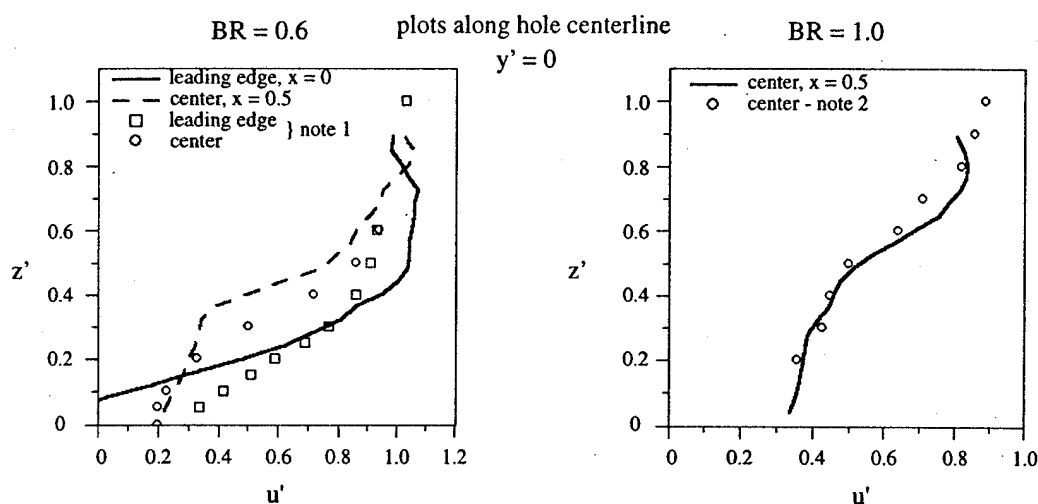
note 1: data from Andreopoulos & Rodi (1984) for BR = 0.5
note 2: data from Andreopoulos & Rodi (1984) for BR = 1.0

Figure 6-31: Hole 3: u'-Velocity Profiles at Leading Edge and Center for BR = 0.6 and
Center for BR = 1.0

Contrary to the other data, which were based on such point-measurements as 3D hot
wire or Laser Doppler Velocimetry (LDV) techniques, PIV used here can capture the com-
plete flow field simultaneously. This unique capability, combined with the understanding
accrued from the other shapes, enables us to answer the question left unanswered in the
past studies on round holes: besides the side vorticity which emerges from the two side

points located furthest apart across the hole, how does the vorticity corresponding to the remainder of the hole circumference contribute to the kidney-pair?

According to the results presented herein, all other vortices do contribute to the kidney-pair, just like the other hole. Thus, it is unnecessary to invoke the postulate of annihilation between other vortices, such as those at the leading and trailing edges, which was proposed by Scorer (1958) and others to explain why only the streamwise vorticity appears in the downstream.

In addition to clarifying this issue, the present data reveals the presence of a 'negative' pair near the trailing edge, which serves to mitigate the 'positive' pair. In this sense, the effect of the trailing edge is beneficial.

The flow visualization and PIV results for the round hole will be presented in the same general format as the previous three holes. Although the curvature of the hole makes it difficult to distinguish between the source of jet vorticity, the general location of the flow features coupled with the experience obtained from the previous results, will be used as a basis for discussion.

6.4.1 'Steady' Kidney-Vortices and 'Negative' Vortex Pair

In comparing the vorticity plots for the round hole (figure 6-32) with those for the square (figure 6-1) or baseline configuration, the primary difference can be seen near the trailing edge of the hole. At the higher blowing ratio, the round hole data shows a 'negative' vortex pair appearing near the surface of the plate: BR = 1.6 and x' = 0.97, BR = 2.0 and x' = 0.89 and 1.05. The presence of this 'negative' vortex pair at the trailing edge will be discussed further in §6.4.4.

When the flow visualization and PIV results in figure 6-32 are compared, a 'negative' vortex pair does not appear to be riding on top of the jet, in contract to the one noticed for the high aspect ratio rectangle and ellipse. Rather, the flow visualization pictures above the vorticity plots show the top vortices to be a 'positive' pair, similar to the steady ones below.

The w'-velocity plots are shown in figure 6-33. The rounded profiles are much like those for the square hole. As with all the holes, the velocity at the leading edge is in the
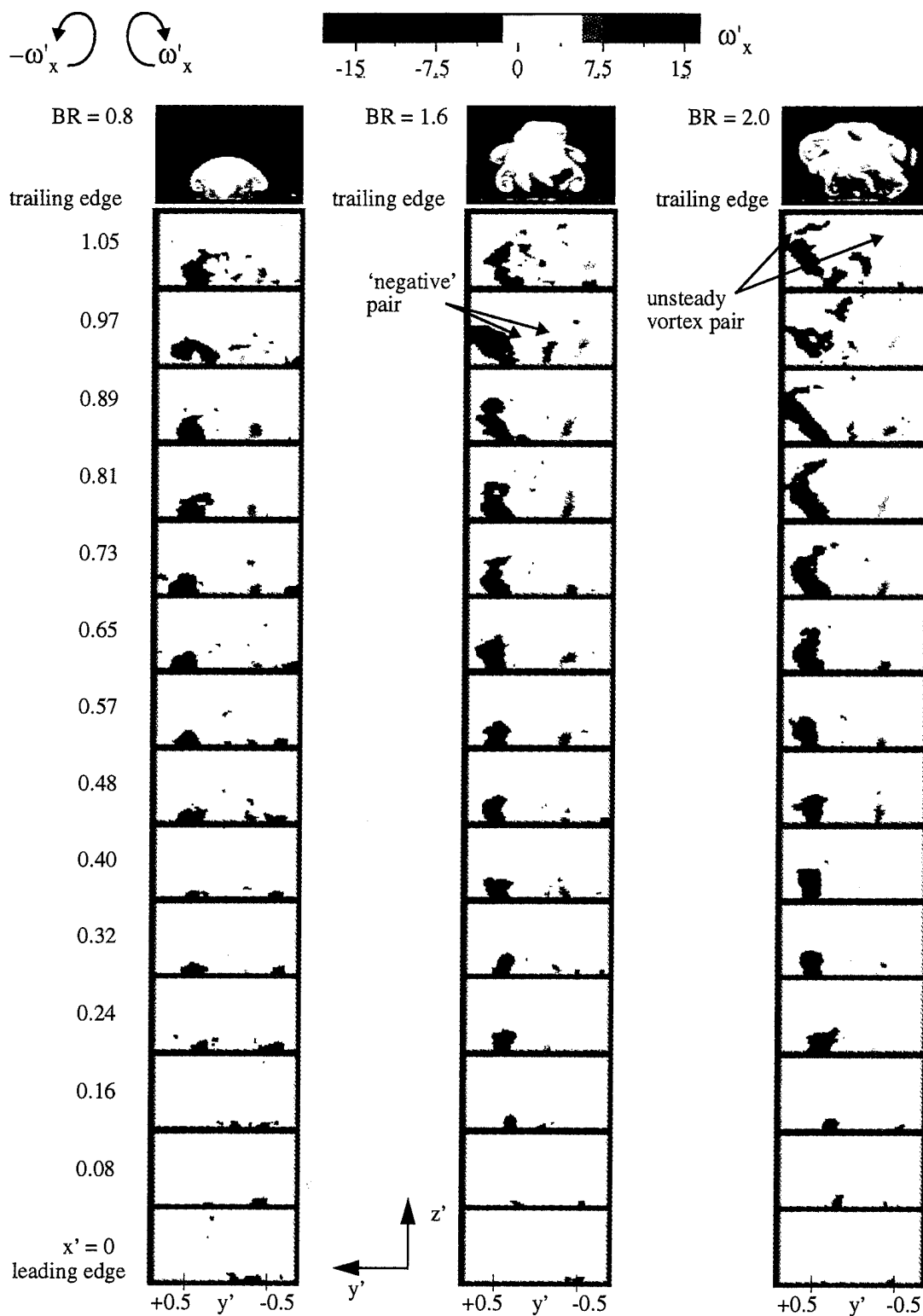
Figure 6-32: Hole 3: Flow Visualization and PIV Vorticity Plots, BR = 0.8, 1.6, and 2.0

negative z-direction. This negative velocity also explains the C_p data from Fearn and Weston (1975) and Sugiyama (1995) which show that at the leading edge of the hole there is no stagnation point as there would be for the case of flow around a solid cylinder. Instead of the crossflow stagnating as it comes in contact with the jet, the velocity induced by both the plate horseshoe vortex and the hole leading edge vortex sheet causes, as mentioned before, a negative velocity region near the hole leading edge. The value of C_p in this region should therefore be lower than that corresponding to a stagnation point. The results of Sugiyama (1995) show the value of C_p to be around 0.5 for a blowing ratio of 0.98, and 0.7 for a blowing ratio of 1.96, as compared to 1.0 for the cylinder. This region of negative velocity is further confirmed in flow visualization experiments by Fric (1994). In air, using smoke lines to trace the path of the crossflow, the smoke line nearest the plate surface is drawn into the hole at the leading edge (figure 6-34).

6.4.2 Vortex Realignment by Tilting of Side-Wall Vortex Sheet

As in the case for the previous holes, the vorticity along with side-walls of the hole is lifted up as a result of the skewing of the w-velocity profile at the exit plane of the hole. The w'-velocity profiles at the exit plane, shown in figure 6-35, agree in general with the data obtained by Crabb, Durao, and Whitelaw (1981) and Andreopoulos (1982). Their data, however, do not show the negative velocity (except for one data point in figure 1(a) of Crabb *et al).* The downstream increase of w, or skewness, observable at the exit plane implies, as pointed out by Andreopoulos (*ibid.*) that the streamlines of the jet in the x-z plane start to bend well within the hole passage. Figure 6-36 shows the vorticity, ω_z, in the horizontal plane very near the plate surface. The vorticity generated in the z'-direction clearly follows the round contour of the hole, becoming greater near the trailing edge. This increase in ω_z toward the trailing edge can be attributed to the increased jet velocity near the trailing edge, which increases the tilting of the jet side-wall vorticity and aligns more of the jet vorticity in the z-direction. As pointed out in §6.1.1 in connection with the previous observation make by Fearn and Weston (1975), the magnitude of the vorticity also increases with jet velocity.
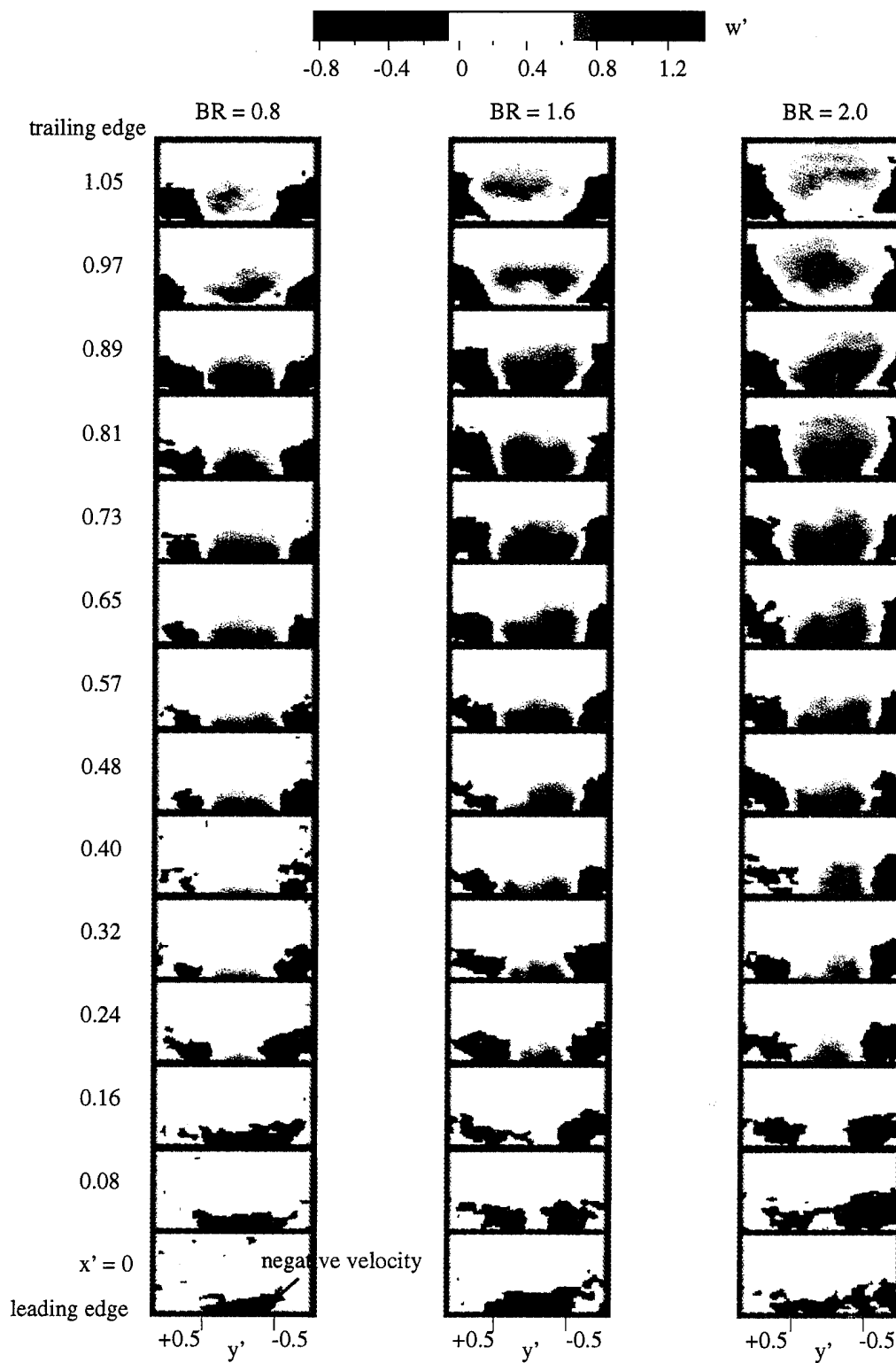
Figure 6-33: Hole 3: w'-Velocity Plots, BR = 0.8, 1.6, and 2.0

smoke entering hole
at leading edge

D
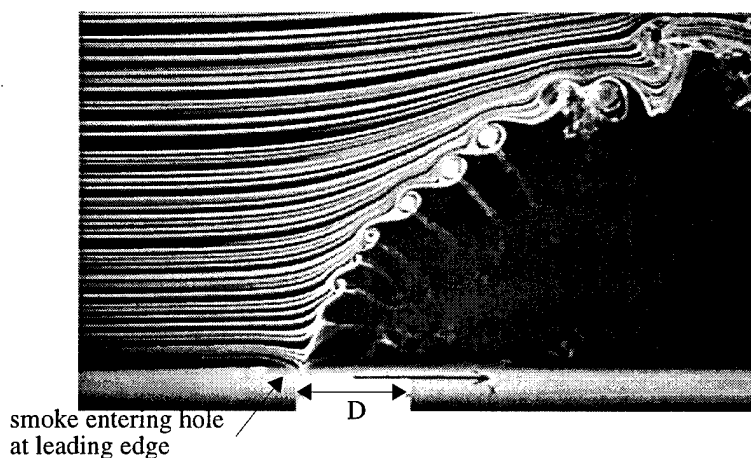
Figure 6-34: Flow Visualization Results, Fric (1994, figure 2), BR = 2.0

BR = 1.0

BR = 1.6

negative velocity
-no stagnation point-
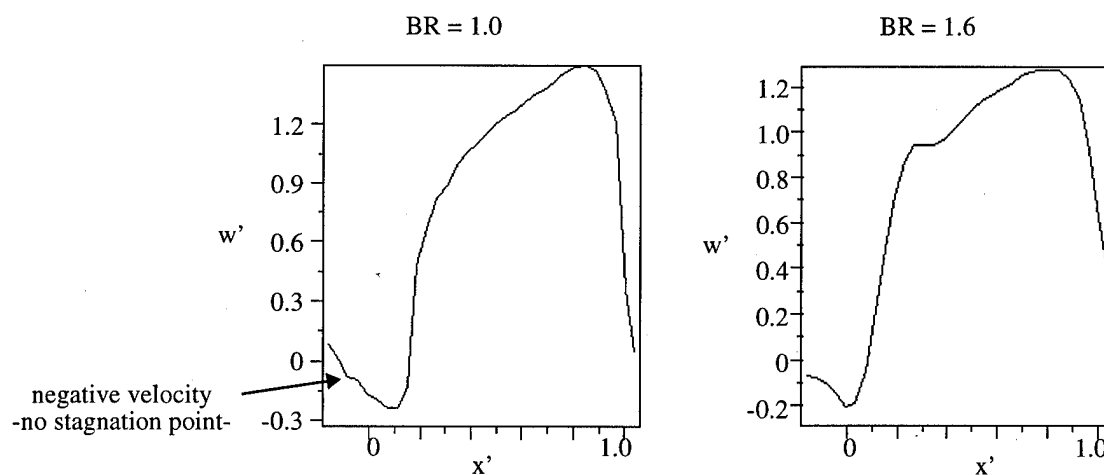
Figure 6-35: Hole 3: w'-Velocity Profile Along the Hole Centerline

6.4.3 Vorticity Realignment by Warping of Leading Edge Vortex Sheet

The side spillage and sweeping of the leading edge vorticity in the downstream direction is evidenced in figure 6-37 by the appearance of counter-rotating lobes on each side of the hole. These lobes appear in the laser sheet oriented parallel to the surface. All flow visualization pictures were taken for the laser sheet positioned at z' = 0.26. As the blowing ratio decreases, the jet is bent more toward the downstream, causing the leading edge vorticity
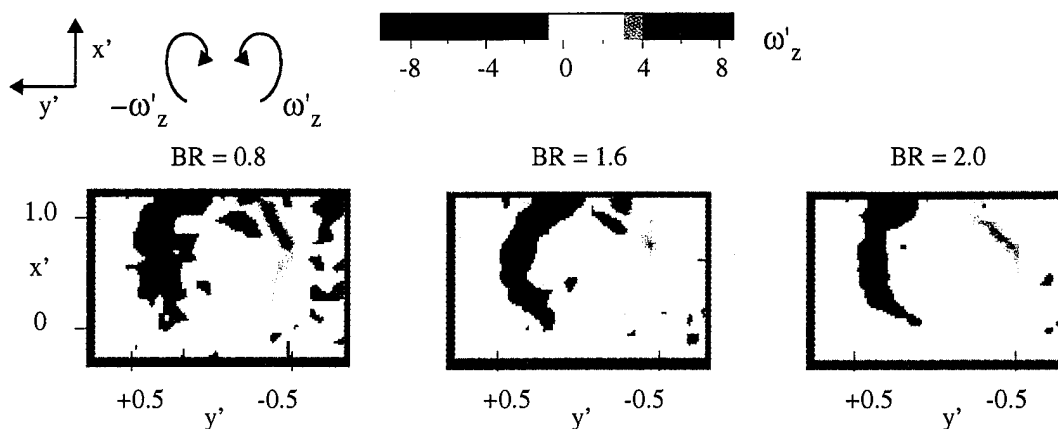
Figure 6-36: Hole 3: z-Vorticity Profiles at z' = 0, BR = 0.8, 1.6, and 2.0

to be convected further downstream for the same z-location. The result is that at BR = 0.8, counter-rotating vortex structures along the sides of the jet appear downstream, as compared to the higher blowing ratios, where these same vortex structures are seen closer to the leading edge.
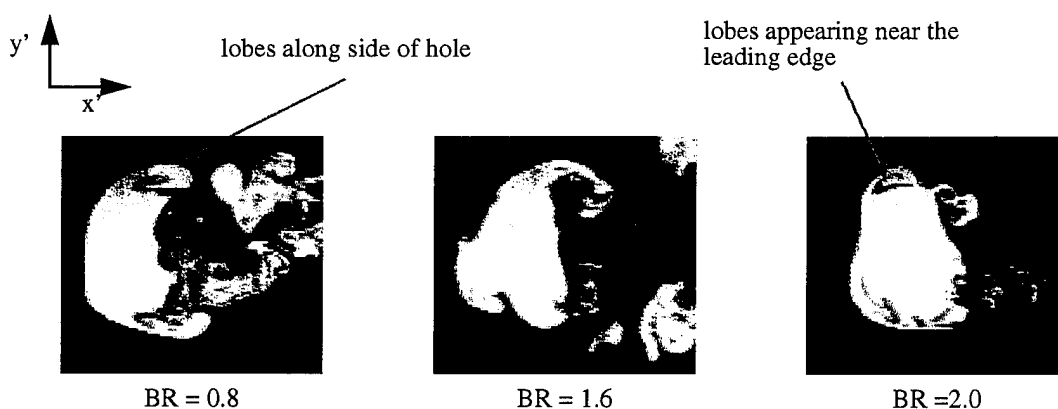
Figure 6-37: Hole 3: Flow Visualization of Leading Edge Vorticity, z' = 0.26

The warping of the leading edge vortex sheet also results in the formation of streamwise vorticity, ω_x, as discussed in §4.1. The u'-velocity profile at z' = 0.32 is shown in figure 6-38 for the three blowing ratios. The sign of the velocity derivative, $\frac{du}{dy}$, is the same

as the one for the square hole, and therefore, the vorticity generated has the same sense of rotation as the kidney-vortices. Therefore, the intermittent passing of the leading edge vorticity can be seen as a second kidney-vortex riding on top of the steady structures, as seen in figure 6-32.
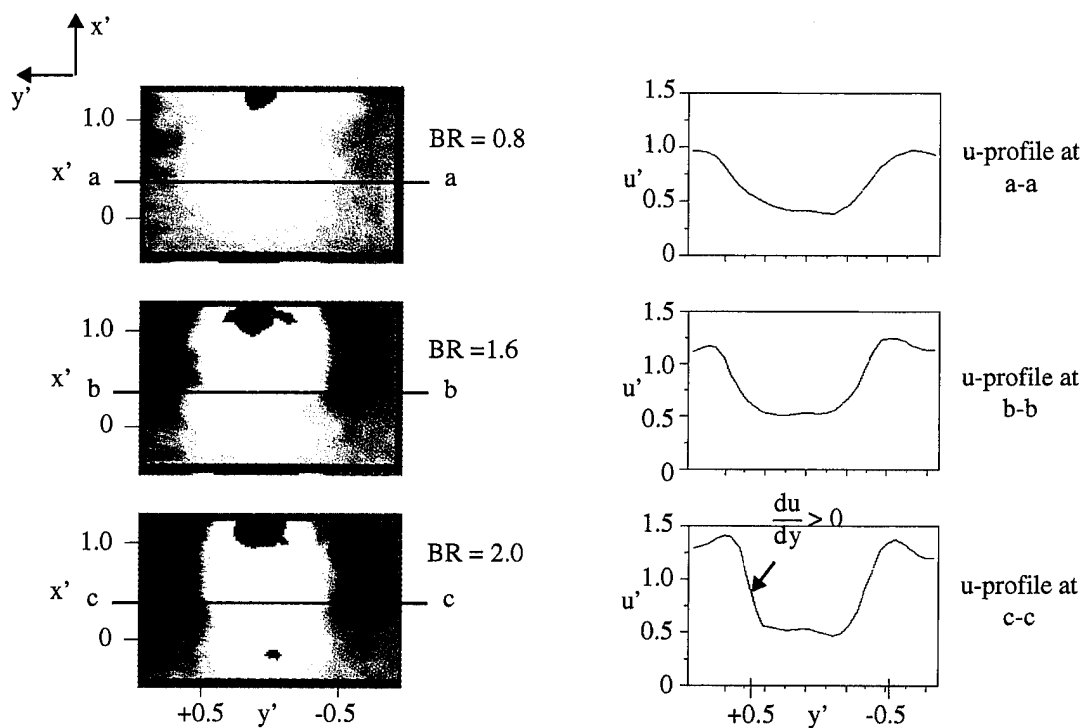
Figure 6-38: Hole 3: u'-velocity Profiles at z' = 0.32, BR = 0.8, 1.6, and 2.0

6.4.4 Tilting of Hole Trailing Edge Vorticity

The u'-velocity distribution of figure 6-39 shows again the presence of the reverse flow at the trailing edge, which was observed by many studies on a round hole. The presence of the reverse flow at the leading edge may also be found in figure 5 of Andreopoulos (1981). The tilting of the trailing edge vorticity results two counterrotating vortices near the downstream edge of the hole (top of figure 6-39). The induced velocity from these vortices is a major contributor to the reverse flow downstream of the jet.

The flowfield in this downstream region is very complicated. As mentioned in §6.4.1, the PIV results at the trailing edge show a 'negative' vortex pair in y-z plane (figure 6-32:

BR =1.6

counter-
rotating
vortex pair

$-\omega'_z$ ω'_z

BR =2.0

z' = 0.26

z' = 0.26

u'

-0.6   0   0.6   1.2   1.8

0.71

0.59

0.52

0.40

0.32

0.19

0.12

z' = 0

x'

y'

reverse flow due
to horseshoe vortex

reverse flow

trailing edge

leading edge

+0.5   -0.5
y'

+0.5   -0.5
y'
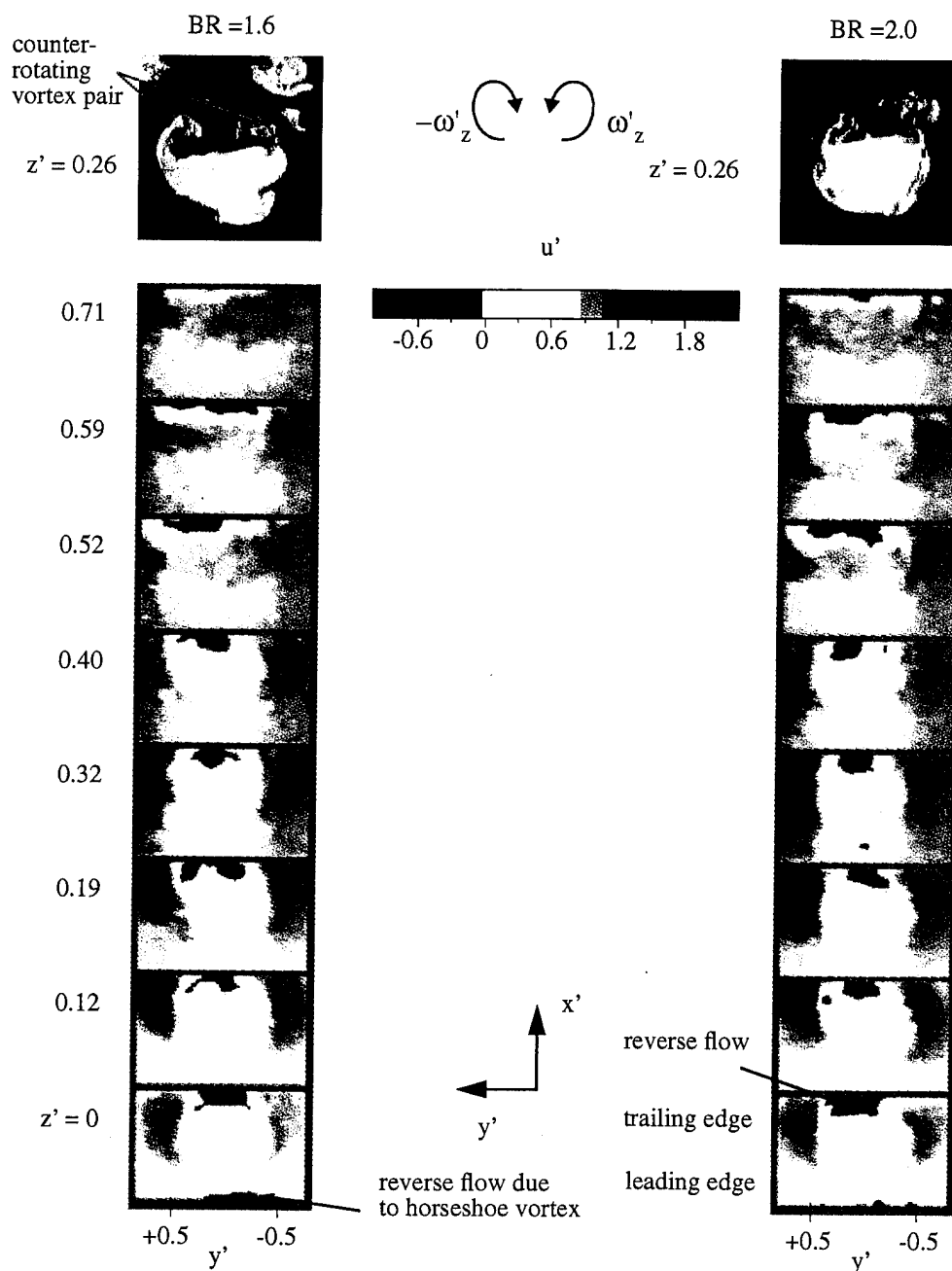
Figure 6-39: Flow Visualization and PIV u'-velocity Profiles, BR = 1.6 and 2.0

e.g. x' = 0.97, BR = 1.6). As shown again in figure 6-40 for a blowing ratio of 1.6, the position of the 'negative' pair is at the surface of the plate, underneath the jet.

The vector plot, corresponding to the vorticity plot, shows the distinct steady kidney-vortices at the sides of the jet. Along the centerline, there is a region of low vertical velocity fluid near the plate, which corresponds to the 'negative' pair. Though not obvious in the vector plot, the processed vorticity plot on the left, reveals the presence of the 'negative' pair, which tends to suppress the jet's vertical velocity at the downstream edge of the hole. The 'negative' pair itself is caused by the following action of the strong reverse flow of figure 6-39: the reverse flow at the trailing edge acts like a crossflow to the jet at the

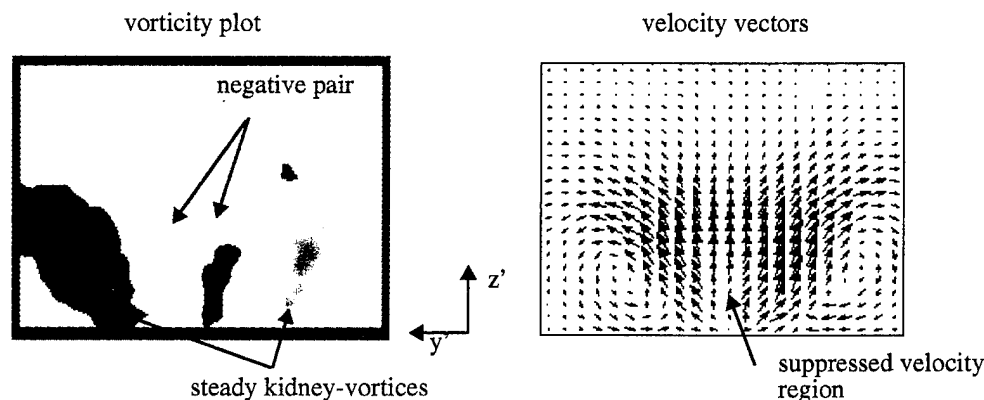vorticity plot   velocity vectors

Figure 6-40: x-Vorticity Plot and Velocity Vector Plot at x' = 0.97, BR = 1.6

leading edge. Just as the crossflow causes the warping of the leading edge vortex sheet, the reverse flow at the downstream edge of the hole can have the same effect on the trailing edge vortex sheet (figure 6-41) (The presence of the 'negative' pair underneath the jet and at the surface of the plate suggests that the vortex filament at the trailing edge is being realigned while it is still within the hole.). This may also explain the lack of a 'negative' pair for the lower blowing ratio of 0.8, since the magnitude of the vorticity inducing the reverse flow is proportional to the jet velocity. If so, increasing the blowing ratio should promote the formation of a 'negative' pair, as is, in fact, the case for a blowing ratio of 2.0 (figure 6-32).

The 'negative' pair for a round hole was previously reported by Moussa, Trischka and Eskinazi (1977), where a 3D hot wire was used to map the crossflow jet issuing from a round pipe. Their figure 17, which displays contours of ω_x in the y-z plane, shows a small
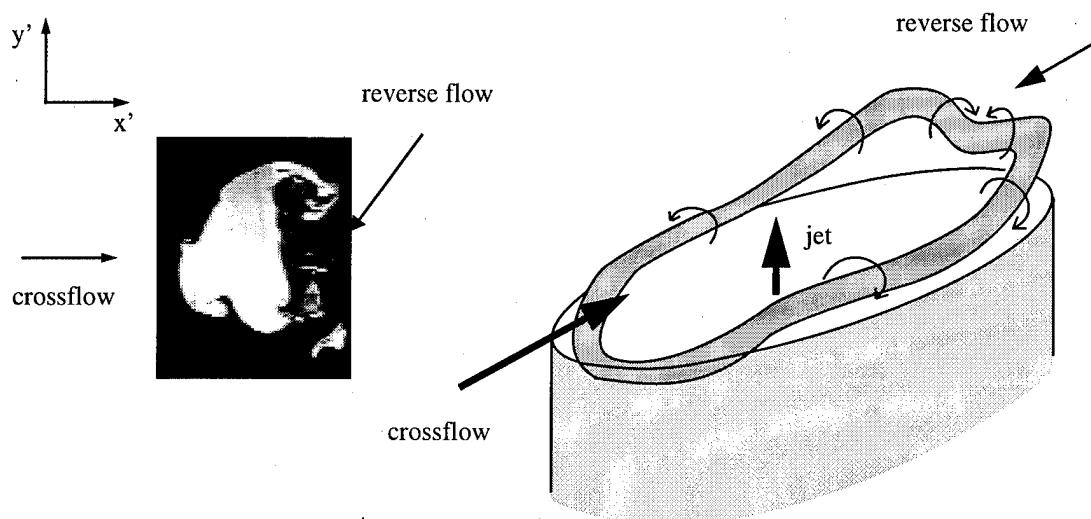
Figure 6-41: Warping of the Trailing Edge Vortex Sheet due to Reverse Flow

'negative' pair above the 'positive' pair at positions of x' =0.5 (fig. 17a), x' = 0.75 (fig. 17b), and x' = 1.5 (fig. 17d). However, at the trailing edge of the hole, x' = 1.0 (fig. 17c), there is no 'negative' pair, contrary to our data.

Instead of the present mechanism based on the warping of the trailing edge boundary layer, the explanation offered by Moussa, *et al.* is "*...the cross-stream develops an induced negative vorticity in all three directions as it spills over the jet boundary. When one takes a very large contour around the entire flow such that the legs of the contours are in irrotational flow, we can deduce that each bound vortex* (i.e., the kidney-vortices in the present terminology) *must generate in the cross-stream an equal and opposite rotation with equal circulation. pg. 76*" This explanation appears to be at odds with the fact that no new vorticity can be generated within the flow. With the exception of Moussa *et.al*, no other subsequent studies on the round hole, or any other shaped hole, has reported on the 'negative' pair.

Of the holes discussed thus far, the round hole is the only one that shows a distinct 'negative' pair at the trailing edge of the hole. It is, however, the harbinger of the 'negative' pair at the trailing edges of lower aspect ratio holes, to be discussed subsequently. Therefore, hole geometry plays an important part in the realignment of the trailing edge vorticity.

As discussed in §3.2, the geometry of the hole determines the lateral spacing of the steady kidney-vortices. As the geometry forces the vortices closer together, the induced velocity between them becomes greater and more concentrated at the centerline. This is where the effect of hole curvature plays a role. For the case of the square hole, the sides of the hole are closer than the sides of the round hole at its widest point; however, because of the round hole's side-wall curvature, the kidney-vortices are brought closer together as the side-wall vorticity begins to lift up near the trailing edge.

6.5 Low Aspect Ratio Rectangle (Hole 1): $\longrightarrow$ ☐

The near field character of a jet from a rectangular hole is dramatically altered by changing its orientation relative to the crossflow. The hole is identical to the one used as the high aspect ratio rectangle (hole 6) in §6.2, but rotated 90°. In §4, a comparison between the low and high aspect ratio rectangles already demonstrated that orientation alone is responsible for the superior attachment characteristics of the high aspect ratio rectangle. The reason proposed in §6.2 for the latter is, that in addition to the greater physical separation of the steady kidney vortices formed by the side-wall vorticity, the potential annihilation of kidney-vortices through the formation of a 'negative' vortex pair at the leading edge of jet. The flow field dissected for the present low aspect ratio rectangle shows significant departure from this.

6.5.1 'Steady' Kidney-Vortices and 'Negative' Vortex Pair

The two general flow characteristics of the low aspect ratio rectangle are the steady kidney-vortices that rise rapidly off the surface along the x-direction, and the appearance of a 'negative' vortex pair now present near the trailing edge of the hole, similar to that seen for the round hole. Figure 6-42 shows the vorticity aligned in the x-direction, ω_x, for three blowing ratios (averaged from three instantaneous files). Near the trailing edge, the area between the vortex pairs is more chaotic than that seen for the previous holes. Despite this, there is a consistent appearance of 'negative' vortex pair along the centerline, close to the surface of the plate. Even for the lowest blowing ratio, a weak 'negative' pair appears just
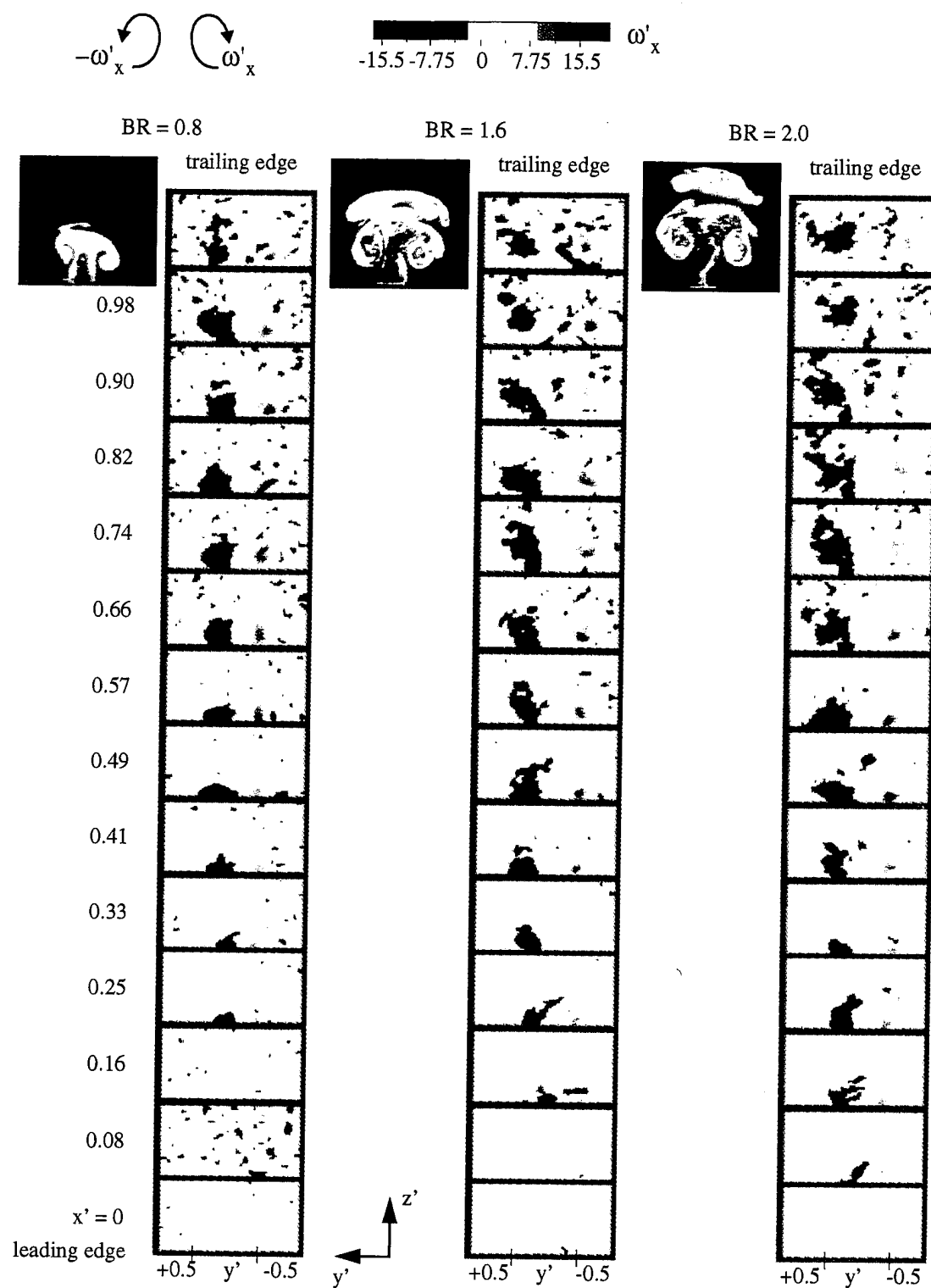
Figure 6-42: Hole 1: Flow Visualization and PIV Vorticity Plots, BR = 0.8, 1.6, and 2.0

aft of the downstream edge of the hole, x' = 1.07. The corresponding flow visualization pictures, taken at x' = 1.0, show the significant lift-off of the jet at the trailing edge. The unsteady kidney-vortices are also very prominent and perhaps one of the reasons for the chaotic appearance of the vorticity plots.

The w'-velocity plots are given in figure 6-43. At the leading edge, the vertical velocity is again negative as a result of the jet's interaction with the crossflow. Along the sides of the jet, the increased lift-off of the kidney-vortices creates large regions of negative velocity. All along the hole, the negative velocity region extends far into the crossflow, which promotes entrainment of crossflow fluid toward the surface (compare figure 6-17 for high aspect ratio rectangle). For applications where the desired function of the jet is to separate the surface from the crossflow, this entrainment is highly undesirable. Near the trailing edge, in the areas where the 'negative' vortex pair is seen, the vertical velocity profile shows low velocity regions near the surface and centerline of the jet. This is similar to what was seen at the trailing edge of the round hole, and will be discussed further in §6.5.4.

6.5.2 Vorticity Realignment by Tilting of Side-Wall Vortex Sheet

The vertical velocity profiles along the edge of the hole are shown in figure 6-44 for blowing ratios of 0.8 and 1.6. The velocity distribution along the centerline is again skewed in a shape similar to that of the high aspect ratio hole. Near the edge, however, the saddle profile, which is first detected for a square hole, but absent in the high aspect ratio hole, reappears. Its presence along the longer side of the low aspect ratio hole is to be expected due to the additive effect of the leading and trailing edge boundary layers near the corners of the hole. This suggests, then, that even for a free jet (BR → ∞) emanating from a rectangular slot, the saddle-shaped velocity distribution should be present along the longer side, but not along the shorter. This is indeed found in figure 12 of Trentacoste and Sforza (1967).

The velocity gradient along the side of the jet indicates the tilting of the side-wall vorticity. Vorticity plots, in the plane just off of the plate (z' = 0), show vorticity concentrations, ω_z, along the sides of the jet due to the realignment of the side-wall vorticity toward
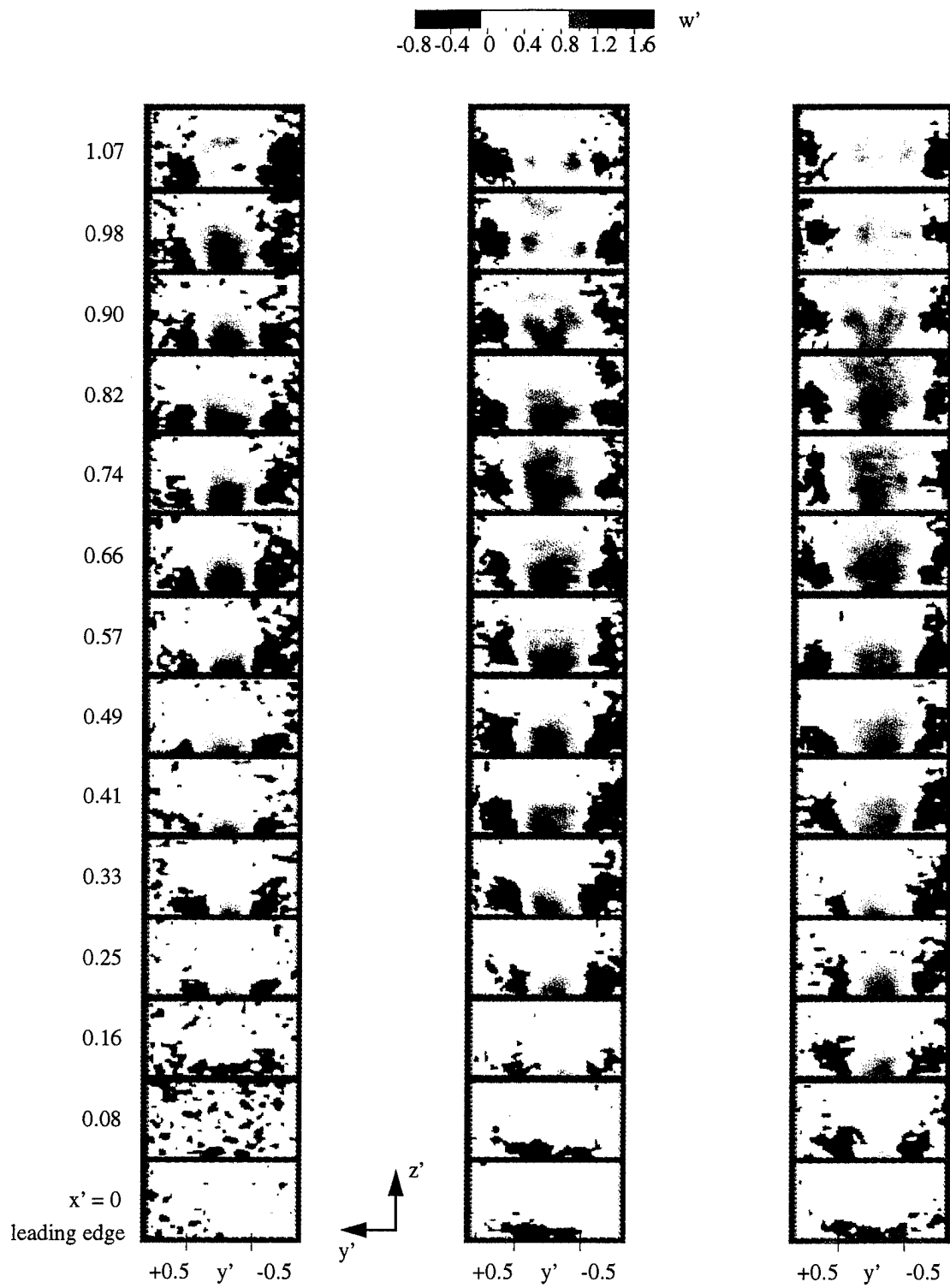
Figure 6-43: Hole 1: w'-Velocity Plots, BR = 0.8, 1.6 and 2.0

the z-direction. The z-component of vorticity appears just downstream of the leading edge and runs along the sides of the hole.

BR = 0.8   BR =1.6
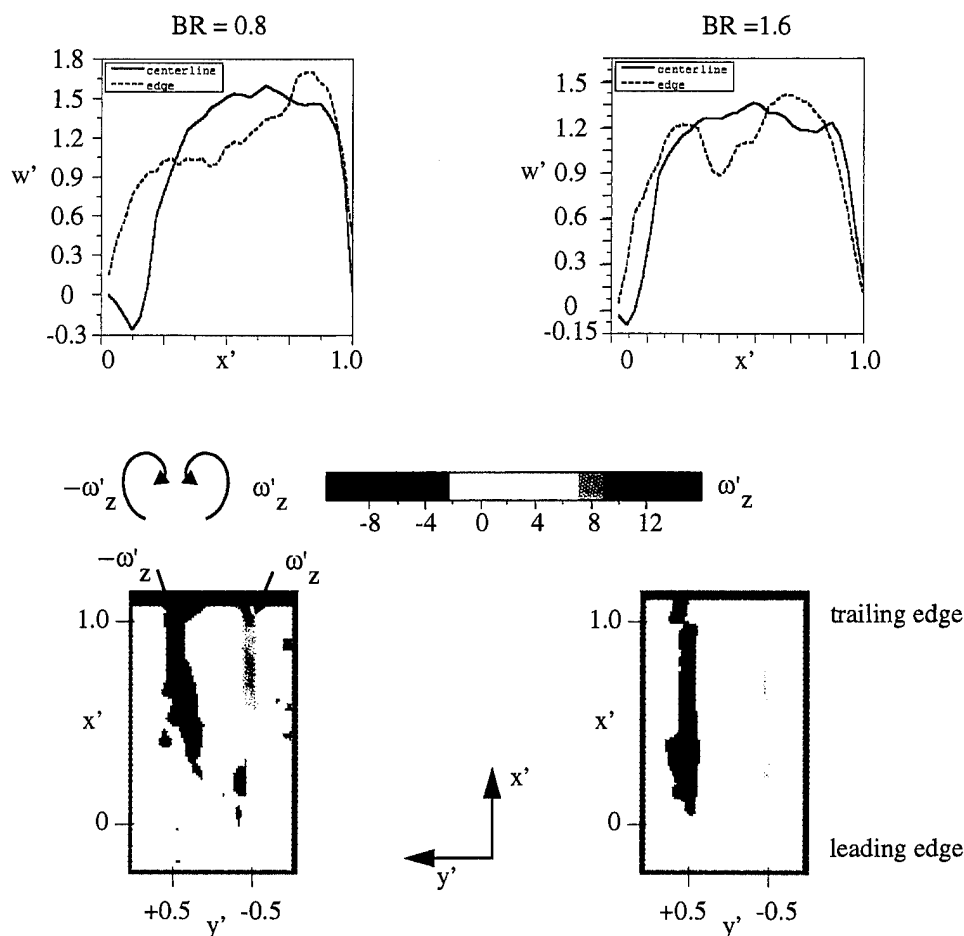
Figure 6-44: Hole 1: Side-wall Velocity Profiles and Vertical Vorticity Plots at z' = 0.12, BR = 0.8 and 1.6

6.5.3 Vorticity Realignment by Warping of Leading Edge Vortex Sheet

The large separation distance between the leading and trailing edges of hole 1, enables the clear distinction of the vorticities originating from them. As shown previously in figure 5-7, for the low aspect ratio rectangle, the vortical structures formed at the corners of the leading edge are the result of the lateral turning of the leading edge boundary layer towards the side. This same counterrotating 'positive' vortex pair is shown again in figure

6-45 for the low aspect ratio rectangle.

crossflow

BR = 0.8   BR =1.6   BR = 2.0
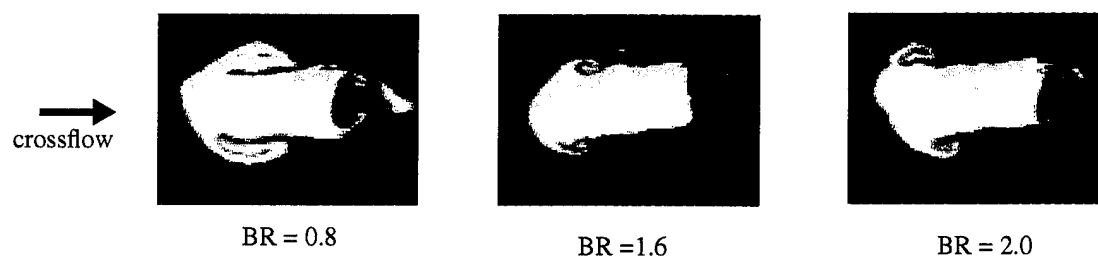
Figure 6-45: Hole 1: Parallel Laser Sheet Cuts at z' = 0.26

As far as the central portion of the leading edge boundary layer is concerned, the streamwise velocity profile shown in figure 6-46, for z' = 0.32, indicates that the leading edge vortex sheet will be warped about its centerline, which induces vorticity in the x-direction, ω_x. The lateral variation in u, $\dfrac{du}{dy}$, is such that this realigned vorticity will be similar to the one for the square and have the same rotational sense as the kidney-vortices.
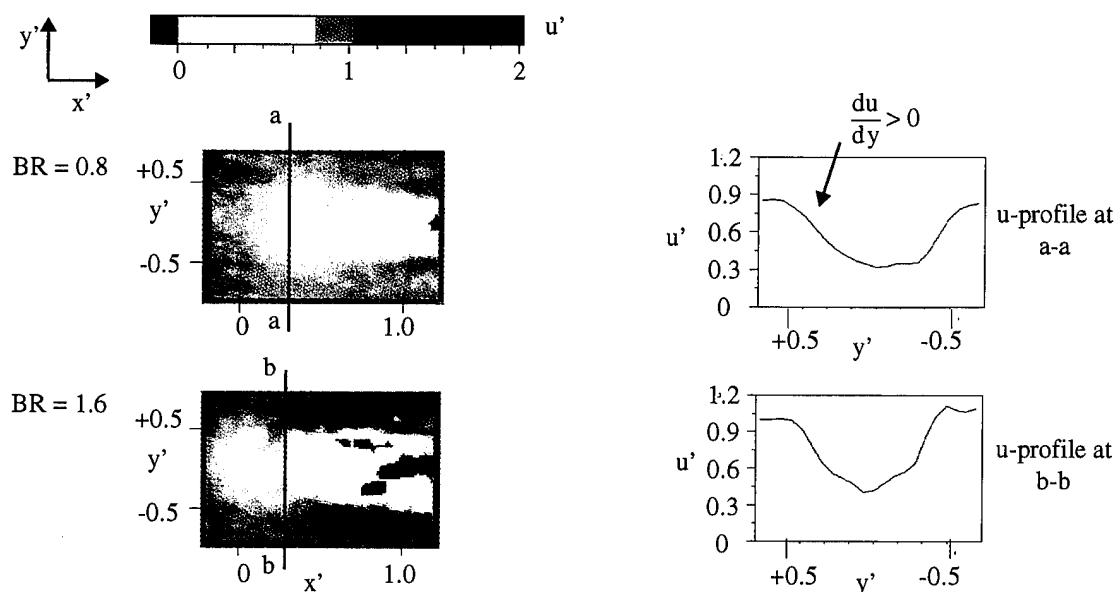
Figure 6-46: u'-Velocity Profiles, z' = 0.32, BR = 0.8 and 1.6

As the leading edge vortex sheet rolls up away from the exit and is convected downstream, the intermittent passage of this leading edge vorticity will appear in the y-z plane as an unsteady vortex pair riding on top of the jet, rotating in the same direction as the kidney-vortices (figure 6-47).
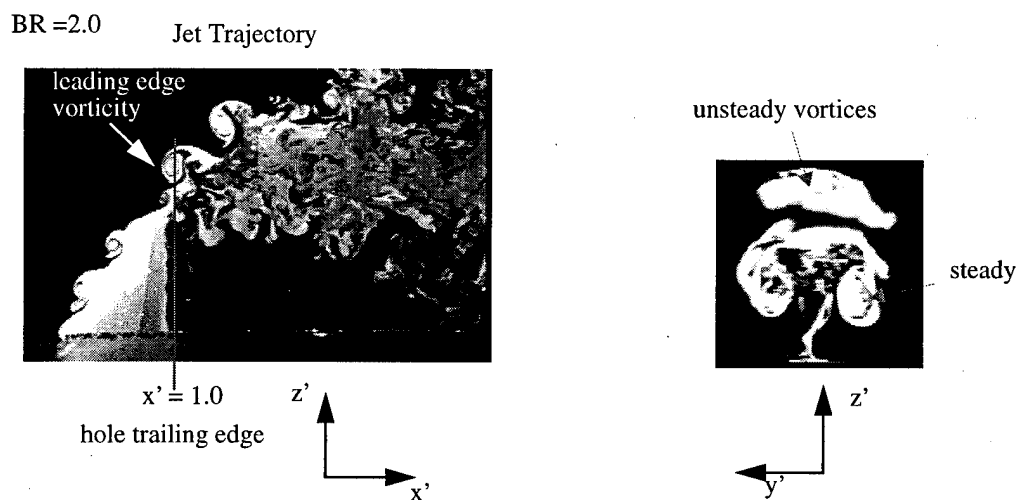
Figure 6-47: Hole 1: Shedding of Leading Edge Vorticity Resulting in the Unsteady Kidney-Vortex Pair

When the u'-velocity distribution of figure 6-46 is compared with that of the high aspect ratio rectangle (figure 6-20), a significant difference between them is observed: while for the present low aspect ratio rectangle, there is a velocity defect at the centerline, for the high aspect ratio rectangle, a central peak is present instead. The reason is considered to be as follows. The low aspect ratio rectangle, which has a longer streamwise dimension with the bulk central core of its jet unexposed to the crossflow, may resist the crossflow more like a bluff solid body. The crossflow is thus diverted sideways, which results in a velocity defect at its center. On the other hand, a high aspect ratio rectangle having considerably less central core is more susceptible to the streamwise penetration of the crossflow into the jet, which leads to the larger u-velocity at its center.

6.5.4 Tilting of Hole Trailing Edge Vorticity

Near the trailing edge of the hole, the vertical velocity, w, changes drastically in the lateral, y, direction (figure 6-43). As shown in figure 6-48 for a blowing ratio of 1.6, the velocity profile near the hole exit changes from a bell shaped profile at x' = 0.90, to one which has a large velocity deficit in the center at x' = 0.98. The reason for the velocity deficit is again the strong reverse flow at the downstream side of the hole.
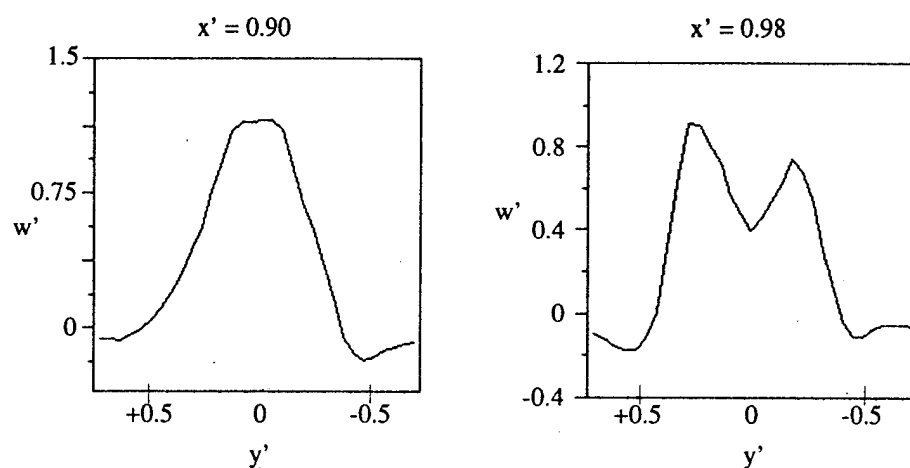
Figure 6-48: Hole 1: w'-Velocity Profiles at z' = 0.36, BR = 1.6, x' = 0.90 and 0.98

Compared to the previous holes, the reverse flow region for the low aspect ratio rectangle is much more localized and penetrates far upstream of the trailing edge. Figure 6-49 shows the streamwise velocity plots on planes parallel to the plate and compares it with all the hole geometries discussed thus far (BR = 1.6). Note that while for the present low aspect ratio rectangle, the crossflow direction is drawn to be horizontal, for the others it is vertically upward. For the previous four holes, the reverse flow region extends across the span of the hole, never penetrating upstream of the hole trailing edge. In contrast to this is the deep upstream penetration of the reverse flow for hole 1.

The penetration is due to the induced velocity between the vortex pair at the trailing edge of the hole. Near the trailing edge, two distinct vortex structures are formed at the
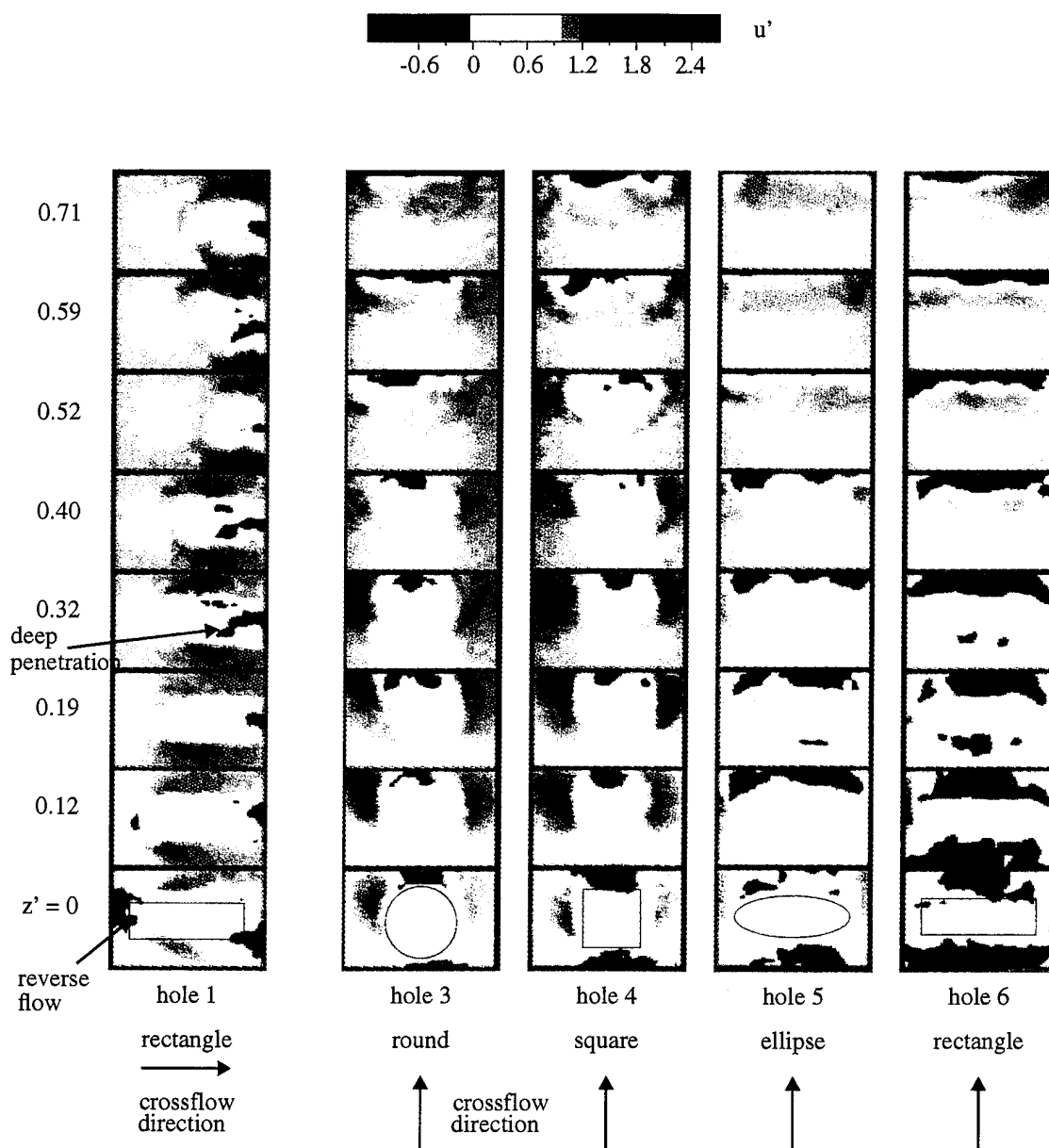
Figure 6-49: Parallel Cuts: u'-Velocity Plots, BR = 1.6, Holes: 1,3,4,5 and 6

corners of the hole with a large vorticity component aligned in the z-direction (figure 6-50). These trailing edge vortices were tracked using two traces of fluorescein dye injected into the downstream jet boundary layer 22 mm inside the hole passage. The dye appears to be trapped in the vortex cores formed at the corners of the hole. Laser sheets at different z-locations show that these trailing edge vortex structures appearing on the underside of the jet remain well defined far off the plate surface.
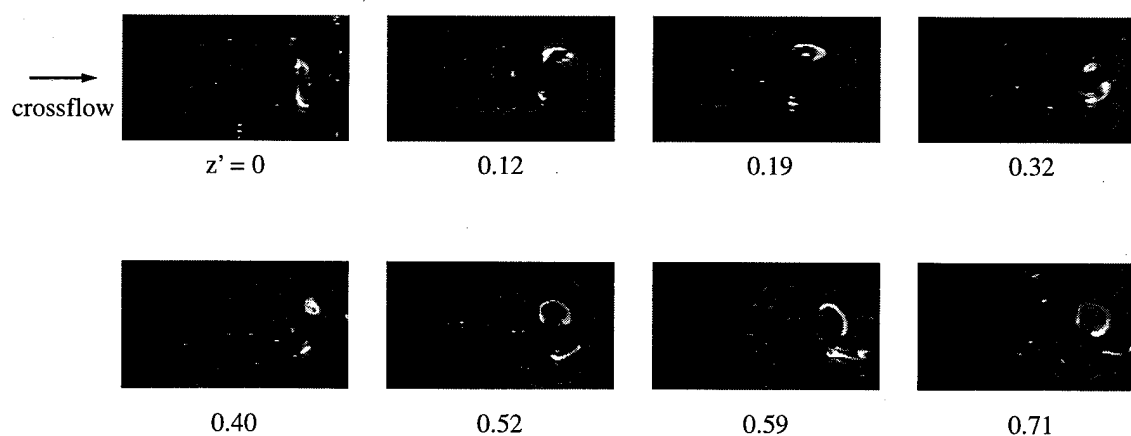
Figure 6-50: Hole 1a: Laser Sheet Cuts in z-Direction, BR = 1.14

As in the case of round hole, the reverse flow is thought to be the cause of the 'negative' vortex pair near the trailing edge. The influence of this trailing edge vortex pair is not limited to the downstream side of the jet. As shown in figure 6-51, the action of these corner vortices draws the crossflow boundary layer fluid that is passing along side of the hole into the underside of the jet. In essence, the vorticity associated with the crossflow boundary layer is being pumped into the jet, which potentially enhances the strength of the kidney-vortices.

BR = 1.14, z' = 0
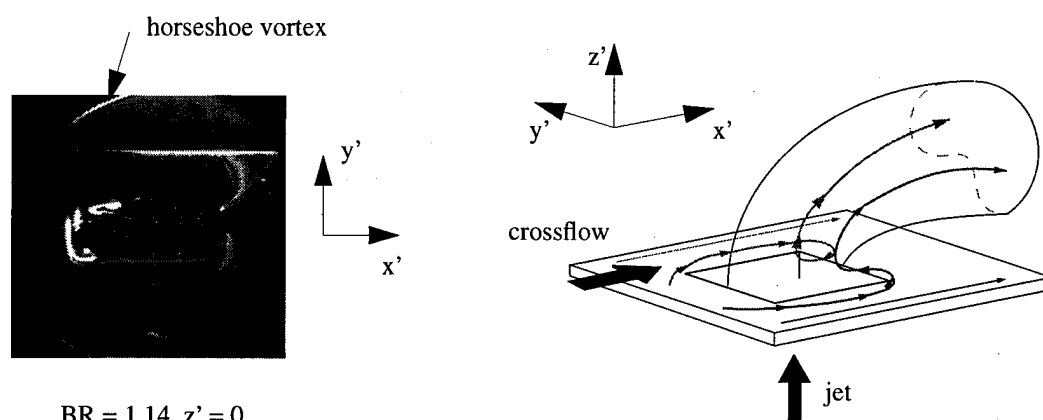
Figure 6-51: Hole 1a: Entry of Crossflow Boundary Layer Vorticity into Jet

6.6 Low Aspect Ratio Ellipse (Hole 2): ⟶ ◯

The low aspect ratio ellipse, hole 2, gives further insight into the effect of hole curvature on the jet characteristics. For the most part, the jet is similar in nature to that for the low aspect ratio rectangle. The primary difference is in the area at the downstream edge of the hole. Here the curvature does not provide the distinct separation distance between the trailing edge vortices, reducing the upstream penetration of the reverse flow.

6.6.1 'Steady' Kidney-Vortices and 'Negative' Vortex Pair

The steady kidney-vortices in figure 6-52 rise rapidly off the plate surface from the leading to trailing edge of the hole. Here, the vorticity plots are obtained from the instantaneous velocity data and show the frequent appearance of a separate unsteady vortex pair. On the downstream side of the hole, near the plate surface, an additional vortex pair is also visible similar to those seen for the low aspect ratio rectangle.

The corresponding vertical velocity plots in figure 6-53 show the large areas of negative velocity along the sides of the jet, with the highest downward velocity occurring well off the plate.
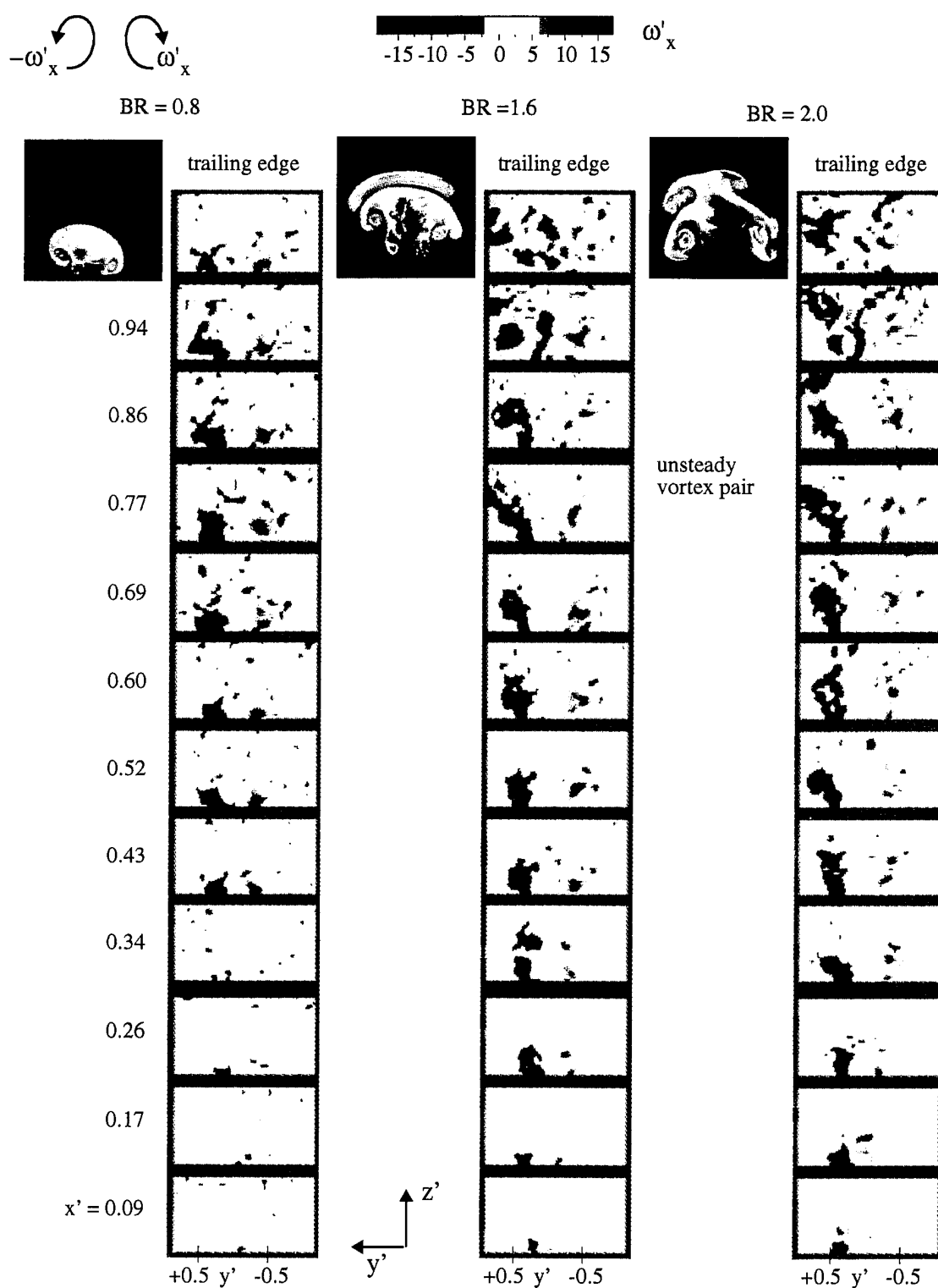
Figure 6-52: Hole2: Flow Visualization and PIV Vorticity Plots, BR = 0.8, 1.6, and 2.0
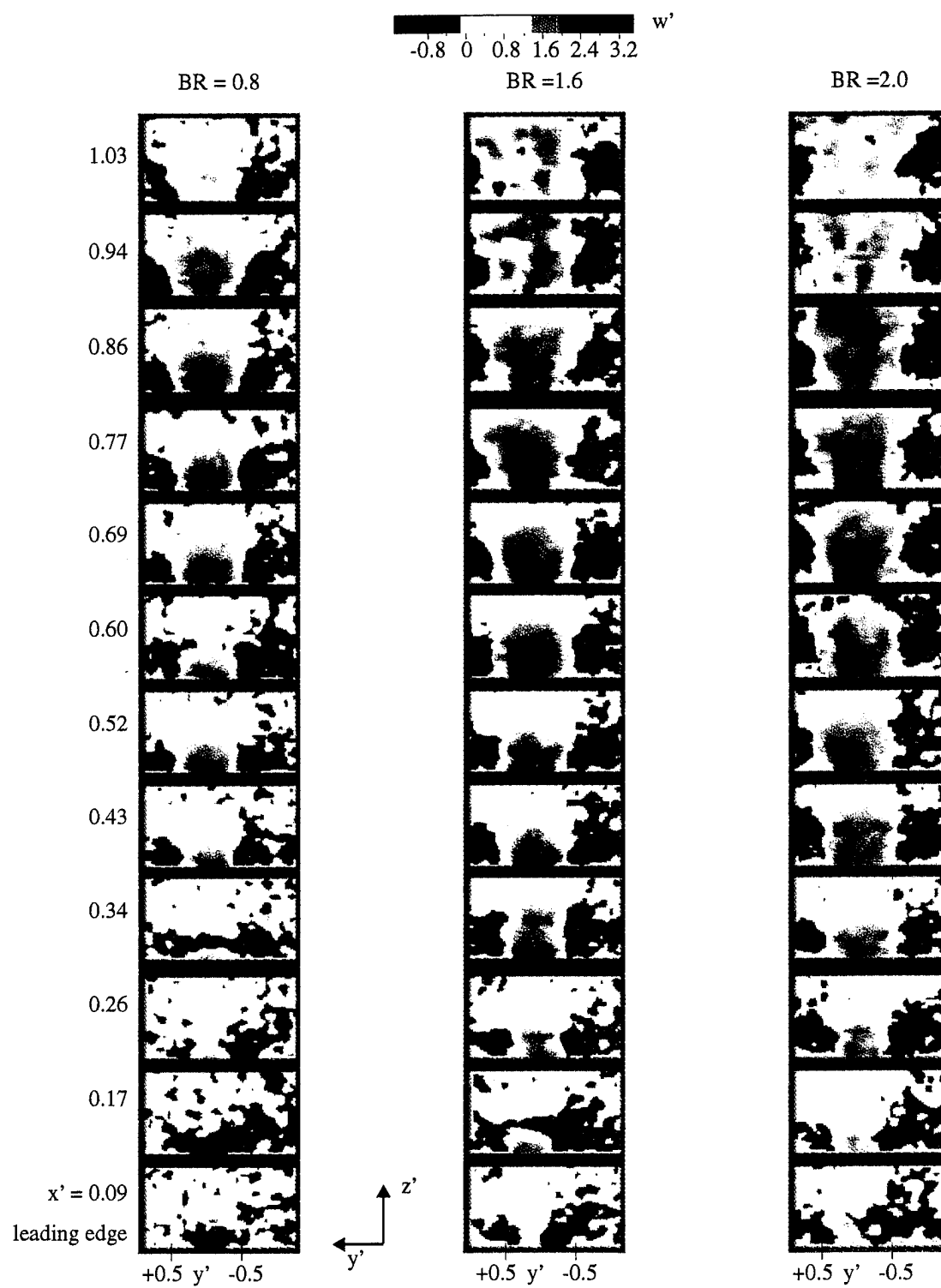
Figure 6-53: Hole 2: w'-Velocity Plots, BR = 0.8, 1.6, and 2.0

6.6.2 Vortex Realignment by Tilting of Side-Wall Vortex Sheet

Evidence for the tilting of the side-wall vortex sheet is seen in the vorticity plots for a blowing ratio of 1.6 (figure 6-54: note, the orientation of the x-y axes is different from figure 6-26 corresponding to the high aspect ratio ellipse). At the surface of the plate, the appearance of perpendicular vorticity, ω_z, happens very near the leading edge and increases in strength toward the trailing edge. (At the trailing edge, a weak vortex pair is evident that has the opposite sign of vorticity relative to the upward tilting of the side-wall boundary layer. This pair may be due to the vorticity realigned in the z-direction by the warping of the trailing edge boundary layer near the plate surface. This vortex pair is only seen near the plate (z' < 0.19)).

6.6.3 Vorticity Realignment by Warping of Leading Edge Vortex Sheet

The hole curvature makes it impossible to distinguish completely between the leading edge and side-wall vortex sheet. As shown in figure 6-55, the leading edge vorticity is turned laterally to form vortex structures along the sides of the jet. These structures do not always appear at the same place, as in the case for the rectangular hole (figure 6-45), but appear to form at various points along the sides of the hole. This unsteady pair, which has the same rotational sense as the kidney-vortices, is clearly seen in the flow visualization pictures in figure 6-52.

6.6.4 Tilting of Hole Trailing Edge Vorticity

As mentioned in the introductory remarks to §6.6, the curvature of the low aspect ratio ellipse affects the character of the reverse flow region on the downstream side of the jet. Figure 6-56 shows the streamwise velocity plots for both the low aspect ratio ellipse and rectangle for eight different z-locations. The upstream penetration of the reverse flow for the ellipse is markedly less than that for the low aspect ratio rectangle. The proposed explanation is illustrated in figure 6-57. The well-defined corners of the rectangle set the location at which the trailing edge vortex sheet lifts up. The fixed region between the vortices allows for the penetration of downstream fluid into the back side of the jet. For the ellipse, however, the point at which the trailing edge vorticity is lifted can easily move
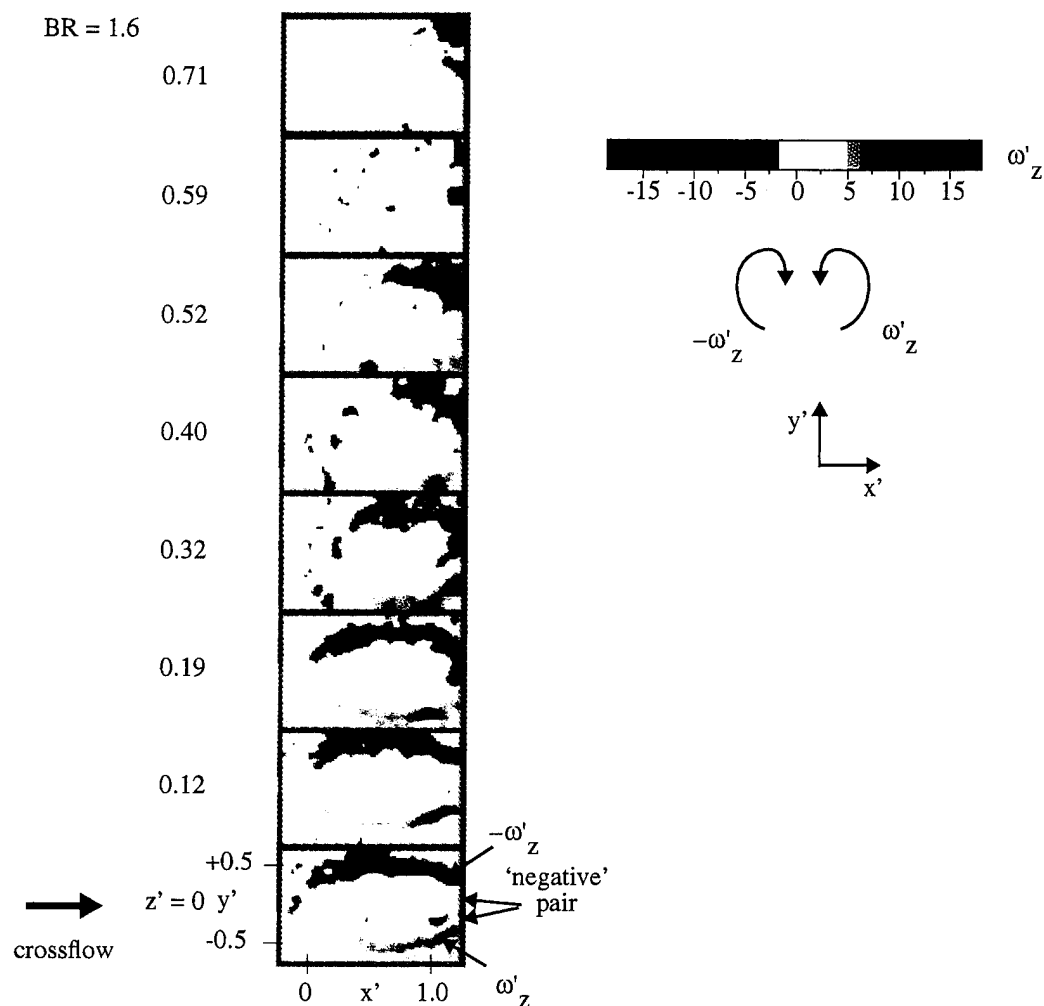
Figure 6-54: Hole 2: Vorticity Plots in Planes Parallel to the Plate, BR = 1.6
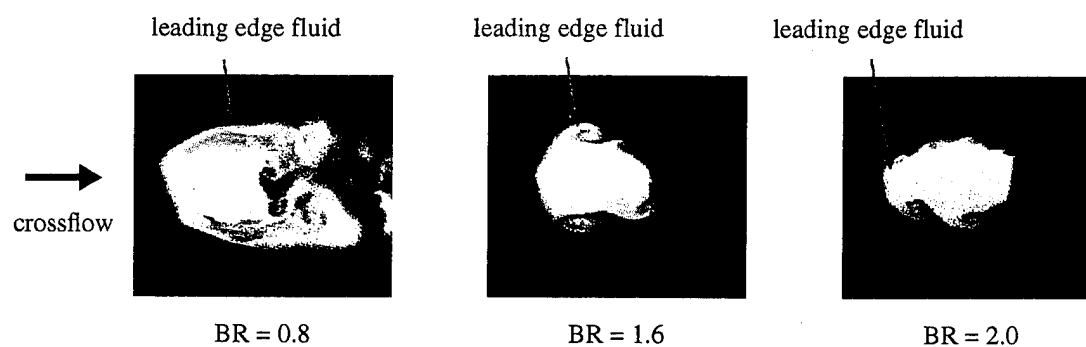
Figure 6-55: Hole 2: Laser Sheets Parallel to Plate at z' = 0.26
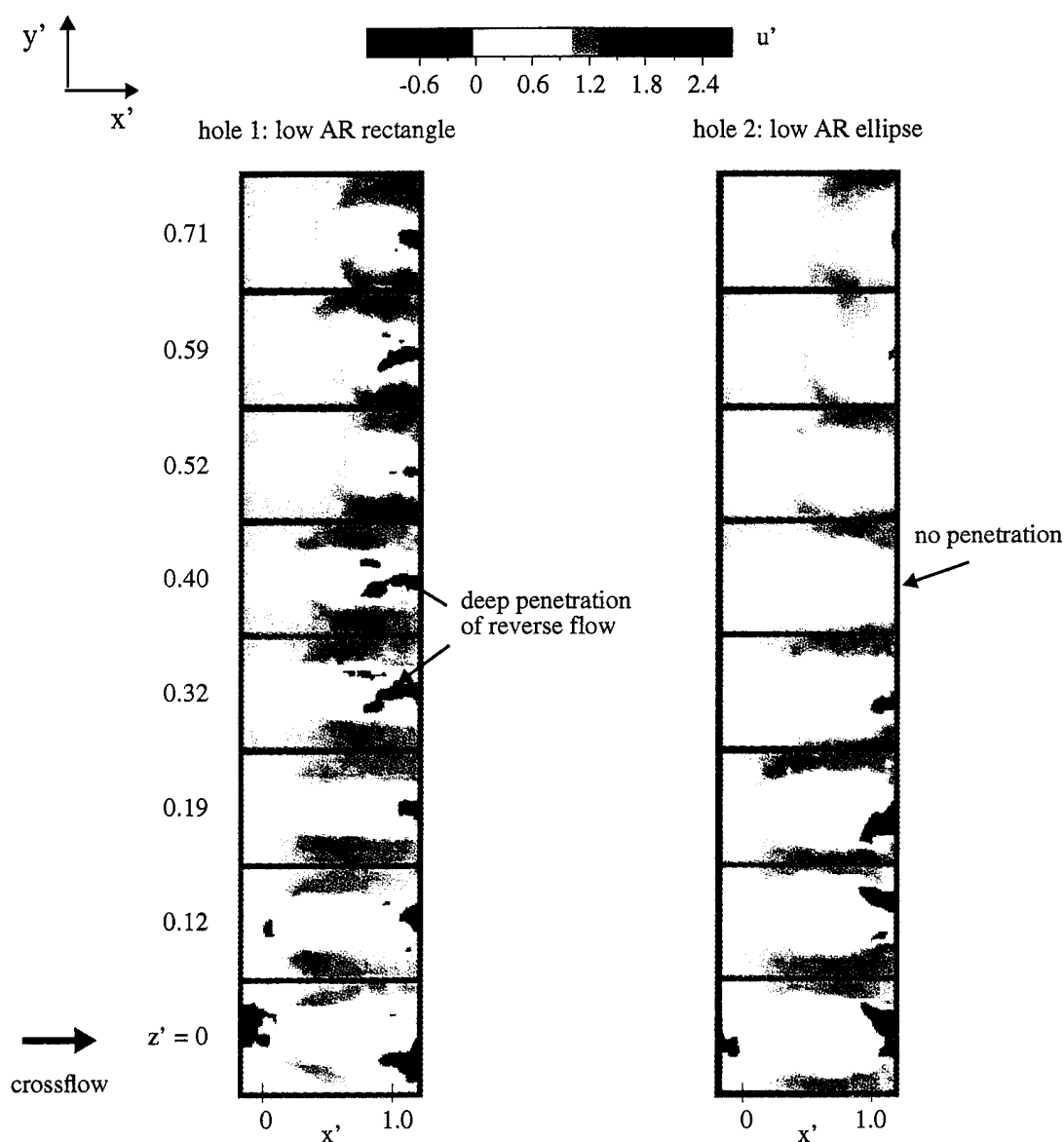
Figure 6-56: Holes 1 and 2: Comparison of Reverse Flow Region, BR = 1.6

along the back part of the hole and does not appear, in general, to be symmetric with respect to the hole centerline. The result is a flow pattern behind the hole that sweeps the fluid from side to side, which minimizes the upstream penetration. The vector plots supporting this illustration are given in figure 6-58 for both the low aspect ratio rectangle and ellipse.
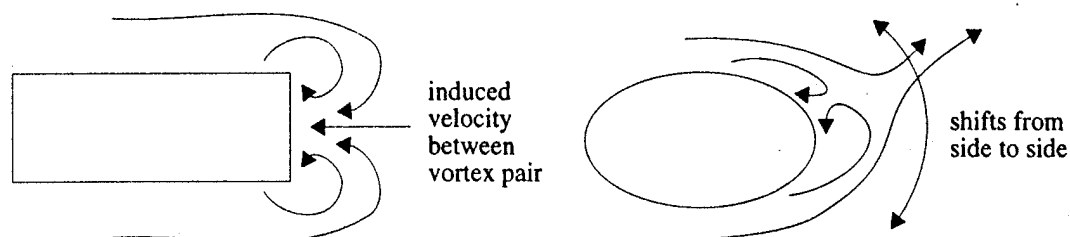
Figure 6-57: Flow Patterns at the Downstream Side of Holes 1 and 2
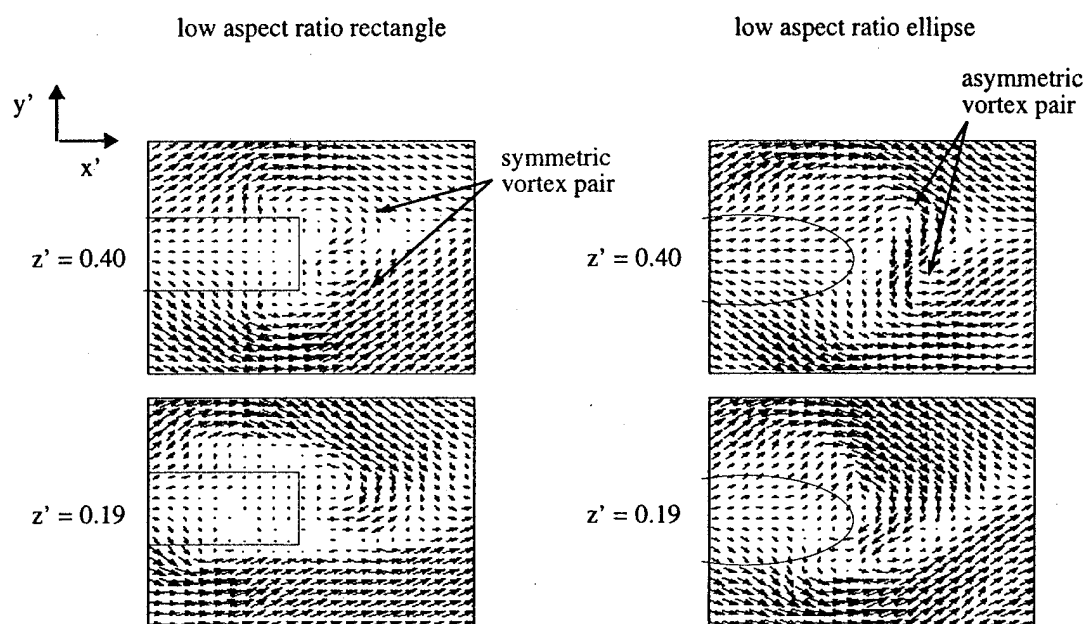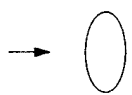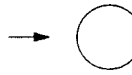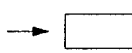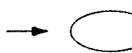
Figure 6-58: Vector Plots in Region Downstream of Holes 1 and 2, BR 1.6

6.7 Tabulated Summary

The following table summarizes the results of all holes, which classifies morphologically the 'positive' and 'negative' pair, and their association with hole boundary layer vorticities.

Table 6-1: Summary of Flow Structure Details

Hole Type	§	leading edge		side-wall	trailing edge	
		center	corner		center	corner
square (hole 4) ⭢ ▢	6.1	'unsteady' positive pair on top of 'steady' pair $(\omega_x, -\omega_x)$	'steady' positive pair $(\omega_x, -\omega_x)$	'steady' positive pair $(\omega_x, -\omega_x)$	'steady' positive pair $(\omega_x, -\omega_x)$ (note 1)	'steady' positive pair z-direction $(\omega_z, -\omega_z)$ (note 2)
high AR rectangle (hole 6) ⭢ ▯ high AR ellipse (hole 5) ⭢ ◯	6.2 6.3	'unsteady' negative pair on top of 'steady' pair $(-\omega_x, \omega_x)$	same as above	same as above	'steady' positive pair near wall $(\omega_x, -\omega_x)$	same as above
round (hole 3) ⭢ ◯	6.4	'unsteady' positive pair on top of 'steady' pair $(\omega_x, -\omega_x)$	same as above	same as above	'steady' negative pair near wall $(-\omega_x, \omega_x)$	same as above
low AR rectangle (hole 1) ⭢ ▭ low AR ellipse (hole 2 ⭢ ⬭	6.5 6.6	same as above	same as above	same as above	same as above	same as above

note 1: only at the highest BR of 2.0, 'steady' negative pair $(-\omega_x, \omega_x)$ near the wall.
note 2: near the trailing edge, 'steady' positive pair at its corner, shown on the right of figure 6-13, is the same vortex as the 'steady' positive pair along the side-wall, top of figure 6-1.

In sum, all hole boundary layer vorticity, regardless of its origin along the hole circumference, contributes to the kidney-pair sufficiently downstream. Even the 'negative' pair affects the downstream kidney-pair by moderating the influence of the 'positive' pair.

Chapter 7: IHI Ltd. Cooling Hole Configuration Studies

IHI Ltd., a leading aircraft gas turbine manufacturer in Japan, has provided us with the basic configuration data for three different hole designs referred to as TP2, TP3, and TP4. They had previously performed wind tunnel tests on these hole configurations to determine their heat transfer performance. These results indicate, in general, the superior performance of TP4 relative to the other two holes. In an attempt to understand the fluid dynamics behind the heat transfer performance, we performed water tunnel studies using both laser induced fluorescence and PIV. The water tunnel results, coupled with the heat transfer data from IHI, provide an opportunity to observe how the preceding studies, of a rather fundamental nature, can be applied to actual film cooling holes designs. In addition, it also yields a more complete understanding of how hole geometry, and that alone, can improve the effectiveness of a coolant jet.

7.1 IHI Hole Geometries and Experimental Setup

The three hole geometries investigated all have the same exit area (7.68 cm^2), inlet to exit area ratio (2.69), injection angle relative to the crossflow (35°), and passage length (8.3 cm). The difference between the holes is how the hole area is increased, i.e., lateral divergence only for TP4, versus the combination of lateral and streamwise divergence for TP2 and TP3. The coolant hole designs, TP2, TP3, and TP4, are shown in figure 7-1.

The holes were attached to a plenum instead of the settling chamber used in the previous experiments (figure 7-2). The plenum is 57 cm long, 5.4 cm high, and 11 cm wide. It consists of a diffuser section with walls that diverge at a half angle of 15 degrees. The dif-

Hole Inlet Area: 2.86 cm^2
Hole Area Ratio: 2.69
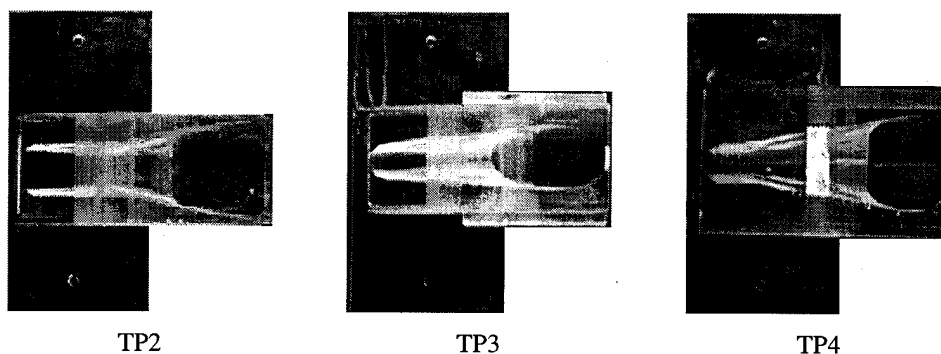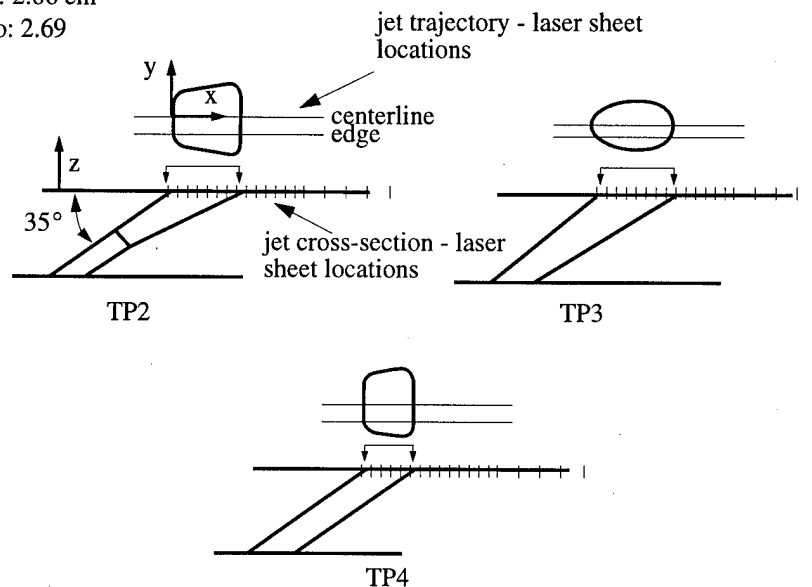
Figure 7-1:   IHI Hole Configurations

fuser section is followed by a 5 cm long straight section containing 3 mm diameter straws to straighten the flow. The jet entrance hole is located 14.5 cm downstream of the straws and positioned at 35° with respect to the crossflow. The plenum has a flow control valve at the outlet to adjust the flow through the plenum. For all the IHI hole experiments, the plenum outlet valve was closed so that all flow into the plenum was directed through the jet passage.
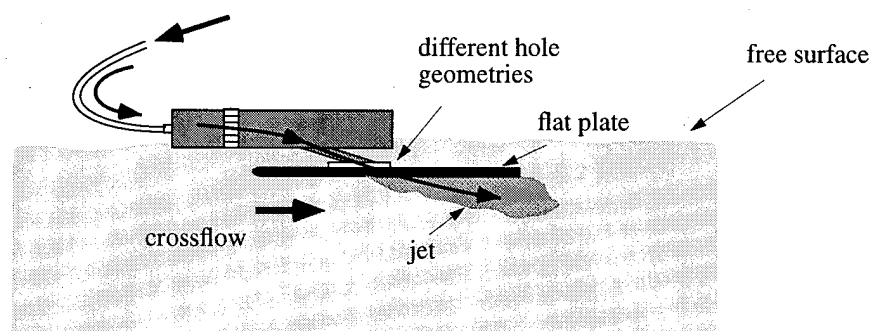
Figure 7-2: Jet Injection Plenum Configuration

7.2 Laser Induced Fluorescence Results

The crossflow velocity was set to 5.3 cm/s for all presented results. The jet velocity, determined from the volume flow rate and hole cross-sectional area at the exit plane, was 9.2 cm/s. This combination gives a blowing ratio based on the normal jet velocity component, BR_n, of 1.0. For comparison, if the blowing ratio is based upon the velocity entering the hole, the value would increase by a factor of 4.69 (area ratio/$\sin 35°$). This large blowing ratio was selected intentionally with the expectation that the lift-off characteristics of each of the jets would become more distinguishable.

The laser sheet was oriented along the axis of the jet, in the x-z plane, to look at the jet trajectory at the centerline and edge of the hole. The jet cross-sections were obtained in the y-z plane at intervals of 0.5 cm along the exit of the hole, and 1.3 cm downstream of the hole as illustrated in figure 7-1.

The flow visualization results presented in figures 7-3, 7-4, and 7-5, reveal a distinct difference in the attachment characteristics of the jet for the different holes. The combined views of jet trajectory and jet cross-sections provide substantial information about the behavior of the jet as it interacts with the crossflow fluid. Perhaps the most dramatic results are those shown in figure 7-3 for hole configuration TP2. The flow visualization reveals jet behavior that would compromise the effectiveness of the jet to protect the plate surface from intrusion of the crossflow fluid along the centerline of the jet. The jet appears

TP2

jet trajectory - BR$_n$ = 1.06
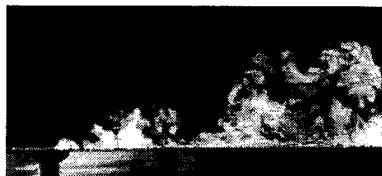
centerline   edge
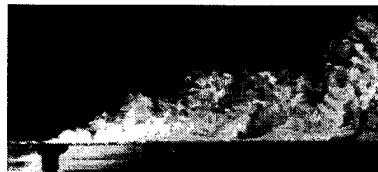
x-location
from leading edge
(cm)

jet cross-section - BR$_n$ = 1.00
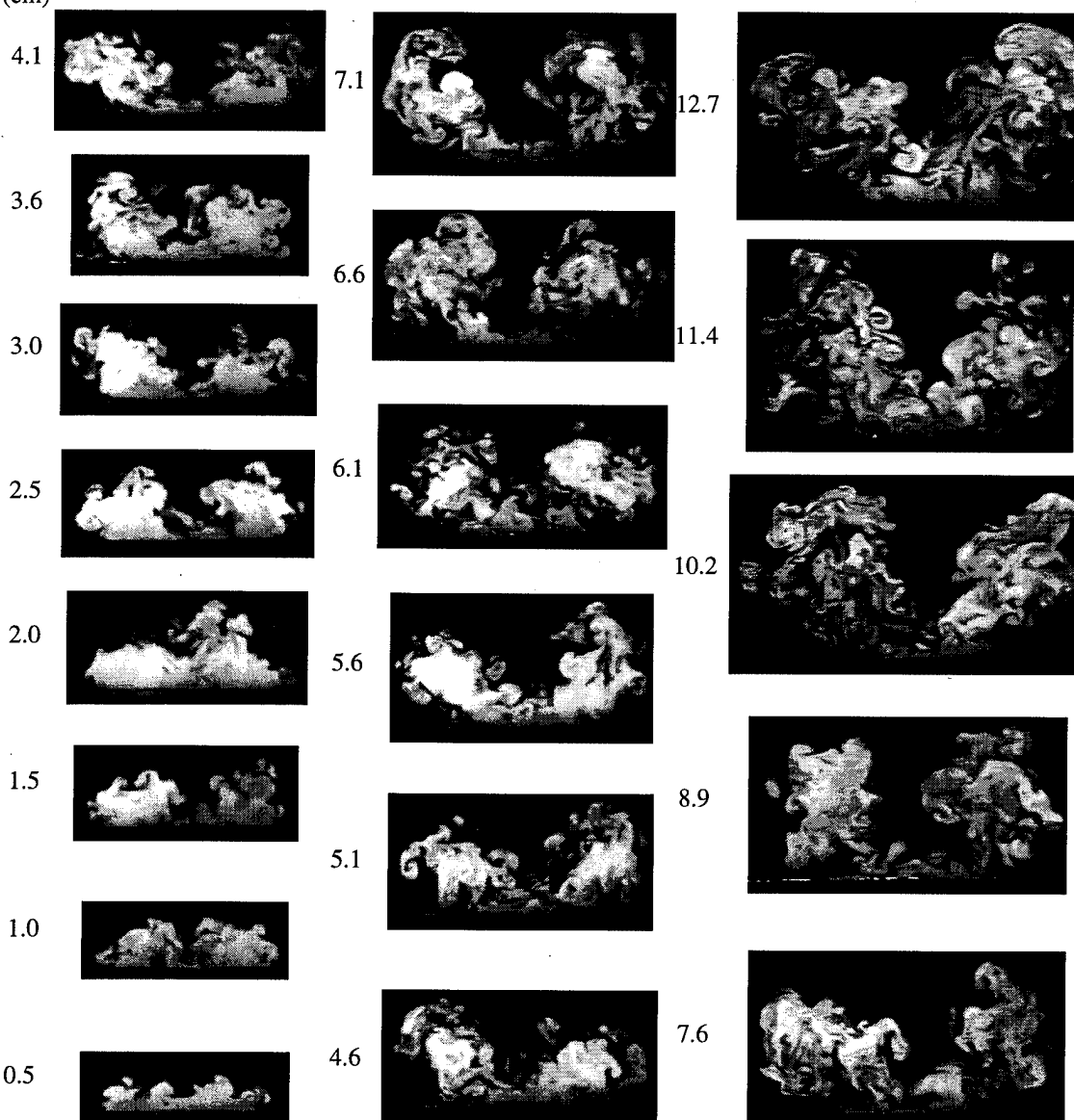
Figure 7-3: TP2: Jet Trajectory and Cross-sections at BR$_n$ = 1.06 and 1.00, Respectively

TP3

jet trajectory - $BR_n = 1.06$

centerline

edge

x-location
from leading edge
(cm)

jet cross-section - $BR_n = 1.00$

4.1

7.1

12.7

3.6

6.6

11.4

3.0

6.1

10.2

2.5

2.0

5.6

8.9

1.5

5.1

1.0

7.6

4.6

0.5
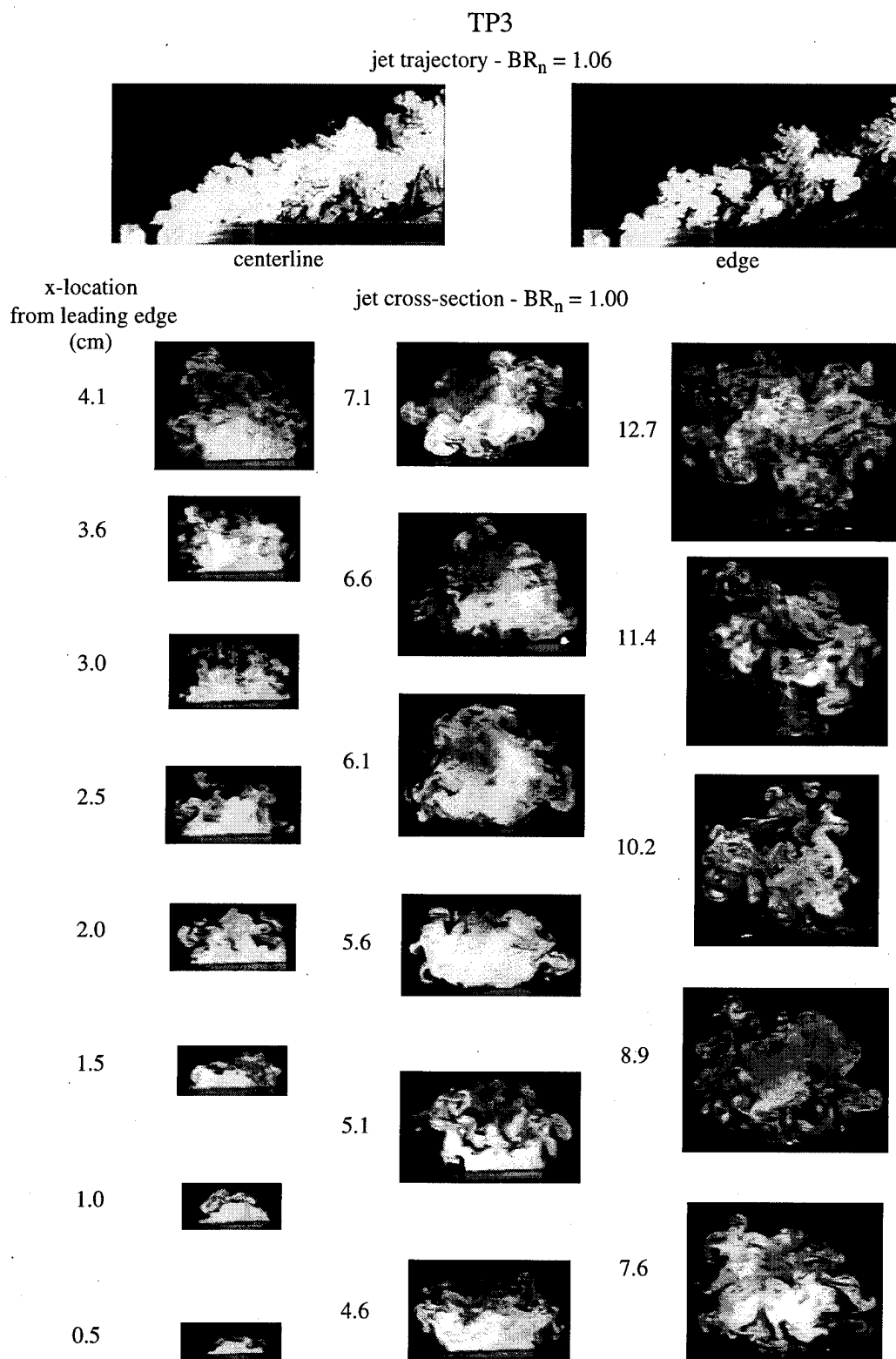
Figure 7-4: TP3: Jet Trajectory and Cross-sections at $BR_n = 1.06$ and 1.00, Respectively

TP4

jet trajectory - $BR_n = 1.06$

centerline   edge

x-location
from leading edge
(cm)

jet cross-section - $BR_n = 1.00$

4.1

7.1

12.7

3.6

6.6

11.4

3.0

2.5

6.1

10.2

2.0

5.6

1.5

8.9

5.1

1.0

7.6

4.6

0.5
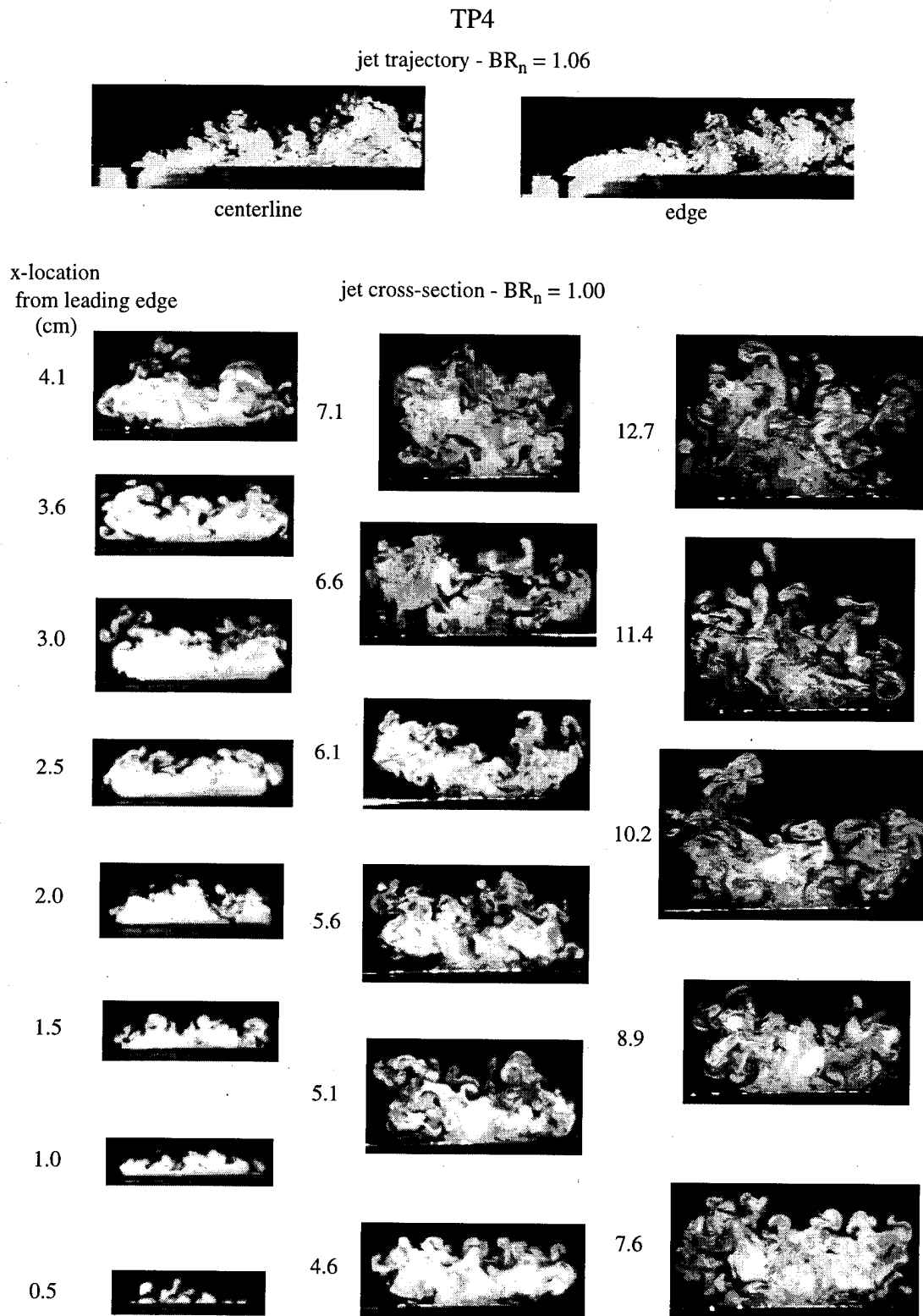
Figure 7-5:   TP4: Jet Trajectory and Cross-sections at $BR_n = 1.06$ and 1.00, Respectively

to migrate toward the outer edges of the jet, which leaves the centerline region "unprotected." This behavior is confirmed in both the cross-section and trajectory views. The trajectory views show that this void region passes intermittently along the jet centerline; however, toward the edge of the hole, the jet appears to have more uniform coverage.

The results for hole configuration TP3 in figure 7-4 show that as the jet proceeds downstream the jet is drawn together (especially near the plate surface) and begins to lift off the surface. Near the edge of the hole, the jet is almost completely detached. This lift-off of the jet fluid is an indication of reduced cooling effectiveness.

The attachment of the jet to the plate surface for TP4 is markedly better than that for either of the previous two holes (figure 7-5). The jet trajectory at both the centerline and edge of the hole are much closer to the surface with more uniform coverage over the span of the jet. Comparison of this behavior with that of the other holes suggests better film cooling effectiveness.

In light of the results previously presented in §6, the difference in jet characteristics among the three holes may be attributed, at least in part, to the realignment of the jet vorticity. Recall that for the case of the high aspect ratio rectangle, hole 6 of §6, the jet along the centerline is depressed in the region of the 'negative' vortex pair (figure 6-17). If this 'negative' pair becomes more dominant, the depression can widen to create a large void along the centerline of the jet which allows the crossflow fluid to penetrate to the plate surface (figure 7-3). Whether this is indeed an explanation for TP2 will be examined next by PIV.

7.3 PIV Results

Although the flow visualization results provide significant insight into the overall behavior of the jet, by making the fine vortex structure on the outer edge of the jet easily discernible, the details of the flow within the jet are completely masked by the fluorescent dye. PIV was used to increase the understanding of what happens inside the jet. However, PIV has its limitations as well. The camera-resolution limits the size of the vortex structures that can be quantified. All details associated with the small scale vortices appearing at the

boundary of the jet are too small to show up as individual vortex structures in the vorticity plots; therefore, the information to be presented undergoes some spatial averaging of the flow field. Nevertheless, the PIV data is very helpful in capturing the global characteristics of the jet.

PIV measurements were taken along the exit plane of the three holes to examine the velocity and vorticity fields perpendicular to the crossflow. These jet cross-section measurements, shown in figures 7-6 through 7-8,were taken at the same blowing ratio and x-locations as the flow visualization results presented in the previous section. Keep in mind that while the flow visualization pictures are instantaneous snapshots, the PIV images are time-averaged: thus they do not exactly correspond to each other on a one-to-one basis.

The void along the centerline for TP2 is confirmed in the v- and w-velocity plots in figure 7-6 obtained by PIV. At x = 2.0, 2.5 and 4.1 cm downstream of the leading edge, regions of high vertical velocity, w, appear at the edges of the jet, while at the center the velocity is in toward the plate surface (blue regions). The corresponding lateral velocity, v, plots show the sideways push of the jet fluid toward the edges of the hole. The vorticity plots show a counter-rotating vortex pair at the lateral edges of the hole: the side-wall kidney-vortices. Near the centerline, a 'negative' vortex pair is clearly evident for these same cross-sectional views. Based on the color coding for the vorticity plots, the strength of the 'negative' pair is similar to that of the side-wall kidney-vortices. This 'negative' pair drives the jet down, toward the wall and toward the edges of the hole, entraining the crossflow into the central region of the jet. Thus, this ill-positioned 'negative' pair has a detrimental effect, instead of the favorable effect of cancelling the kidney-vortices.

The flow visualization and PIV results for TP3, shown in figure 7-7, contain flow characteristics similar to those previously observed for the round hole, hole 3 of §6: the high vertical velocity at the center of the hole and the significant downward velocity at the edges. The corresponding vorticity plots show the distinct side-wall kidney-vortex pair at the edges of the hole. The vorticity pockets appearing between the side-wall pair have, in general, the same rotational sense as the kidney-vortices. This suggests that the leading edge boundary layer vorticity is being realigned in a similar manner to that of the previous

115
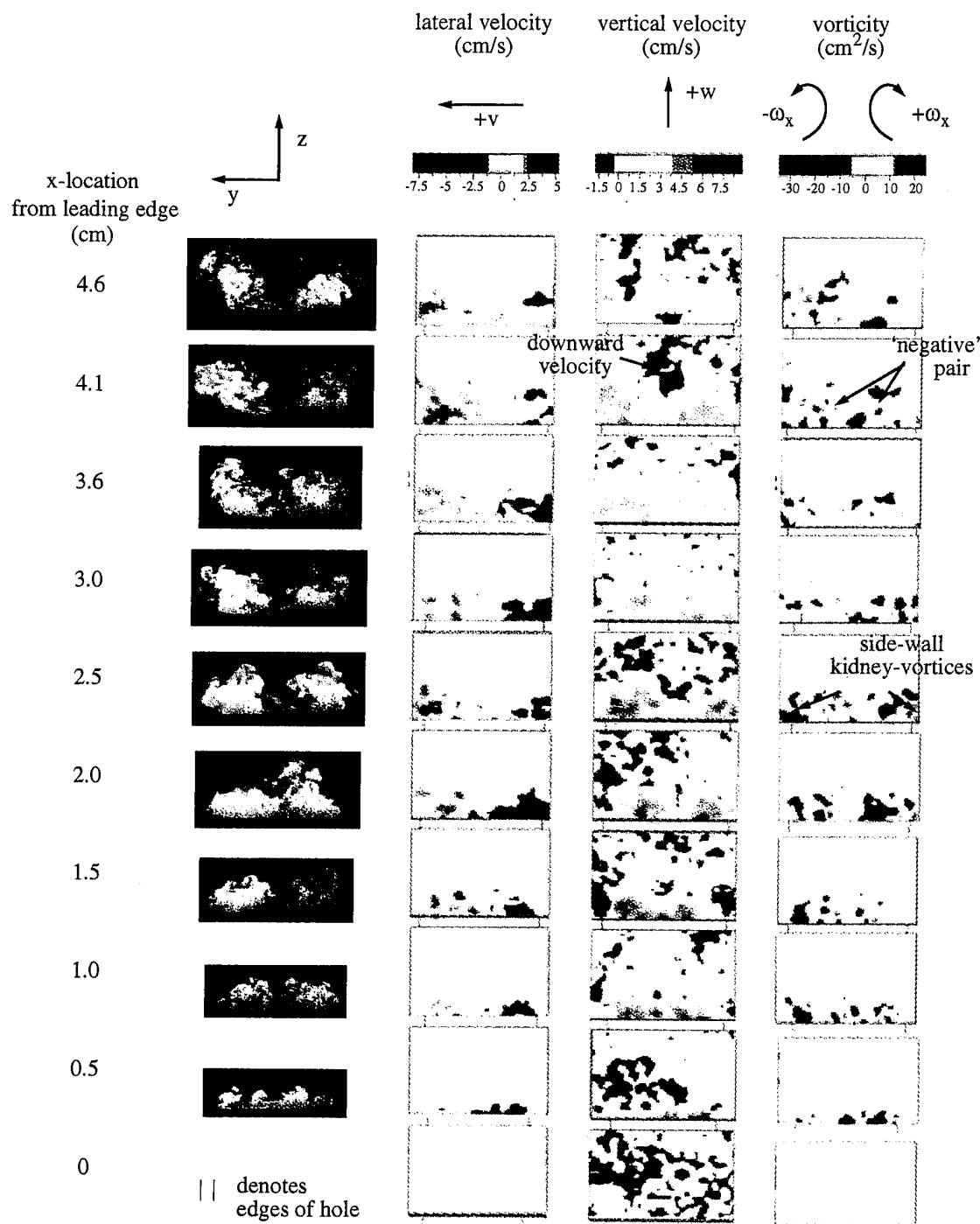
Figure 7-6: TP2: PIV Velocity and Vorticity Plots for Jet Cross-sections, $BR_n = 1.0$
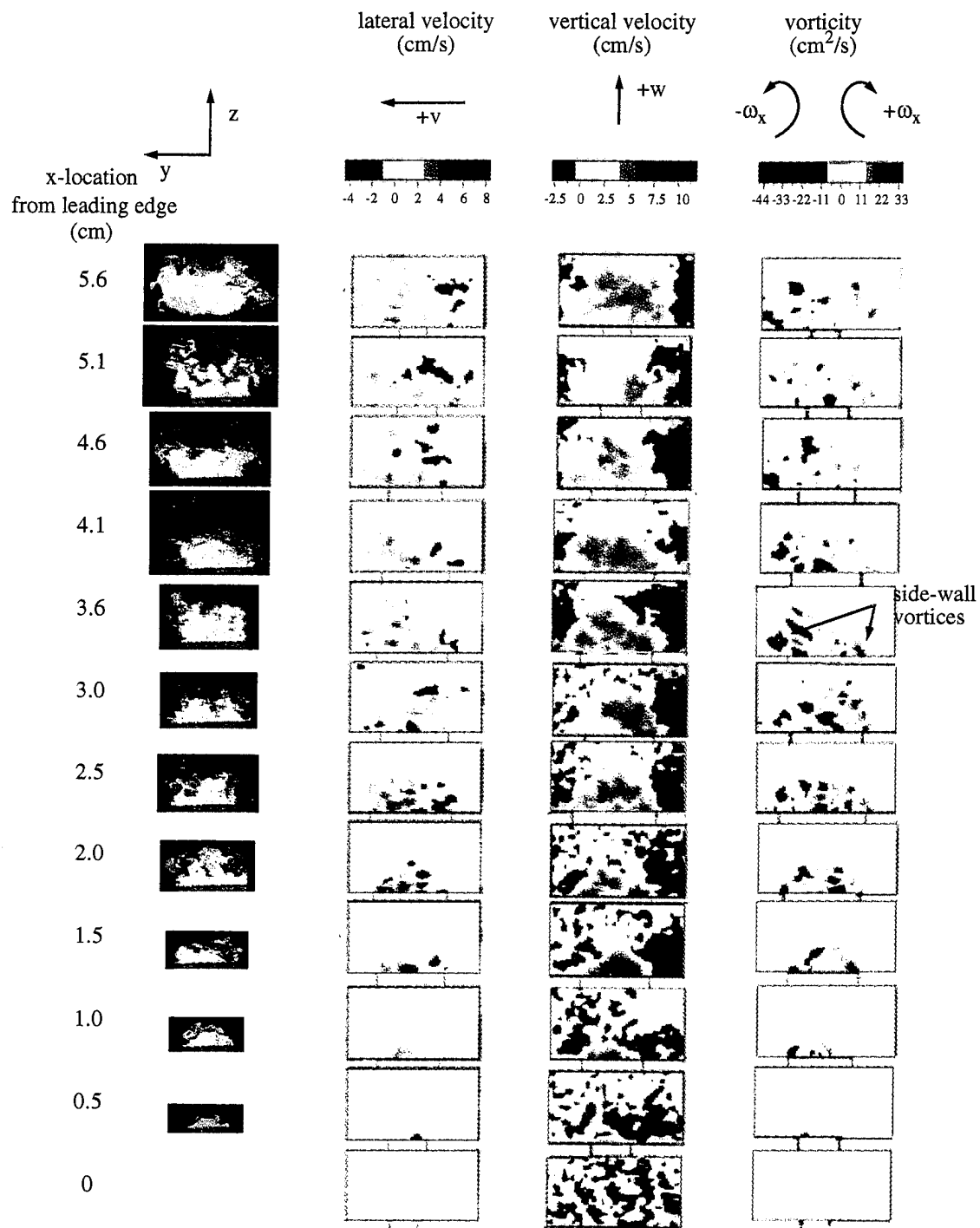
Figure 7-7:   TP3: PIV Velocity and Vorticity Plots for Jet Cross-sections, BR_n = 1.0

lateral velocity
(cm/s)

vertical velocity
(cm/s)

vorticity
(cm^2/s)

$\longleftarrow$
$+v$

$\uparrow$ $+w$

$-\omega_x$ $\quad$ $+\omega_x$

x-location
from
leading edge
(cm)

z

y

-4 -2 0 2 4

-2 0 2 4 6 8

-20 -10 0 10 20

3.6

3.0

2.5

2.0

1.5

1.0

side-wall
vortices

0.5

0
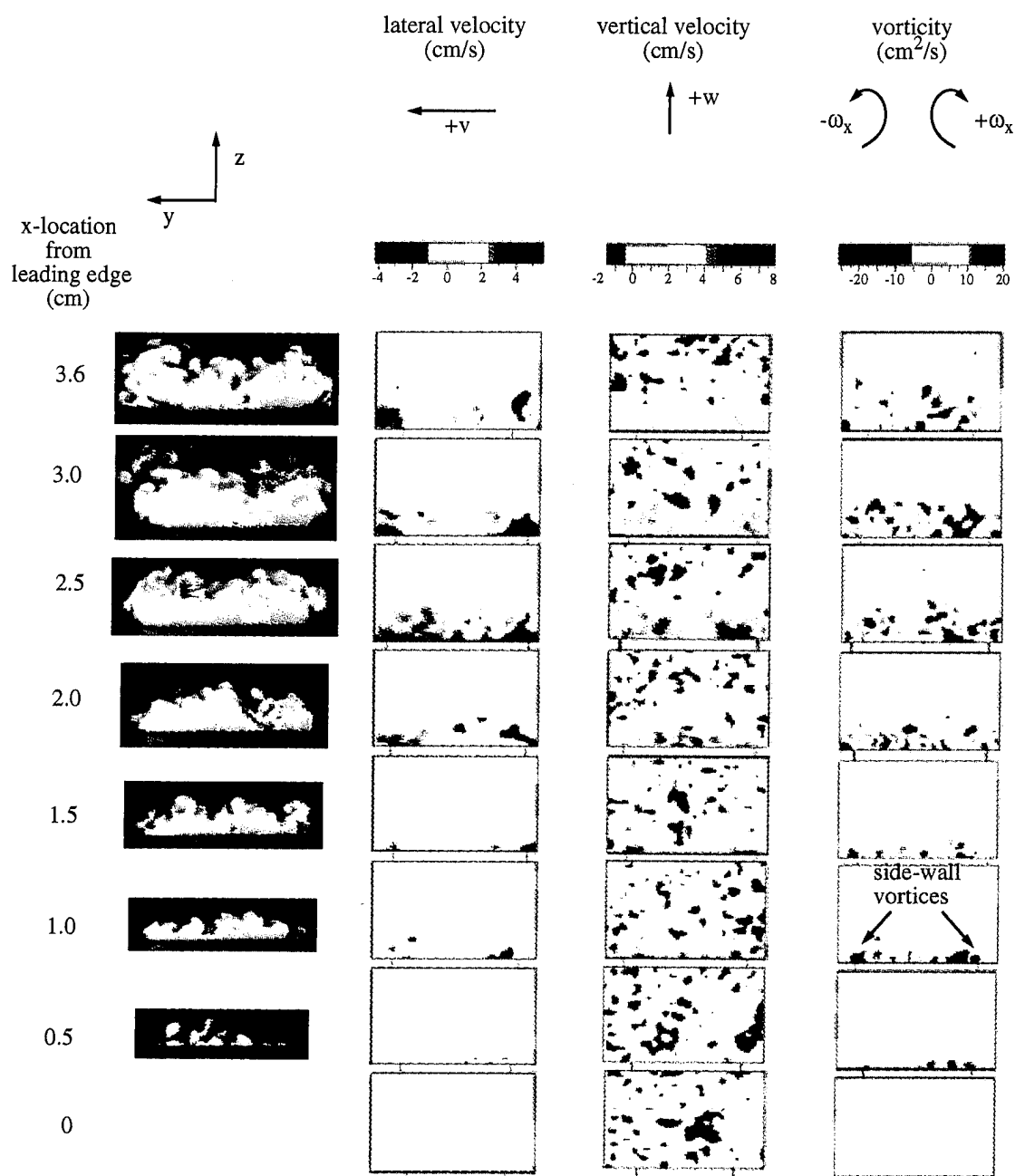
Figure 7-8: TP4: PIV Velocity and Vorticity Plots for Jet Cross-sections, $BR_n = 1.0$

round hole, hole 3 or the low aspect ratio ellipse, hole 2. This is not too surprising since the geometry of TP3 at the exit plane is almost elliptic.

The flow visualization results for TP4 show that the lateral distribution of jet fluid over the hole is much more uniform that for the other two hole configurations. This behavior is again confirmed by the PIV vertical velocity plots in figure 7-8. Perhaps the greatest insight into the behavior of the jet comes from the vorticity plots. Here the distribution of positive and negative vorticity is much less organized compared to TP2 and TP3. This mosaic pattern results in the competition between the 'positive' and 'negative' vortex pairs. This competition promotes annihilation, which, as pointed out previously in figure 4-2, may be the ultimate reason for the improved coverage.

7.4 Implications to Heat Transfer

The near field ($x/D = 10$) IHI film cooling effectiveness data presented in figure 7-9, for a density ratio of 1.1, may be interpreted based on the observed characteristics of each jet presented above. The reduced coverage for both TP2 and TP3, suggests a lower film cooling effectiveness compared to TP4, which is indeed the case. For a blowing ratio of 2.5 (based on the total magnitude of the jet exit velocity rather than its normal component) the heat transfer data shows that TP4 has a higher film effectiveness than either TP2 or TP3. (For description of IHI experimental set-up, see Yamawaki, Maya, and Yasu, 1996)
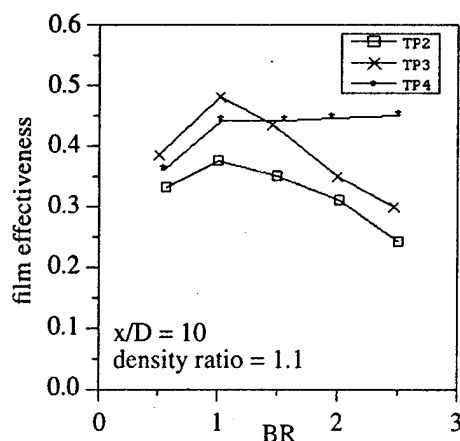
Figure 7-9: IHI Heat Transfer Data (1995) for TP2, TP3, and TP4

Chapter 8: Conclusions

On the problem of film cooling hole geometry and jet lift-off, we posed three questions in the beginning (§1.4). In specific response to these, here we summarily itemize the results presented in §3 through §7. This summary will be followed by a brief description of suggested areas for future research.

8.1 Summary of Results

8.1.1 Question 1:

Can the hole geometry alone influence lift-off without the need to manipulate the hole cross-sectional area?

As shown in §3.2, hole geometry has a definitive influence on the very near field character of the kidney-vortices. The proximity of these counter-rotating vortices relative to one another affects both the lift-off of the jet and the entrainment of crossflow fluid toward the plate surface. The LIF results for six basic hole geometries show that the jet from the large aspect ratio holes, which increase the separation distance between the side-wall vortices, stays attached to the surface for higher blowing ratios, while for the low aspect ratio holes, it tends to blow off. Thus, by manipulating the hole geometry alone, one can reduce jet lift-off, without the need to increase the hole cross-sectional area.

Bear in mind, however, that although the width of the side wall fixes the initial separation distance between the side-wall vortices, there are other factors which modify the effect significantly, as summarized next.

8.1.2 Question 2:

Do the leading and trailing edge boundary layers simply cancel each other, or do they modify the effect of the side-wall boundary layer to influence jet lift-off?

The flow visualization and PIV studies of §5 and §6 reveal distinct contributions to the kidney-vortices from the leading and trailing edge boundary layers. Here, rectangular geometries enable the clear distinction between the vorticity arising from the leading and trailing edges and that from the side-wall boundary layer,

The outer portion of the leading edge boundary layer spills sideways upon leaving the hole and then combines with the side-wall boundary layer. The central portion is periodically shed from the hole and rides on top of the jet (§5.3). The periodic vortex shows up in the jet cross-sections as either a 'positive' or 'negative' vortex pair on top of the 'positive' steady side-wall vortices. The hole geometry determines whether the leading edge boundary layer is warped to induce this 'positive', or 'negative' unsteady pair; the 'negative' pair corresponds to the high aspect ratio hole, holes 5 and 6 (§6).

The trailing edge boundary layer may be warped by the reverse flow, in a similar manner as the leading edge boundary layer. Here, the reverse flow is due to the combined effect of jet bending and the tilting of the trailing edge vortex sheet near the jet centerline. This reverse flow acts like a crossflow to the back side of the jet, which can cause warping similar to that seen for the leading edge. The appearance of the 'negative' pair at the trailing edge also depends on the hole geometry, just like the one at the leading edge. The corner vortex pair $(\omega_z, -\omega_z)$ at the trailing edge of the hole is caused by the tilting of the trailing edge boundary layer and eventually becomes a positive pair further downstream. Its position is established by the downstream contour of the hole. The low aspect ratio holes provide lesser separation for the vortex pair, and thus, increases the reverse flow and subsequent penetration near the centerline of the jet. Hole curvature also appears to play a role in the upstream penetration of the reverse flow. For the low aspect ratio rectangle, the discrete corners fix the location of the vortex pair $(\omega_z, -\omega_z)$: the area between this pair becomes a channel for the reverse flow. For the round and elliptic holes, however, the continuous curvature prevents the vortex pair from establishing a fixed location; they instead move along the downstream sides of the hole and limit the upstream penetration.

The results of §6 show that all the vorticity around the circumference of the jet combine to form the downstream kidney-vortex structures. As the jet exits the hole, the crossflow acts to realign some of the jet vorticity in such a way that it can enhance the side-wall kidney-vortices or reduce their strength through annihilation.

8.1.3 Question 3:

Can these fundamental results be used to diagnose and evaluate the more complex holes actually used in industry?

The results for the more complex IHI hole geometries presented in §7 can be interpreted based on the simpler hole results presented in §3 through §6.

The lowest aspect ratio hole, TP3 has nearly an elliptical cross-section at the exit plane. The flow visualization and PIV results show many similarities to the low aspect ratio ellipse. Here the kidney-vortices are formed close together, which increases the mutual induction, and as a consequence, increases the jet lift-off.

In comparing holes TP2 and TP4, the difference is not in the lift-off of the jet, but in the unprotected region along the centerline for TP2. Based on the finding in §5 and §6, with regard to the role of the leading edge boundary layer, we believe this void is due to a strong 'negative' vortex pair which acts to separate the jet and draw crossflow fluid toward the surface at the jet centerline. For TP4, the 'positive' and 'negative' vorticity appears more evenly distributed across the span of the hole. This arrangement of the vorticity is believed to promote annihilation, which may be the underlying reason for it s improved performance relative to TP2.

8.1.4 Summary

In sum, the most noteworthy results of the present study are that hole width fixes the separation distance between the kidney-vortices, and certain hole-shapes are conducive to the formation of a negative pair of vortices. This 'negative' pair competes with the 'positive', or kidney-vortices and the net balance between them determines the film coverage and jet lift-off.

8.2 Future Research

Suggested areas of future research are as follows:

1. Manipulate the hole exit geometry to isolate the effect of the 'negative' vortex pair due to the leading edge boundary layer.

2. Investigate the effect of angled injection on the jet characteristics for the same basic hole configurations presented in §3 through §6.

3. Examine the effect of jet fluid density, which may introduce additional vortices due to baroclinic torque.

4. Delineate the connection between the hairpin vortices observed at low blowing ratios with the various vortex structures examined here.

References

Adler, D. and Baron, A. "Prediction of a Three Dimensional Circular Turbulent Jet in a Crossflow" *AIAA Journal*, vol.17, pp. 168-174, 1979.

Ajersch, P., Zhou, J.M., Ketler, S., Salcudean, M., and Gartshore, I. S. "Multiple Jets in a Crossflow: Detailed Measurements and Numerical Simulations" ASME paper 95-GT-9, 1995.

Andreopoulos, J. "Measurements in a Jet-Pipe Flow Issuing Perpendicularly Into a Cross Stream" *Journal of Fluids Engineering*, Transactions of the ASME, vol. 104, pp. 493-499, 1982.

Andreopoulos, J. "On the Structure of Jets in a Crossflow" *Journal of Fluid Mechanics*, vol.157, pp. 163-197, 1985.

Andreopoulos, J. and Rodi, W. "Experimental Investigation of Jets in a Crossflow" *Journal of Fluid Mechanics*, vol.138, pp. 93-127, 1984.

Bergeles, G., Gossman, A.D. and Launder, B.E. "The Near-Field Character of a Jet Discharged Normal to a Main Stream" *Journal of Heat Transfer*, Transactions of ASME, pp. 373-378, 1976.

Broadwell, J.E. and Breidenthal, R.E. "Structure and Mixing of a Transverse Jet in Incompressible Flow" *Journal of Fluid Mechanics*, vol. 148, pp. 405-412, 1984.

Brown, A. and Minty, A.G. "The Effects of Mainstream Turbulence Intensity and Pressure Gradient on Film Cooling Effectiveness for Cold Air Injection Slits of Various Aspect Ratios" ASME Paper 75-WA/HT-17, 1975.

Coelho, S. L.V. and Hunt, J.C.R. "The Dynamics of the Near Field of Strong Jets in Crossflow" *Journal of Fluid Mechanics*, vol. 200, pp. 95-120, 1989.

Crabb, D., Durao, D.F.G., and Whitelaw, J.H. "A Round Jet Normal to a Crossflow" *Journal of Fluids Engineering*, Transactions of ASME, vol. 103, March, pp. 142-153, 1981.

Durando, N. A. "Vortices Induced in a Jet by a Subsonic Cross Flow" *AIAA Journal*, vol. 9, no. 2, pp. 325-327, 1971.

Eroglu, A. "An Experimental Investigation of Entrainment and Mixing in Pulsed and Exponential Transverse Jets" Ph.D. thesis, University of Washington, 1991.

Fearn, R.L. and Weston, R.P. "Induced Pressure Distribution of a Jet in a Cross-Flow" NASA TN D-7916, 1975

Fearn, R.L. and Weston, R.P. "Vorticity Associated with a Jet in a Cross Flow" *AIAA Journal*, vol. 12, No. 12, pp. 1666-1671, 1974.

Fric, T.F. "Structure in the Near Field of the Transverse Jet" Ph.D. thesis, CalTech, 1990.

Fric,T.F. and Roshko, A. "Vortical Structure in the Wake of a Transverse Jet" *Journal of Fluid Mechanics*, vol. 279, pp. 1-47, 1994.

Goldstein, R.J., Eckert, E.R.G. and Burgraff, F. "Effects of Hole Geometry and Density on Three-Dimensional Cooling" *International Journal of Heat and Mass Transfer*, vol. 17, pp. 595-607, 1974.

Hoult, D.P. and Weil, J.C. "Turbulent Plume in a Laminar Cross Flow" *Atmospheric Environment*, vol. 6, pp. 513-531, 1972.

IHI, Ltd. Heat Transfer Data, 1995.

Kadotani, K.and Goldstein, R. J. "Effect of Mainstream Variables on Jet Issuing from a Row of Inclined Round Holes" *Journal of Engineering for Power, Transactions of ASME*, vol 101, pp. 298-304, 1979.

Kamotani, Y. and Greber, I. "Experiments on a Turbulent Jet in a Cross Flow" *AIAA Journal*, vo.10, no. 11, pp. 1425-1429, 1972.

Karagozian, A.R. "An Analytical Model for the Vorticity Associated with a Transverse Jet" *AIAA Journal*, vol. 24, pp. 429-436, 1986.

Keffer, J.F. and Baines, W.D. "The Round Turbulent Jet in a Cross-Wind" *Journal of Fluid Mechanics*, vol. 15, Part 4, pp. 481-496, 1963.

Kelso, R.M., Lim, T.T., and Perry, A.E. "An Experimental Study of Round Jets in Crossflow" *Journal of Fluid Mechanics,* vol. 306, pp. 111-144, 1996.

Kikkawa, S.and Nakanishi, K. "Experimental Investigation on Film Cooling of a Pressure Surface of a Gas Turbine Blade" pp. 27-36, in *Heat Transfer and Fluid Flow in Rotating Machinery*, Hemisphere Publishing Co. 1987

Krothapalli, A., Lourenco, L., and Buchlin, J. M."Separated Flow Upstream of a Jet in a Crossflow" *AIAA Journal*, vol. 28, no. 3, pp. 414-420, 1990.

Liscinsky, D. S., True, B., and Holdeman, J.D. "Cross flow Mixing of Noncircular Jets" AIAA Paper 95-0732, 1995.

Makki,Y.H.and Jakubowski, G.S. "An Experimental Study of Film Cooling from Diffused Trapezoidal Shaped Holes" AIAA -86-1326, 1986.

Moussa, Z. M., Trischka, J.W. and Eskinazi, S. "The Near Field in the Mixing of a Round Jet with a Cross-Stream" *Journal of Fluid Mechanics*, vol. 80, pp. 49-80, 1977.

Norton, R.J.G., Forest, A.E., White, A.J., Henshaw, D.G., Epstein, A.E., Schultz, D.L., and Oldfield, M.L.G., "Turbine Cooling System Design: Vol 1 - Technical Report" WRDC-TR-89-2109, 1990.

Papell, S.S. "Vortex Generating Flow Passage Design for Increased Film-Cooling Effectiveness and Surface Coverage" NASA Technical Memorandum 83617, 1984.

Schatzmann, M. "An Integral Model of Plume Rise" *Atmospheric Environment*, vol. 13, 721-731, 1979.

Scorer, R. S. " Natural Aerodynamics" Pergamon Press, p. 194 and p. 210, 1958.

Shi, Z., Wu, J.M., and Wu, J.Z., "Symmetric and Asymmetric Jets in a Uniform Crossflow" AIAA 91-0722, 1991.

Simpson, A.G. "Flow Visualization of Vorticity Cancellation of Jet in Crossflow" M.S. thesis, University of Washington, 1995.

Sugiyama, Y. "A Calculation of Penetration of the Jet Issuing Normally into a Cross Flow Across a Wall Boundary Layer" SAE Technical Paper Series 912029, International Pacific Air and Space Technology Conference and 29th Aircraft Symposium. Gifu, Japan, Oct 7-11, 1991.

Sugiyama, Y. "Formation and Behavior of the Vortices Associated with a Transverse Jet" IUTAM Symposium, Göttingen, Germany, edited by Eckelmann, H., Graham, J.M.R., Huerre, P.and Monkewitz, P.A., pp. 211-214, 1992.

Sugiyama,Y. "Pressure Distribution on and Around an Exit Plane of a Jet Normal to a Cross-Flow" 1995 International Gas Turbine Congress, Yokohama.vol. II-375-382, 1995.

Sugiyama, Y. and Kawase, M. "A Flow Field with a Jet affected by a Nonuniform Cross Flow" Bulletin of Japan Society of Mechanical Engineers, Vol. 28, N0. 241, pp. 1387-1395, 1985.

Sugiyama, Y. and Usami, Y. "Experiments on the Flow in and Around Jets Directed Normal to a Cross Flow" Bulletins of Japan Society of Mechanical Engineers, vol.22, No. 174, pp. 1736-1745, 1979.

Sykes, R.I., Lewellen, W.S., and Parker, S.F. "On the Vorticity Dynamics of a Turbulent Jet in a Crossflow" *Journal of Fluid Mechanics*, vol.168, pp. 393-413, 1986.

Takeishi, K. "Study on Gas Turbine Film Cooling" Ph.D. thesis, University of Osaka, 1995 (in Japanese).

Trentacosta, N. and Sforza, P. "Further Experimental Results for Three-Dimensional Free Jets" *AIAA Journal*, vol. 5, May 1967.

TSI Particle Image Velocimetry System Operation Manual, 1995.

Turner, J. S. "Buoyant Vortex Rings and Vortex Pairs" *Journal of Fluid Mechanics,* vol. 7, Part 3, March, pp. 419-433, 1960.

Vogler, R.D. "Surface Pressure Distributions Induced on a Flat Plate by a Cold Air Jet Issuing perpendicularly from the Plate and Normal to a Low-Speed Free-Stream Flow" NASA TN D-1629, 1963.

Wu, J.M., Vakili, A.D. and Yu, F. M. "Investigation of the Interacting Flow of Nonsymmetric Jets in Crossflow" *AIAA Journal*, vol. 26, no. 8, pp. 940-947, 1988.

Yamawaki, S., Maya, T., and Yasu, S. "Study of Film Cooling with Shaped Holes for a Hydrogen Combustion Turbine Blade" Preceedings of the 11th World Hydrogen Energy Conference, June 1996.

Vita

Name: Brenda Ann Haven

███████   ███████

███████   ███████

Parents: John and Donna La Haye

Education: B.S. Aerospace Engineering
University of Minnesota
Minneapolis, MN
June 1983

M.S. Aeronautical Engineering
Air Force Institute of Technology
Wright-Patterson, AFB, OH
March 1988

Doctor of Philosophy
Department of Aeronautics and Astronautics
University of Washington
Seattle, WA
June 1996